Modeling diffuse neutrino fluxes from gamma-ray bursts

Diplomarbeit
von
Philipp Baerwald

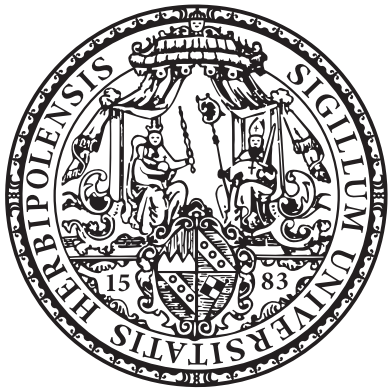

vorgelegt bei
PD Dr. Walter Winter

am
Institut für Theoretische Physik und Astrophysik
der
Julius-Maximilians-Universität Würzburg

22. December 2010

Kurzzusammenfassung

In der vorliegenden Arbeit stellen wir einen neuen Ansatz zur Simulation des Neutrinoflusses von Gamma-Ray Bursts (GRBs) vor. Ausgehend von grundlegenden physikalischen Konzepten und Wissen aus der Teilchenphysik simulieren wir die Produktion besagter Neutrinos in den aus photohadronischen Wechselwirkungen resultierenden Zerfallsketten. Wir zeigen, dass sich das vielzitierte Waxman-Bahcall Flussspektum mittels Approximation der photohadronischen Wechselwirkungen durch die Δ-Resonanz reproduzieren lässt. Anschließend erläutern wir wie sich das Form des Flussspektums ändert, wenn man den vollen Wechselwirkungsquerschnitt der photohadronischen Wechselwirkungen berücksichtigt und die Mischung der flavor-Zustände der Neutrinos berücksichtigt. Weiterhin überprüfen wir den Effekt von Parameterverteilungen. Wir testen mittels Monte Carlo sampling Modelle für den Lorentz-Faktor Γ, die Rotverschiebung z und das magnetische Feld B und deren Effekt auf den Neutrinofluss. Im Zuge dieser Überprüfung quantifizieren wir auch den Effekt, den eine geringe Stichprobenmenge auf das Resultat der Verteilung hat. Zum Schluss geben wir einen Ausblick auf Punkte, die im Zusammenhang mit diesem Projekt noch bearbeitet werden sollten, und in welchen Gebieten noch Entwicklungspotential besteht.

Abstract

In this work we present a new algorithm for the simulation of the gamma-ray burst (GRB) neutrino flux. We simulate the production of neutrinos from photohadronic interactions using fundamental physical concepts and knowledge of particle physics. We show that we can reproduce the much-quoted Waxman-Bahcall spectrum by using the Δ-resonance approximation for the photohadronic interactions. Hence, we describe how the flux shape changes when we consider the full photohadronic cross section and also include flavor mixing. Moreover, we analyze the effect of parameter distributions on the flux shape. Utilizing Monte Carlo sampling we test models for the distribution of the Lorentz factor Γ, the redshift z, and the magnetic field B. In the course of this investigation we also consider the effect of low count statistics on the resulting flux shape. Finally, we give a short outlook on open issues and possible improvements.

Contents

1. Introduction

In the range of the standard model the neutrino is a unique particle. It was first proposed (or one could say "invented") by W. Pauli in 1930 in an attempt to explain discrepancies in energy, momentum and angular momentum in atomic (beta) decays [1]. The name "neutrino" for these new particles was introduced in 1934 by E. Fermi when he developed his theory of β-decay [2]. The main problem at that point was that the means of detection were not known and still had to be developed on the basis of theoretical results. It took until 1956 for the confirmation of the existence of neutrinos, see Ref. [3]. C. Cowan et al. designed and constructed a large multi-layer detector near a nuclear power plant reactor in an attempt to measure neutrinos from nuclear fission. In the detector the reaction

$$\bar{\nu} + p^+ \rightarrow e^+ + n \tag{1.1}$$

leads to multiple photon pulses which are closely correlated. The first burst is due to pair annihilation from e^+ hitting an e^-, the second one due to n being caught in the scintillator medium. The results from these measurements proved Fermi's theory and verified Pauli's intuition that a particle in the lepton sector had been missing in the particle zoo. In due course the particle physics advanced and new leptons - μ and τ - where discovered and measurements again demonstrated that these also had to have associated neutrinos. It took years for the direct detection of all neutrino flavors, with the (final) detection of interactions of ν_τ being published in Ref. [4] in 2001 by the DONUT collaboration.

As the name "neutrino" suggests they are electrically neutral (have no electric charge) and are extremely small (suffix "-ino"). Here "small" refers to the mass of neutrinos as well as their interaction cross section. From tritium decay end point measurements the mass of the neutrinos is confined to $m_\nu < 2\,\mathrm{eV}$, see Ref. [5]. As for the cross section it has to be noted that νs only participate in standard charged current (CC) and neutral current (NC) weak interactions. This leads to very small cross sections of the order of $\sigma_{\nu N,\mathrm{CC}} = 10^{-38}\,\mathrm{cm}^2$ at $E_\nu = 10\,\mathrm{GeV}$ (in case of the

νN charged current interactions). The basic set of attributes can be derived from the properties of the lepton sector. Since leptons exist as particles and anti-particles there also have to be antineutrinos. Also, there are three flavors of charged leptons; electrons, muons and taus. Correspondingly there have to be electron neutrinos ν_e and antineutrinos $\bar{\nu}_e$, muon neutrinos ν_μ and antineutrinos $\bar{\nu}_\mu$ and tau neutrinos ν_τ and antineutrinos $\bar{\nu}_\tau$. It is now considered an experimental fact that these neutrinos take part in the aforementioned weak interactions. For example, Standard Model fits to LEP data show that there are $N = 2.984 \pm 0.008$ flavors of interacting neutrinos, taken from Ref. [5] and references therein. Being leptons neutrinos possess a spin of 1/2. And their mass is so small that they were considered massless for a long time. In section 3.3 we will take a closer look at the masses when discussing the propagation.

Already 14 years before the direct detection of ν_τ, neutrinos from outside our solar system were detected. In 1987, as reported in Ref. [6], a burst of neutrinos from supernova SN1987A was recorded by M. Koshiba and collaborators. These were the first detected extraterrestrial neutrinos apart from the solar neutrino signal. This was an important step for astronomy as it marked the possibility of observing the universe in neutrinos. Before the detection of neutrino emission from this supernova, astronomers were restricted to information from photons (from gamma-rays to radio waves) and cosmic rays (charged particles such as α, β, p or higher ions). All of these "old" observation methods have limitations in their accessible range. Photons can *e.g.* get absorbed by matter while cosmic rays get deflected by magnetic fields which makes the reconstruction of their origin nearly impossible. Neutrinos with their property of only being subject to weak interactions are not as distance limited as photons or charged particles. Thus a new field of astronomy - neutrino astronomy - was born. In the past each new "window" of observation has led to a wide set of new discoveries in astronomy with neutrinos being the most recent one. This was honored by the 2002 Nobel Prize in Physics, shared between R. Davis Jr. for his pioneering work on the detection of solar neutrinos, *e.g.* Refs. [7, 8], and M. Koshiba for the detection of the SN1987A neutrinos, Ref. [6].

Unfortunately, the great advantage of the weakly interacting neutrinos is also their main limitation. The interaction cross section of neutrinos is so low that events can rarely be detected. The only way of recording a sufficient number of events is by using a large detector volume and running measurements over a long time. Because

of this limitation current state of the art neutrino telescopes have up to $1\,\mathrm{km}^3$ of detector volume. Neutrino telescopes of such size are Km3Net in the Mediterranean Sea, which is still in the planing stages [9, 10], and the IceCube neutrino telescope at the South Pole [11], that will be completed in 2011 and is already taking data. Both telescopes are designed to detect Cherenkov radiation from neutrino induced muons in the deep sea or Antarctic ice. In case of IceCube the detector consists of several strings with photomultiplier tubes deployed 2 km deep in the ice, see Ref. [11]. These track events have to be analyzed to determine if or what kind of cosmic object produced the detected neutrino. For these analyses theoretical models of the sources are needed and particle physics comes back to the focus of interest. For all astrophysical uncertainties it is essential to have models of the shape of the neutrino spectra from different astrophysical sources. However, so far no high energy neutrino signal has been detected by any of the experiments.

When these telescopes finally detect the first signals, it will lead to the next step in multi-messenger physics. A key part of deciphering the vast range of objects in the observable universe is utilizing all the possible sources of information. Each kind of particle, such as cosmic rays, photons of different energy ranges and neutrinos, can be used to observe a certain part of the whole picture. The combination of all data of an object, or of a region in space, helps to understand it better. In the case of neutrinos the vast distances they can travel unperturbed are the greatest advantage. It is one of the goals of multi-messenger astrophysics to determine the sources of cosmic rays. If it is possible to establish a connection of a cosmic ray (CR) source to a source of cosmic neutrinos, astrophysical neutrinos could be used to probe cosmic ray sources. This would be mandatory for detecting high energy cosmic ray sources, because directional information of the highest energy cosmic rays is lost due to magnetic fields in space. It is assumed that the highest energy cosmic rays originate from extragalactic sources. However, these charged particles are deflected by the intergalactic magnetic field. Moreover, it might even be not necessary to detect point sources. A diffuse flux of neutrinos, similar to the extragalactic CR flux, could already be sufficient when detected. This diffuse flux could, in principle, be explained by connecting certain astrophysical sources, such as active galaxy nuclei (AGN) or gamma-ray bursts (GRBs), to highest energy particle production. Furthermore, neutrinos can be used to probe the inner regions of stars. In case of the Sun it was expected that nuclear fusion led to the vast energy output. Unfortunately, the photons reaching Earth are emitted from the photosphere of the sun, far above the core of Sun. Cosmic rays emitted from the Sun are ejected from

the corona, and, therefore, are also useless for information on the inner part of the Sun. Only neutrinos can pierce through the outer layers and thus give information on processes in the core of the Sun. The detection of a solar neutrino flux proved that the models with nuclear fusion in the Sun, and presumably other stars, are correct.

Hence, the detection of neutrinos from a certain kind of cosmic source would be a huge step in understanding cosmic accelerators. One particular case being discussed in the literature is the neutrino production of gamma-ray bursts. There have been several models for these extremely energetic events, but, unfortunately, there is no final agreement how these bursts are produced. So far they were only detected in photons. Even though the detection in different wavebands has led to some agreement on what kinds of objects are the source of these bursts, a detection in neutrinos would be essential in solving several questions. There are considerations that high energy cosmic rays are the result of these cataclysmic events. Particle physics dictates that interactions of emitted particles would result in a neutrino flux. These interactions could be either hadronic collisions (pp) or photohadronic interactions ($p\gamma$). Both would lead to the production of neutrinos. As for solar neutrinos, a theoretical prediction of the cosmic neutrino flux, which precedents the detection, would be beneficial for such a measurement. Therefore, a model of the expected fluxes and flux shapes should help in the search for highest energy neutrinos. Today, the calculation of neutrino fluxes profits greatly from the advances in numerical simulations and the precision of high energy particle data.

In this work we present a new simulation algorithm for neutrinos from extragalactic cosmic accelerators. We will take a closer look at GRBs and the neutrinos one can expect from these events. We will first recapitulate the theoretical framework, such as the basic concepts, astrophysical neutrinos and the cosmic sources, on which this work is based. Then we will introduce the NeuCosmA code and how it is used in Monte Carlo simulations. In the third part we reproduce the so-called Waxman-Bahcall flux and show how it changes in case of a more detailed model. After this we discuss the effects of parameter distribution on the diffuse GRB neutrino flux. We then summarize our results and give a short outlook on what still has to be done and what could be done.

2. Basic physics concepts

In the following sections we want to give an overview of the general theoretical aspects of this work. We will give a short introduction into relativity, cosmology and the boost of spectra. Since the phenomena discussed in this work are considered to be relativistic and at cosmologic distances effects of "both" theories of relativity have to be considered. Originally published by A. Einstein in 1905 (Special Relativity; SR), Ref. [12], and 1916 (General Relativity; GR), Ref. [13], the former quickly gained acceptance in the scientific community since SR can describe high energy particle physics and its processes while the latter was long viewed to be too complex. The time of GR came in the 1960s when new developments in mathematics helped to extract measurable results from the Einstein field equations as well as explaining new astronomical phenomena. Today all cosmologic models incorporate principals of GR. In the first two of the following sections we take a look at the effects of Special and General Relativity affecting this work. In the third we discuss the boost of particle spectra and unit conversion.

2.1. Special Relativity

The simple case of Newton's classical mechanics has to be modified when looking at phenomena with velocity $v \lesssim c$. These modifications to mechanics are based on two postulates which are in conflict with classical mechanics:

1. The laws of physics are the same in each reference frame moving at the same speed and in the same direction (in a uniform motion); principle of relativity.
2. The speed of light in vacuum is constant regardless of the reference frame.

Starting from these two postulates Einstein derived a theory of motion that includes several additional effects compared to classical mechanics. Especially the transition between reference frames leads to changes that cannot be described by classical mechanics. For an observer who is at rest relative to an event the event looks different compared to an observer who is moving towards or away from the event. Therefore,

the result of an event depends on the reference frame from which it is viewed. To correctly describe these effects of transformations, it is necessary to consider all objects in 4D spacetime instead of just the 3D space of classical mechanics. Thus, a reference frame has three spatial axes to measure the position as well as a "clock" to measure the time of an event. Using Lorentz transformations it is possible to change between these reference frames.

Let us consider two reference frames: the frame S, in which the clock is at rest, and the reference frame $S^{'}$, which is moving with velocity $\vec{v}$ relative to S. Therefore, the clock of $S^{'}$ is moving. At the point zero the spatial axes and the clocks of both frames coincide. The transition between the two reference frames S, the frame with the clock at rest, and $S^{'}$, the frame with the moving clock, can be described mathematically with the following Lorentz boost:

$$\begin{pmatrix} ct^{'} \\ \vec{r^{'}} \end{pmatrix} = \Gamma(\vec{v}) \begin{pmatrix} 1 & -\vec{v}^{T}/c \\ -\vec{v}/c & \Gamma(\vec{v})^{-1}\,\mathbb{I} + (1-\Gamma(\vec{v})^{-1})\frac{\vec{v}\cdot\vec{v}^{T}}{v^{2}} \end{pmatrix} \begin{pmatrix} ct \\ \vec{r} \end{pmatrix} \quad . \tag{2.1}$$

Here ct is the temporal component of the 4-vector and $\vec{r}$ is the spacial 3-vector. Moreover, the symbol $\mathbb{I}$ represents the (3×3) identity matrix and $\vec{v}^{T}$ is the transposed velocity vector. The Lorentz factor Γ is defined as

$$\Gamma(\vec{v}) = \frac{1}{\sqrt{1-\beta^{2}}} = \frac{1}{\sqrt{1-\frac{|\vec{v}|^{2}}{c^{2}}}} \tag{2.2}$$

with $\beta = v/c$ and is the scalar quantity describing the "strength" of the general Lorentz boost as can be seen in Eq. (2.1). For most of the following calculations only the absolute value of the velocity ($v = |\vec{v}|$) will be of interest and not the direction. Because of this we will use the Lorentz factor Γ instead of the velocity $\vec{v}$ to describe motions and boosts between different reference frames.

The effect of Lorentz transformations between the reference frames in the time component is called time dilation. Due to the relative motion of the reference frames events appear on different timescales. We consider an event in both reference frames. As in the previous paragraph we assume that the clock is at rest for reference frame S while it is moving in reference frame $S^{'}$. Hence, we define the elapsed time between two points to be called Δt (for measurement with the clock at rest; in S) and $\Delta t^{'}$ (for measurement with the moving clock; in $S^{'}$). If the two clocks are synchronized

at the starting point, then the two times are connected as follows:

$$\Delta t = \Gamma \, \Delta t^{'} \quad . \tag{2.3}$$

The time on the moving clock seems to have elapsed slower in comparison to the clock at rest. Applied to particle physics this effect describes the "longer" lifetimes of moving particles for an observer at rest. On the other hand there is also an effect on the spacial component, which is dubbed length contraction. Since the speed of light is the same in all reference frames, it is no longer possible to claim that two events are simultaneous in every reference frame. For a length measurement it is essential to measure both endpoints of a length simultaneously ($\Delta t = 0$ as well as $\Delta t^{'} = 0$). An object, which is at rest in reference frame S, has a length x measured in frame S. If the object is now observed in reference frame $S^{'}$ (and, therefore, moves relative to $S^{'}$), a measurement of its length gives a different value, namely $x^{'}$. x and $x^{'}$ are again connected via Lorentz boosts:

$$x^{'} = \Gamma \, x \quad . \tag{2.4}$$

The time dilation, Eq. (2.3), and the length contraction, Eq. (2.4), are merely the consequence of Lorentz transformations between frames. They describe the effect of the transformations on time or length measurements in a simple way. We will need these simplifications when dealing with the different reference frames in a GRB. The two most relevant frames are the rest frame of the shock (short: SRF) and the observer's frame. The SRF is the comoving frame of reference for our particle interactions and, therefore, for the production of the neutrinos. The observer's frame is as the name suggests the frame of an observer here on Earth. Therefore, the observer's frame equivalent to the frame S of our examples. The SRF is accordingly considered to be the frame $S^{'}$. Hence, primed variables will denote quantities in the SRF and unprimed variables quantities in the observer's frame.

In case the source of a wave and a detector observing the wave move relative to each other there is a shift in frequency called the Doppler effect. This concept of moving source and observer also applies to the change of reference frames. Therefore the general transition between the comoving SRF and the observer's frame can be described with the help of the Doppler factor $\mathcal{D}$. In the classical case the Doppler factor depends on the velocity between source and detector $\beta = \frac{v}{c}$ and (the cosine of) the angle between the line of sight and the direction of motion $\mu = \cos\theta$, while the relativistic speeds require the consideration of time dilation as in Eq. (2.3).

Note that S is equivalent with the observer's frame and $S^{'}$ corresponds to the SRF. The Doppler factor for relativistic beaming can be calculated with the help of the following formula

$$\begin{array}{rcccl} \text{relativistic } \mathcal{D} & = & \text{time dilation} & \cdot & \text{classical } \mathcal{D} \quad , \\ \mathcal{D} & = & \frac{1}{\Gamma} & \cdot & \frac{1}{1-\beta\mu} \quad , \end{array}$$

or as a function of v and θ:

$$\mathcal{D} = \frac{\sqrt{1-\left(\frac{v}{c}\right)^2}}{1-\frac{v}{c}\cdot\cos\theta} \quad . \tag{2.5}$$

As stated before the main difference compared to the classical Doppler effect is the contribution of time dilation. This leads to an additional shift. Due to time dilation, the observed Lorentz boost is approximately 2Γ for a head-on approach ($\theta = 0$) with $v \approx c$, and not Γ. Also, one can easily calculate the classical Doppler factor from Eq. (2.5) for the aforementioned scenario. Without time dilation the Doppler factor would go to infinity which is unphysical. In the next paragraph we will now discuss the angular dependence of the Doppler factor and its effect on the spectra.

Another important result of the relativistic boosting discussed in the previous paragraphs is the distortion of an emitting object. Especially the example of a spherically expanding shell is useful for considerations on GRB in section 4.1. An emitting sphere in the comoving frame, *i.e.* the SRF, will be seen as an ellipsoidical shape for a distant observer when considering the equal arrival time surface. Most radiation arrives from the hemisphere facing towards the observer. The photons are strongly Doppler-boosted inside the light cone $1/\Gamma$. This effect is called relativistic beaming. This was first discussed for radio sources by Rees in Ref. [14] and is depicted in Fig. 2.1. As can be seen from the figure, the radiation from the forward hemisphere dominates the observed flux due to the high boost factors. Inside the light cone with $\theta \leq 1/\Gamma$ the Doppler factor $\mathcal{D}$ is in the range from Γ up to 2Γ. Thus, it is a reasonable simplification to assume $\mathcal{D} \approx \Gamma$ in the forward direction, independent of the viewing angle. The variation is only by a factor of 2 and can therefore be neglected. However, we can only deem this approximation valid, if the radiation is coming really boosted into said light cone.

In the last part of this section we now want to discuss how quantities transform using the Doppler factor $\mathcal{D}$. The connection between times in the SRF $\Delta t^{'}$ and in

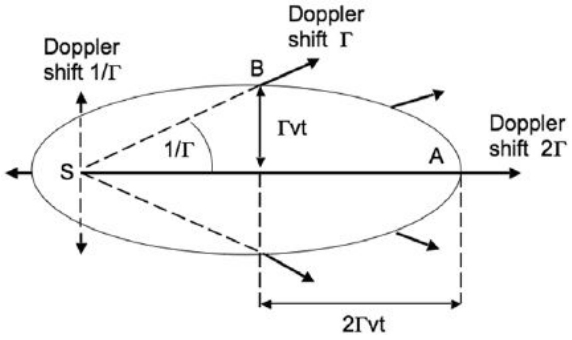

Figure 2.1: The ellipsoid represents the surface of equal arrival for photons emitted from a shell that expands spherically from the point S with $\Gamma = (1 - (v/c)^2)^{-1/2} \gg 1$ as seen by a distant observer (situated far on the right). The major contribution of radiation is coming from the forward (right) hemisphere, which is due to the strong Doppler boosting inside the light cone $1/\Gamma$, see Ref. [14]. The time t in the figure is the observer time.

the observer's frame Δt can now be expressed in terms of the Doppler factor $\mathcal{D}$ as

$$\Delta t = \mathcal{D}^{-1}\, \Delta t' \quad . \tag{2.6}$$

This result is similar to the one given for the time-dilation in Eq. (2.3). However, the Doppler factor describes the change of frame and location from source to detector (including the Doppler effect), while the Lorentz boost only describes a change of reference frame. This distinction is important for emitted radiation or particles. In Ref. [15] the connections between comoving shock rest frame and observer's frame values for further quantities, *e.g.* frequency ν, solid angle Ω, specific intensity $I_\nu(\nu)$ and volume V are expressed with help of the Doppler factor $\mathcal{D}$. Note, according to Ref. [15] the specific intensity $I_\nu(\nu)$ is defined as the energy emitted at a certain frequency per unit time into a solid angle onto a surface area A:

$$I_\nu(\nu) = \frac{\mathrm{d}E}{\mathrm{d}\nu\, \mathrm{d}t\, \mathrm{d}\Omega\, \mathrm{d}A} \quad . \tag{2.7}$$

Remember, this is a quantity defined for radiation (photons). It is similar to the particle flux we will later define. However, the specific intensity as in Eq. (2.7) is the amount of energy emitted as described and not the number of particles, which we need. The derivation of the following transformation relations for the aforementioned

quantities is done in Ref. [15] with relativistic invariants:

$$\nu = \mathcal{D}\,\nu' \quad , \tag{2.8}$$

$$\mathrm{d}\Omega = \mathcal{D}^{-2}\,\mathrm{d}\Omega' \quad , \tag{2.9}$$

$$I_\nu(\nu) = \mathcal{D}^3\, I'_{\nu'}(\nu') \quad , \tag{2.10}$$

$$\mathrm{d}V = \mathcal{D}\,\mathrm{d}V' \quad . \tag{2.11}$$

Note that primed quantities note values in the SRF while unprimed quantities are in the observer's frame. This convention will be used throughout the whole work. We will need these quantities when we discuss the transformation of rates in section 2.3.

2.2. Consequences of current cosmologic models

Since physics is trying to provide a detailed mathematical description of nature, a model describing the largest scales, *i.e.* the whole known universe, is needed as a framework for astrophysics. The current models of cosmology are based on the Einstein field equations derived in 1916. Without going into detail on the field equations themselves, one needs a metric to solve the equations. Since observations indicate that on large scales (above 100 Mpc) the universe is homogeneous and isotropic, the metric of choice is the so-called Friedmann-Lemaître-Robertson-Walker (FLRW) metric

$$\mathrm{d}s^2 = c^2\,\mathrm{d}t^2 - a(t)^2\,\left[\mathrm{d}r^2 + \Sigma(r)^2\,\mathrm{d}\Omega^2\right] \quad . \tag{2.12}$$

Here $a(t)$ is the "scale factor" of the universe as a function of time t. It describes the time-dependence of the distance between two observers and depends only on one length scale. The differential solid angle is defined as $\mathrm{d}\Omega^2 = \mathrm{d}\theta^2 + \sin^2\theta\,\mathrm{d}\phi^2$. The function $\Sigma(r)$ incorporates the curvature of space into the metric. It depends on the sign and value of the curvature, and can be defined as follows (in hyperspherical coordinates, as is Eq. (2.12)):

$$\Sigma(r) = \begin{cases} \sqrt{-k}\,\sinh(r/\sqrt{-k}) & \text{for } k < 0 \\ r & \text{for } k = 0 \\ \sqrt{k}\,\sin(r/\sqrt{k}) & \text{for } k > 0 \end{cases} \tag{2.13}$$

with k being the value of the curvature radius squared.[1] This metric already includes the possibility of a expanding universe, as has been observed by Hubble in Ref. [16].

With this metric it is possible to solve the Einstein field equations leading to the Friedmann equations

$$\begin{aligned} \left(\frac{\dot{a}}{a}\right)^2 &= \frac{8\pi G}{3}\rho - \frac{k\,c^2}{a^2} + \frac{\Lambda\,c^2}{3} \quad . \\ 2\,\frac{\ddot{a}}{a} &= -\frac{8\pi G}{c^2}\,p - \frac{k\,c^2}{a^2} + \Lambda\,c^2 - \left(\frac{\dot{a}}{a}\right)^2 \quad . \end{aligned} \tag{2.14}$$

Here ρ and p are the homogeneous density and pressure of the universe. Newton's constant of gravity is symbolized by G, and Λ is a relic once introduced by Einstein himself. This cosmologic constant was introduced to explain the cosmic expansion. It is still kept in models nowadays since observational results of the cosmic microwave background (CMB) can be fitted best to models with this Λ component. The currently favored set of models is called ΛCDM which are models with Λ and cold dark matter. The common way to define a model is to use a set of energy densities and Hubble's constant. The first Friedmann equation in Eq. (2.14) can be transformed to include these quantities. By defining a vacuum energy density ρ_Λ it is possible to re-write the Λ term to also include a density. With $\rho_\Lambda = \Lambda\,c^2/(8\pi G)$ the first of the Friedmann equations from Eq. (2.14) can be simplified to

$$\left(\frac{\dot{a}}{a}\right)^2 = \frac{8\pi G}{3}\left(\rho + \rho_\Lambda\right) - \frac{k\,c^2}{a^2} \quad . \tag{2.15}$$

The physical interpretation of ρ includes matter (ρ_m) as well as radiation (ρ_γ). Note that all densities can have a time dependence and only today's values can be measured, see Ref. [17]. The values of the densities are nowadays given in a dimensionless form, Ω, as multiples of $\rho_{0,\mathrm{crit}} = 3\,H_0^2/(8\pi G)$ with the index 0 denoting todays ($t = t_0$) values. In recent years the results from the Wilkinson Microwave Anisotropy Probe (WMAP) satellite set quite firm boundaries on the current densities. A description of how the parameters are obtained is given in Ref. [18]. An excerpt from the values derived from the current 7-year data (and other experiments) are found in Table 2.1. These values tell us that matter ($\Omega_m = \Omega_b + \Omega_c \approx 0.27$) and "dark energy" ($\Omega_\Lambda \approx 0.73$) are the dominating contributions to the total energy density in

[1] Depending on the choice of units of k the units of other quantities change. If k is a length^{-2} then r has the unit length and $a(t)$ is unitless. On the other hand if $k \in \{+1, 0, -1\}$ (and unitless) then r is unitless as well and $a(t)$ has the units of length.

Description	Symbol	$WMAP$+BAO+H_0
Hubble constant	H_0	$70.4^{+1.3}_{-1.4}\,\mathrm{km\,s^{-1}\,Mpc^{-1}}$
Baryon density	Ω_b	0.0456 ± 0.0016
Dark matter density	Ω_c	0.227 ± 0.014
Dark energy density	Ω_Λ	$0.728^{+0.015}_{0.016}$
Total density	Ω_{tot}	$1.0023^{+0.0056}_{-0.0054}$

Table 2.1: Excerpt of the current cosmological parameters taken from Ref. [18], the WMAP seven-year report. Except for Hubble's constant all quantities are dimensionless. The first four values are obtained for a flat ($k = 0$) universe while the last entry, Ω_{tot}, is obtained with the possibility of $k \neq 0$. For details on the acquisition see Ref. [18] and references therein. We will use simplified values derived from the ones above. We set $H_0 = 70.5\,\mathrm{km\,s^{-1}\,Mpc^{-1}}$, the matter density $\Omega_m = \Omega_b + \Omega_c = 0.27$ and $\Omega_\Lambda = 0.73$.

a flat ($k = 0$ and $\Omega_{\mathrm{tot}} = 1$) universe. We will use the approximated values for the matter density and the dark energy density, derived from the exact values in Table 2.1. Compared to these two contributions the radiation density Ω_γ is negligible and therefore not included in Table 2.1. When one relaxes the restriction on k and calculates the total energy density Ω_{tot} from observed values it is still close to unity and hence spacetime can be considered to be flat (or of negligible curvature), see Table 2.1.

Apart from changing the distance between two points in space, see Eq. (2.12), the cosmic expansion also leads to an energy shift. Photons are observed at lower frequency compared to the frequency they were emitted with. In terms of optical frequencies they are "red-shifted". Since all energies are affected by this shift the so-called redshift z was introduced. It is defined as

$$z = \frac{\lambda_{\mathrm{obs}} - \lambda_{\mathrm{emit}}}{\lambda_{\mathrm{emit}}} \tag{2.16}$$

with λ_{obs} and λ_{emit} being the observed and the emitted wavelength. By comparing the distance traveled in the expanding spacetime and by assuming that for today $t = t_0$ and $a(t = t_0) = 1$ one obtains the formula connecting the scale factor $a(t)$ with the redshift z

$$a(t) = \frac{1}{1+z} \quad . \tag{2.17}$$

By knowing the redshift z of a distant object and using the framework of the flat ΛCDM cosmology it is possible to calculate the distance between the observer and

an object in the universe. Since we have an expanding spacetime a distance that was defined at one point in time expands with the spacetime (and the scale factor $a(t)$). Thus, it is useful to have a distance measure that is defined at the present cosmological time along a path and is independent from the cosmologic expansion. Such a distance is called comoving distance d_{com} and can be calculated from the redshift z:

$$d_{\text{com}}(z) = \frac{c}{H_0} \int_{\frac{1}{1+z}}^{1} \frac{\mathrm{d}a}{\sqrt{\Omega_m a + \Omega_\Lambda a^4}} \quad . \tag{2.18}$$

The values needed for this formula are the rounded values from Table 2.1, see caption of the table for explanation. c is the speed of light.

Another important distance is the so-called luminosity distance d_L. It connects the luminosity L, the energy output per unit time, of an object at cosmologic distance to the measured flux F on Earth. The classic relation between L and F is given with

$$L_{\text{iso}} = 4\pi\, d^2 \cdot F \quad . \tag{2.19}$$

Here, it is assumed that the flux F is emitted isotropically from a source at distance d. This formula does not hold for objects at cosmologic distances if we insert d_{com} as the distance d. This is because photons loose energy due to the cosmologic redshift as well as being affected by (cosmic) time dilation. This leads to an additional redshift,

$$L_{\text{iso}} = 4\pi\, d_{\text{com}}^2\, (1+z)^2 \cdot F \quad , \tag{2.20}$$

and to the introduction of the luminosity distance,

$$\begin{aligned} d_L &= (1+z) \quad d_{com} \\ &= (1+z) \quad \frac{c}{H_0} \int_{\frac{1}{1+z}}^{1} \frac{\mathrm{d}a}{\sqrt{\Omega_m a + \Omega_\Lambda a^4}} \quad . \end{aligned} \tag{2.21}$$

Before we come to the section on the boost of spectra, it has to be mentioned that the above calculations and distance measures are only valid for $z > 0.023$. The central assumption of these derivations is that the universe is isotropic and homogeneous. As one can tell by looking into the sky at night, this is not the case for structures like our galaxy. Structures of stars or clusters of galaxies are anisotropic. However, sky surveys have shown that above 100 Mpc structures begin to be distributed evenly in space, see *e.g.* Ref. [17]. These 100 Mpc translate into a minimum redshift of $z_{\text{min}} \simeq 0.023$ (for luminosity distance) with help of Eq. (2.21) and the

values from Table 2.1. Therefore, only bursts with $z > 0.023$ should be included in the discussion of cosmic sources since smaller structures are not isotropic.

2.3. Relativistic boost of particle spectra and transformation of rates

As mentioned before our calculations will be done in two different reference frames. The production of the particles is best described in the shock (or bulk) rest frame (SRF), but experimental results can only be taken in the observer's frame (Obs). As noted in section 2.1 Lorentz transformations, as defined in Eq. (2.1), connect values from both frames. For the general astrophysical case one has to consider the relativistic Lorentz factor Γ as well as the energy loss due to the cosmological expansion, expressed through the redshift z.

$$x_{Obs} = x^{'} \cdot \Gamma^{-1} \cdot (1 + z) \tag{2.22}$$

Here x_{Obs} is a length in the observer's frame along the direction of the boost, while $x^{'}$ is the comoving length in the SRF. Mind, that our notation for quantities in the two different frames will be such that primed ($'$) quantities are in always in the SRF and unprimed quantities are in the observer's frame. The way elements in the normal plane of the boost are not affected by the Lorentz factor, see Eq. (2.1) (for motion along one axis). However, they are nonetheless subject to the cosmic expansion. For other values it is advisable to use relativistic invariants depending on the relativistic Doppler factor $\mathcal{D}$ as described in Ref. [15], see Eqs. (2.8) - (2.11). Those equations need to be extended with a contribution from the cosmological redshift. For energy and specific intensity this results in the following formulas:

$$E_{Obs} = E^{'} \cdot \mathcal{D} \cdot (1 + z)^{-1} \tag{2.23}$$

$$I_{\nu,Obs} = I^{'}_{\nu} \cdot \mathcal{D}^3 \cdot (1 + z)^{-3} \quad . \tag{2.24}$$

The changes due to the cosmological expansion have to be considered carefully, since the effect of the cosmic expansion is not the same as the effect of the Lorentz boost. However, the scale factor already describes the effect and from Eq. (2.17) one gets the "cosmological component" for the transformations.

The limitation of the possible visibility of an event is another effect of the transition of reference frames.. Current observational data and also constraints from energetic considerations suggest that gamma-ray bursts are generated by relativistic jets, similar to jets of active galaxy nuclei (AGN). Assuming an outflow in two diametrical jets, the maximal angle in the SRF under which the outflow of one jet can be seen from the direction of the observer is $\theta_{\mathrm{SRF}} = \frac{\pi}{2}$. Higher values can be neglected since emission from the second jet would be observed under a smaller viewing angle θ_{SRF}. Using the relativistic aberration formula

$$\cos\theta_{\mathrm{Obs}} = \frac{\cos\theta_{\mathrm{SRF}} + \beta}{1 + \beta\ \cos\theta_{\mathrm{SRF}}} \tag{2.25}$$

for a moving source one can calculate the value of $\theta_{\mathrm{Obs},\mathbf{max}}$. This angle is the largest angle for which the relativistic outflow can be observed. It, therefore, reduces the number of observable sources, and, also, sets a boundary to the properties of the jet, *i.e.* the jet opening angle θ_j. For $\theta_{\mathrm{SRF}} = \frac{\pi}{2}$ the cos disappears and the equation can be re-written to the form

$$\begin{aligned} \theta_{\mathrm{Obs},\mathbf{max}} &= \arccos(\beta) = \arcsin\left(\frac{1}{\Gamma}\right) \\ &\approx \frac{1}{\Gamma} \quad . \end{aligned} \tag{2.26}$$

The last approximation is the result of the series expansion of $\arcsin\left(\frac{1}{\Gamma}\right)$ and valid for large Lorentz boost factors Γ. If one compares this to the opening angle of the relativistic beaming in Fig. 2.1, then one sees that the maximum observable angle $\theta_{\mathrm{Obs},\mathbf{max}}$ is equal the opening angle of our relativistically beamed light cone. Hence, as long as the jet opening angle θ_j is larger than $1/\Gamma$, the approximation of the emitting sphere still applies even for emission from jets. Moreover, we can use the simple approximation of a constant boost factor $\mathcal{D}$ inside the jet. Therefore, it is common in the literature to use

$$\mathcal{D} = \Gamma \quad . \tag{2.27}$$

We will also adept this simplification for our simulations and will not consider the effect of the viewing angle explicitly. Thus, the Doppler factor $\mathcal{D}$ simplifies to the Lorentz factor Γ. However, the angular dependence may be of interest at some point in the future, and, therefore, we will treat the boosts in these introductory chapters as general possible. Hence, Eq. (2.27) applies to all of the following transformations.

We now want to explain how the different kinds of spectra in our work transform.

Therefore, we first need a definition of the different spectra. We will be using three different kinds of particle flux spectra, two at the source and one at the observer. The first spectrum Q is the spectrum per unit time at the source, and in the SRF. It is given in units of $\mathrm{GeV}^{-1}\,\mathrm{s}^{-1}\,\mathrm{cm}^{-3}$. The second spectrum N is the time-integrated spectrum, *i.e.* opposite to Q N has no dependence per unit time, at the source, and in the SRF. The units of this spectrum are $\mathrm{GeV}^{-1}\,\mathrm{cm}^{-3}$. The third spectrum is denoted as ϕ in this work. This is the flux spectrum at the observer, in the observer's frame, in $\mathrm{GeV}^{-1}\,\mathrm{s}^{-1}\,\mathrm{sr}^{-1}\,\mathrm{cm}^{-2}$. If ϕ appears in the shock rest frame, it will be denoted as ϕ', following our convention of primed and unprimed quantities. [2]

The basic procedure in our calculations will be to compute the spectrum per unit time Q from the steady (read: "no dependence per unit time") spectrum N. Details on how this computation is done can be found in section 5.1. The resulting Q then has to be boosted to the observer's frame to match a spectrum at a detector, ϕ. Unfortunately there is also a difference in units between Q and ϕ. Q depends on the volume while ϕ depends on the area and the solid angle. The standard procedure for this kind of unit conversion is described in Ref. [19]:

$$\phi = \frac{c}{4\pi} \cdot N \quad . \tag{2.28}$$

As can be seen from Eq. (2.28) this method only applies to the steady spectrum (without dependence on unit time) N and not to Q. We, therefore, need another way to calculate the unit conversion. We will divide the conversion into three steps. The first is to loose the volume dependence via integration. The second step is to include the dependence on solid angle. And as the third and final step the dependence on the surface area is introduced. The integration over the volume can be simplified, if we assume a spherical symmetry for the emission region as well as an emission which is independent of the location inside the source. Then the integration simplifies to a multiplication with the volume of a sphere ($V = \frac{4\pi}{3}\, r^3$). The radius of the emission region r does not affect the results since we introduce a total normalization. Moreover, we assume that the radius is large enough to not lead to additional effects, such as *e.g.* the particles cannot be accelerated because magnetic field and radius have unsuitable values, see Ref. [20] for a discussion of these effects. The dependence on the solid angle can be obtained by simple division by 4π because the emitted flux is assumed to be of isotropic origin. The dependence

[2] The flux ϕ is sometimes denoted as $\mathrm{d}N/\mathrm{d}E$ in the literature, but this notation is misleading since it neglects the differentials of solid angle, time and surface area. Note that in this notation N is the number of particles, and not our spectrum without a dependence on the unit time.

on the surface area is included by assuming that the flux is now through a sphere with radius d_L, reflecting the distance between source and observer.[3] Hence, the total unit conversion is

$$\begin{aligned} \phi' &= \frac{1}{4\pi\, d_L^2} \cdot \frac{1}{4\pi} \cdot \left(\frac{4\pi}{3}\, r^3 \right) \cdot Q \\ &= \frac{r^3}{12\pi\, d_L^2}\, Q \quad . \end{aligned} \tag{2.29}$$

However, we still need to take the effects of relativistic boosting into account. Thus, we need to know how ϕ' (in SRF) transforms to ϕ in the observer's frame. The appropriate power of the Doppler factor, describing the boost of the spectrum ϕ, can be derived from the dependencies included in the spectrum:

$$\phi = \frac{\mathrm{d}N}{\mathrm{d}E\, \mathrm{d}t\, \mathrm{d}\Omega\, \mathrm{d}A} \quad . \tag{2.30}$$

Here N is the particle number, E is the energy, t the time, Ω the solid angle and A the surface area. The number of particles N and the surface area A perpendicular to the direction of the boost are unaffected from the Lorentz boost. However, the energy E transforms in the same way as the frequency ν in Eq. (2.8), since the energy of a quantum, *e.g.* a photon, can be expressed as the product of Planck's constant and its frequency, see Ref. [22]. Moreover, the solid angle Ω transforms as described in Eq. (2.9), and the time t as in Eq. (2.6). By combining all the components as described by Eq. (2.30) we obtain that

$$\phi = \mathcal{D}^2\, \phi' \quad . \tag{2.31}$$

Note that we do not need the "extended" Doppler factor. Even if the reasoning of the derivation slightly changes for z, the solid angle Ω is not changed by the redshift while A is, the result for the cosmic expansion is as expected $(1+z)^{-2}$. But the effect of the cosmic expansion is already accounted for by the luminosity distance d_L as part of the surface area A in the transformation in Eq. (2.29). As part of A, d_L is not affected by the Lorentz boost.[4]

[3] As one might tell, Eq. (2.21) does not give an analytic expression for the chosen values from Table 2.1. Therefore, we approximate the result from $z = 0$ to $z = 6$. The upper bound is the current bound of star formation rate considerations taken from Ref. [21].

[4] It may be more reasonable to first boost the spectrum and then divide it by $4\pi\, d_L^2$. However, the two steps are independent, when d_L is assumed to be part of the area A perpendicular to the direction of the boost. Therefore, the calculation factorizes and both steps can be interchanged, as we have done in our derivation.

3. Astrophysical neutrinos

The field of neutrino astronomy is a field with high potential. As reported in reviews such as Refs. [23, 24] the properties of neutrinos open a whole new detection range and insight on astrophysical sources. The great advantage of neutrinos comes from their lack of attunement and from the fact that they are not deflected by magnetic fields. Therefore, it is in principle possible to detect signals not accessible by conventional means, such as photons or cosmic rays. However, we have to understand where and at which energies neutrinos are produced, in which kind of sources, and from which interactions. Thus, we will first recapitulate the possible sources for astrophysical neutrinos. Then, we re-iterate the interactions leading to neutrino production in these sources. In the third section of this chapter we discuss the mass of neutrinos and the resulting effects on the propagation through space. In the last section we will consider the different detection mechanisms available for the high energy neutrinos.

3.1. Sources of astrophysical neutrinos

As stated in reviews such as Refs. [23, 24], there are potentially lots of interesting astrophysical sources of high-energy neutrino. In the widest sense every kind of source with non-thermal emission qualifies as such a neutrino source. These kind of spectra normally characterize a source far away from thermodynamic equilibrium and is a sign of highly efficient particle acceleration. The non-thermal spectra are associated with powerful supersonic outflows, as those seen in supernova remnants, gamma-ray bursts, or galactic and extragalactic radio jets, which lead to particle acceleration at shock waves. The general process leading to the non-thermal emission is assumed to be Fermi acceleration. This kind of diffusive shock acceleration, developed by Krymskii and by Axford et al, utilizes repeated scattering between magnetic mirrors. For details on the process see Ref. [23] and references within. As already mentioned in the introduction mainly pp and $p\gamma$ interactions of the accelerated particles will lead

to the production of neutrinos. We will discuss the interaction chains leading to neutrinos in more detail in section 3.2. According to Ref. [23] the possible sources of the cosmic rays participating in the interactions can be divided in galactic candidates, such as pulsars and pulsar-driven nebulae, shell-type supernova remnants, and black hole candidates and microquasars, and extragalactic candidates, such as active galaxy nuclei (AGN), galaxy clusters and gamma-ray bursts (GRB). In this work we will focus on GRB and will give a more detailed description of these events in section 4.1.

As for the expected diffuse neutrino flux from cosmic sources there have been several estimates in the past. The general scheme of these estimates is to calculate the neutrino flux by assuming photohadronic interactions between the observed ultra-high energy cosmic rays (UHECR) and the observed photon spectra of cosmic sources or by proton-proton interactions of cosmic rays, see Refs. [25] and [26]. While the model by Waxman and Bahcall (WB) is calculated by assuming a particular model spectrum for cosmic rays, the one from Mannheim, Protheroe and Rachen (MPR) orientates more on the experimental data on protons and gamma-rays available at the time of the publication of Ref. [26]. In both models the strongest bounds can be derived by assuming that the sources are transparent to neutrons. However, both have their advantages and disadvantages. Namely, WB can describe a certain type of source well, *i.e.* GRB with an E^{-2} proton spectrum together with a Band function for the photon spectrum. Furthermore, it has a strong GZK cut-off, which is fairly consistent with data from the High Resolution Fly's Eye Experiment (HiRes), see Ref. [27], and the *Auger* International Collaboration, see Ref. [28]. However, this treatment by Waxman and Bahcall does not reproduce the steep slope of the observed cosmic ray spectrum below $\sim 10^{10}\,\mathrm{GeV}$. On the other hand the MPR treatment does include these features, it is however centered more on the observational data up to $10^{11}\,\mathrm{GeV}$ (and not specifically single sources), even though modifications to analyze different sources, such as several types of AGN or GRB, have been done, see Ref. [26]. Both estimates give the same result in the energy range between $10^7\,\mathrm{GeV} \leq E_\nu \leq 10^9\,\mathrm{GeV}$, but at higher and lower energies the MPR result is higher than the WB prediction. This can be seen in Fig. 3.1, which is taken from Ref. [26]. However, for our theoretical calculation of GRB neutrinos including the detailed treatment of the particle physics the derivations by Waxman and Bahcall [25] are better suited, since they can be applied to single sources and give a prediction of the flux shape. The estimates of Waxman and Bahcall, taken from Ref. [25], are currently considered a simple approximation of the neutrino flux stemming from the

prompt emission of GRBs.

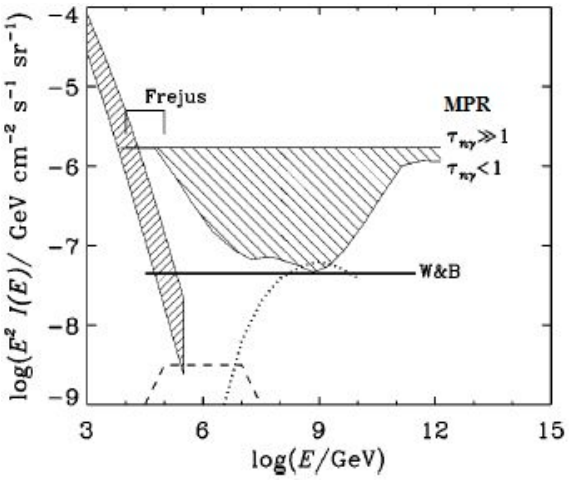

Figure 3.1: The bounds of the (muon) neutrino flux derived from considering the cosmic ray spectra as well as gamma-ray observations, taken from Ref. [26]. The figure shows the bound derived by Mannheim, Protheroe and Rachen (MPR) for different optical depth of neutrons, and the bound derived by Waxman and Bahcall (W&B). Furthermore, the Waxman-Bahcall GRB neutrino flux, stated to be taken from Ref. [25], is shown as a dashed curve.

3.2. Assumed production mechanisms for astrophysical neutrinos

Neutrinos in general are produced in weak interactions. In astrophysical sources these can be part of several processes, or decay chains. First of all they are a byproduct of the nuclear fusion in stars. These neutrinos have low energies for astrophysical standards ($\sim$ eV). Neutrinos with higher energy are presumably produced in proton-proton (pp) collisions and/or photohadronic ($p\gamma$) interactions in shock fronts. Here, the neutrinos are the product of the decay of (charged) pions. The leading contribution from pp interactions is

$$p + p \rightarrow \begin{cases} p + n + \pi^+ & 1/3 \text{ of all cases} \\ p + p + \pi^0 & 2/3 \text{ of all cases} \end{cases} , \tag{3.1}$$

as described in Ref. [24]. The interactions between the cosmic rays and the photons (photohadronic interactions) are in leading order approximated with the so-called

Δ-resonance. The simple reaction chain for the production and decay of the Δ-resonance is the following:

$$p + \gamma \to \Delta^+ \to \begin{cases} n + \pi^+ & 1/3 \text{ of all cases} \\ p + \pi^0 & 2/3 \text{ of all cases} \end{cases} . \tag{3.2}$$

Both kinds of interactions lead to neutrinos, if charged pions are produced as intermediate particles. (See Eq. (3.3) for more details on the production of neutrinos.) The same kind of processes can also occur for incident neutrons, which leads to π^- additionally. Furthermore, Ref. [24] mentions the possibility of kaons production at high energies as well as high energy processes leading to multiple pions.

For a realistic computation of the neutrino spectra from astrophysical accelerators one also has to include these further interaction channels. In this work we want to focus on photohadronic interactions. In addition to the Δ-resonance we also include higher resonances, the direct (t-channel) production of pions as well as multi-pion production as in Ref. [29]. We then consider the weak decays of pions, muons, kaons and neutrons into neutrinos as

$$\begin{aligned} \pi^+ &\to \mu^+ + \nu_\mu \,, \\ &\quad \mu^+ \to e^+ + \nu_e + \bar{\nu}_\mu \,, && (3.3) \\ \pi^- &\to \mu^- + \bar{\nu}_\mu \,, \\ &\quad \mu^- \to e^- + \bar{\nu}_e + \nu_\mu \,, && (3.4) \\ K^+ &\to \mu^+ + \nu_\mu \,, && (3.5) \\ n &\to p + e^- + \bar{\nu}_e \,. && (3.6) \end{aligned}$$

These decay channels are sometimes mentioned in the literature, but their discussion is generally restricted to how synchrotron cooling affects each particle species differently, as in *e.g.* Ref. [30]. To ensure a correct simulation of the neutrino spectra, we have to calculate the synchrotron losses for each intermediate particle species. Because of this we cannot integrate out the intermediate particles, as explained in Ref. [29]. Moreover, this allows us to include the P (parity-) symmetry breaking properties of weak interactions in the calculation of the decays. Experimental results have shown that the weak force only couples to left-handed (LH; helicity $+1/2$) particles or right-handed (RH, helicity $-1/2$) anti-particles. This has consequences for the decay of particles, *e.g.* weakly interacting neutrinos are always either left-handed neutrinos or right-handed antineutrinos. In particular, we adopt the helicity

dependent decay of muons from Ref. [31].

3.3. Effects of propagation through space on neutrinos

In the last two decades experiments with solar, atmospheric, reactor and accelerator neutrinos showed that there was an unusual discrepancy between the expected and the observed flux of neutrino. The description of this effect was adopted from the quark sector of the SM and led to the introduction of the transition among different neutrino flavors ν_e, ν_μ, ν_τ (antineutrinos $\bar{\nu}_e$, $\bar{\nu}_\mu$, $\bar{\nu}_\tau$) in flight. The latter implies that neutrino flavor states can mix due to the flavor states not being equal to the mass eigenstates. This can be described by connecting the flavor states $|\nu_\alpha\rangle$ with $\alpha = e, \mu, \tau$ to the mass eigenstates $|\nu_j\rangle$ via a mixing matrix, see Ref. [32],

$$|\nu_\alpha\rangle = \sum_j U^*_{\alpha j} |\nu_j\rangle \quad . \tag{3.7}$$

$U_{\alpha j}$ is a unitary neutrino mixing matrix. Before we can define $U_{\alpha j}$ we need to know how many mass eigenstates $|\nu_j\rangle$ need to be considered. With the exception of the LSND result all current neutrino oscillation data can be described by neutrino mixing with three mass eigenstates in vacuum. From these results one can obtain that three neutrinos ν_j, *e.g.* ν_1, ν_2 and ν_3, must be light, $m_{1,2,3} \lesssim 1\,\text{eV}$, and not equal, $m_1 \neq m_2 \neq m_3$.[1] Unfortunately the results of current experiments only limit the total neutrino mass, *e.g.* $m_\nu < 2\,\text{eV}$ from tritium decay experiments [5], or set boundaries on the mass difference Δm^2 in the 3-neutrino mixing scheme, taken from Ref. [5],

$$\begin{aligned} \Delta m^2_{21} &= m^2_2 - m^2_1 = (7.59 \pm 0.20) \cdot 10^{-5}\,\text{eV}^2 \quad , \\ |\Delta m^2_{31}| &= |m^2_3 - m^2_1| = (2.43 \pm 0.13) \cdot 10^{-3}\,\text{eV}^2 \quad . \end{aligned} \tag{3.8}$$

The difference Δm^2_{21} is obtained from detailed calculation and measurement of solar neutrinos. In theory the chains of nuclear fusion only produce ν_e, however, the measured flux of ν_e on the Earth coming from the Sun is significantly lower than

[1] There is still the possibility of "sterile" neutrinos, but we will not consider this more general case in this work. This is justifiable since to this point there is no strong evidence that there are more than three light neutrinos.

expected compared to calculations without flavor mixing. This discrepancy can be described with transitions among neutrino flavor states and, hence, can be calculated. On the other hand neutrinos can also be produced by interaction of cosmic rays with the Earth's atmosphere. The detection of these atmospheric neutrinos allowed for calculation of $|\Delta m^2_{31}|$.

One of the most fundamental questions that cannot be determined with current data is the question of the "nature" of neutrinos, *i.e.* if neutrinos are Dirac or Majorana fermions. Since neutrinos have no electric charge they can in principle be their own anti-particle since anti-particles are defined as the electric charge conjugate of a particle, *e.g.* positron e^+ (anti-particle) to electron e^- (particle). If there is a lepton charge L carried by the neutrino ν_α, which is conserved in particle interactions, then there would be distinguishable neutrinos ν_α and antineutrinos $\bar{\nu}_\alpha$ with opposite lepton charge; *e.g.* $L(\nu_\alpha) = +1$ and $L(\bar{\nu}_\alpha) = -1$. On the other hand if such a lepton charge is not conserved, neutrinos could be Majorana particles. A massive Majorana particle χ is identical with its anti-particle $\bar{\chi}$; $\chi \equiv \bar{\chi}$.

In the following studies we will treat neutrinos as Dirac fermions. We assume three generations of light neutrinos and will not include other possible effects (*e.g.* from sterile neutrinos) in this work. The unitary mixing matrix for $n = 3$ parameterized as in Eq. (3.9) is called the Pontecorvo-Maki-Nakagawa-Sakata (PMNS) matrix U_{PMNS}. Here, the rows represent the flavors e, μ and τ, and the columns the mass eigenstates 1, 2 and 3, taken from Ref. [33],

$$U_{\mathrm{PMNS}} = \begin{pmatrix} c_{12}c_{13} & s_{12}c_{13} & s_{13}\mathrm{e}^{-\mathrm{i}\delta} \\ -s_{12}c_{23} - c_{12}s_{23}s_{13}\mathrm{e}^{-\mathrm{i}\delta} & c_{12}c_{23} - s_{12}s_{23}s_{13}\mathrm{e}^{-\mathrm{i}\delta} & s_{23}c_{13} \\ s_{12}s_{23} - c_{12}c_{23}s_{13}\mathrm{e}^{-\mathrm{i}\delta} & -c_{12}s_{23} - s_{12}c_{23}s_{13}\mathrm{e}^{-\mathrm{i}\delta} & c_{23}c_{13} \end{pmatrix} \quad (3.9)$$

In this equation the following short hand conventions are used: $c_{ij} = \cos(\theta_{ij})$ and $s_{ij} = \sin(\theta_{ij})$ are the cosine and the sine of the neutrino mixing angle θ_{ij}, $i, j = 1, 2, 3$. δ is the CP violating (Dirac) phase. Note that in this parameterization the effect of δ (also called δ_{CP}) is connected to θ_{13}.

For the results presented in this work we include the values of the mixing angles from the update of Ref. [34] in February 2010. The best fit values are given in Table 3.1 with 1σ errors, as in Ref. [34], together with the mixing angles use for our calculations. The results in Table 3.1 are obtained for a three-flavor neutrino oscilla-

Parameter	best fit	mixing angle	derived value
$\sin^2\theta_{12}$	$0.318^{+0.019}_{-0.016}$	θ_{12}	0.599
$\sin^2\theta_{23}$	$0.50^{+0.07}_{-0.06}$	θ_{23}	$\frac{\pi}{4}$
$\sin^2\theta_{13}$	$0.013^{+0.013}_{-0.009}$	θ_{13}	0

Table 3.1: The first two columns represent the best fit values with 1σ errors for the three-flavor neutrino oscillation parameters, taken from Ref. [34]. These results are derived from global data including solar, atmospheric, reactor (KamLAND and CHOOZ) and accelerator (K2K and MINOS) experiments, according to Ref. [34]. The last two columns, however, are the values for the mixing angles we use in our work. These values are derived from the best fit values in the second column. The precision of the chosen angles is on purpose higher than the current experimental precision. The value $\theta_{13} = 0$ is not exactly the best fit value, but a reasonable simplification to avoid effects of CP violation in flavor mixing, see Eq. (3.9).

tion scheme from global data including solar, atmospheric, reactor (KamLAND and CHOOZ) and accelerator (K2K and MINOS) experiments. The values of the angles θ_{12} and θ_{23} are obtained by calculating the angles from the best fit values of $\sin^2\theta$ (second column of Table 3.1). These values are $\theta_{12} = 0.599$ and $\theta_{23} = \frac{\pi}{4}$. However, the value for θ_{13} is set to 0 for simplicity reasons. This confinement of θ_{13} allows to set the CP-violating phase δ to an arbitrary value, since it no longer has an effect on the flavor mixing, see Eq. (3.9).

For the correct calculation of the expected neutrino flux from cosmic accelerators it is mandatory to include neutrino mixing, as described in Eq. (3.7). In the case of cosmological neutrinos it is sufficient to take averaged oscillation probabilities since distances are long enough to have a loss of coherence and, therefore, no more transitions among mass eigenstates. A more detailed discussion of this can be found in section 6.3. In the simple case of three neutrino flavors and three mass eigenstates without any initial unstable states the probability of a neutrino of flavor α being detected as a neutrino of flavor β is

$$P_{\alpha\beta} = \sum_j |U_{\alpha j}|^2 |U_{\beta j}|^2 \quad , \tag{3.10}$$

taken from Ref. [35]. $U_{\alpha j}$ are entries of U_{PMNS} from Eq. (3.9). The flavor indices α and β can be e, μ or τ, and mass state index is $j = 1, 2, 3$. Using Eq. (3.10) we calculate all unique combinations of $P_{\alpha\beta}$ needed and implement them in our c-code. Since currently no τ (or ν_τ) is produced from the discussed processes, see

Eqs. (3.3)-(3.6), $P_{\tau\tau}$ was not included into the source file. The full formulas of the detection probabilities can be found in the Appendix B. By multiplying the detection probability P with the boosted flux spectra ϕ one can calculate the expected flux after flavor mixing,

$$\phi_{\nu_\alpha} = \sum_\beta P_{\alpha\beta}\phi_{\nu_\beta} \quad . \tag{3.11}$$

3.4. Detection methods for astrophysical neutrinos

The detection of neutrinos is highly limited by the small interaction cross section of neutrinos. Since neutrinos only participate in weak interaction processes the number of processes that can be used for detection is relatively small. The commonly used methods include the detection of secondary leptons, Cherenkov radiation or characteristic photons from secondary (annihilation) processes. For low energy (reactor) neutrinos β-capture is the commonly used detection method, see Eq. (1.1). As described in Ref. [3] this method yielded the first positive neutrino signal. Here the flash from e^+e^- pair annihilation needs to be detected as well as a signal from the slow neutron. In case of neutrinos with higher energies this and similar detection methods are no longer sufficient.

For these neutrinos with higher energy other techniques are needed. As stated in Ref. [23] astrophysical neutrinos with energies $E_\nu \geq 100\,\mathrm{MeV}$ are considered to be high-energy and need special telescopes to be observed. The strongest limiting factor today as stated by the authors in Ref. [23] is not necessarily the technique, but the cost of the detector. To reach a sufficiently high sensitivity an effective area of $1\,\mathrm{km}^2$ is needed. Just the cost for the detectors can therefore easily reach several US $ 100 million, assuming US $ $100/\mathrm{m}^2$ (numbers taken from Ref. [23]). Still there are several viable methods to detect neutrinos. The currently most prominent one is the detection of Cherenkov radiation in a transparent medium, such as ice or water. The Interaction of a neutrino with a nucleon can lead to the production of the charged lepton associated to the neutrino, see *e.g.* Eq. (1.1). If the velocity of a charged particle, *e.g.* a muon, is higher than the speed of light in the medium then the atoms along the path of the particle are first polarized and then relax rapidly leading to radiation. Even though the production of the charged leptons is possible for all three flavors, Cherenkov telescopes generally measure the tracks of muons. This is due to the relatively long life time of the muons (compared to taus) and their ability to polarize the medium well (compared to electrons), leading to a clear

Cherenkov signal at these energies ($E_\nu \geq 100\,\mathrm{MeV}$). The lifetime of the muons in this energy range is long enough to detect the propagation track of the muon. The reconstruction of the track can give directional information on the origin of the neutrino. The uncertainty of the reconstruction depends on the used detector medium, the intrinsic detector resolution and on the kinematics of the interaction. The resolution is of the order of $1\,^\circ$ for IceCube in the Antarctic ice, taken from Ref. [36], and $0.3\,^\circ$ for Antares in the Mediterranean Sea, see Ref. [37]. The interactions themselves, as described by particle physics, do not give a fixed result for the energies and the momentum. Thus, the kinematics of the interaction always includes an additional uncertainty independent from the detector. However, for the purpose of detecting point sources the directional information is of great value. Electrons from ν_e also produce Cherenkov radiation, but the signal from electrons is much fuzzier and full of dots rather than a track. Also the Cherenkov radiation could be observed in the radio window (below 100 MHz) or via acoustic detection.

Another possibility is the detection of shower or cascade events. As stated in Ref. [38] this could be used to gain additional information. All flavors of neutrinos can participate in neutral current interactions, creating a hadronic shower. However, ν_e can also produce an electromagnetic shower through charged current interactions. Theoretically it is possible to distinguish electromagnetic from hadronic showers by comparing their muon content. In electromagnetic showers muons are absent, while they occur in hadronic showers. However, it is not considered to be experimentally viable at the moment. Nevertheless, a direct measurement of the electromagnetic and the hadronic shower would be sufficient to recreate the total shower energy and, therefore, the energy of the ν_e. In case of ν_μ, the charged current interaction leads to the production of a muon and a shower. However, due to the long lifetime of high energy muons, the muon track always extends beyond the shower. Thus, these showers can be discriminated and do not contribute to the shower rate. For the third flavor, ν_τ, the result of the interaction are a hadronic shower and a tau track, similar to a muon event. Unfortunately, the decay path length of taus is $\Gamma c\tau_\tau \sim 50(E_\tau/\mathrm{PeV})\,\mathrm{m}$, with τ_τ the lifetime of the tau, taken from Ref. [38]. This is so short that below a few PeV the decay of the tau cannot be distinguished from the hadronic shower. Therefore, it is possible that the resulting particles also contribute to the shower rate. According to Ref. [5] roughly 50% of the tau decays lead to hadronic events. Moreover, the channel $\tau^- \to \mu^- + \bar{\nu}_\mu + \nu_\tau$ accounts for $(17.36\pm0.05)\,\%$, taken from Ref. [5]. This can lead to an additional muon track event. However, if the energy of the tau is even higher, the track of the tau should extend

beyond the shower. The ensuing decay of the tau would create a second shower. Such double showers are called double-bang and lollipop events, see Ref. [38] for a discussion. There are several possibilities to detect a shower. Either, photoelectrons from the shower can be detected in a Cherenkov photon detector, such as IceCube. The photoelectrons are distributed over a sphere with a $\sim 100\,\mathrm{m}$ radius for a TeV shower. For a detection, the shower must at least be partially in the detector volume. Since the size of a shower is much smaller than the range of a muon track the effective volume for such a detection is much smaller compared to track events. Or alternatively, the detection of the (nearly) horizontal extensive air showers (EAS) in the atmosphere can be used to detect neutrino events at energies above EeV. The measurement of the EAS can be accomplished by using Cosmic Ray detectors, such as the *Pierre Auger Observatory*, or with pixelated optical detectors monitoring the dark night sky for nitrogen fluorescence, a method developed by the Fly's Eye group, discussed in Ref. [23]. However, these events have to be separated from the atmospheric showers, and again the effective volume for horizontal air showers is rather small. In general, the detection of a shower event is less likely than the detection of a track event. To reach comparable event rates in Cherenkov photon detectors such as IceCube a much larger detector volume would be needed. Then it should even be possible to directly detect double bang or lollipop events from taus, see Ref. [38]. When it is possible to distinguish the different neutrino flavors, it is helpful to define some new observables, that, according to Ref. [39], have to fulfill the following two requirements:

1. They take into account the unknown flux normalization.
2. They take into account the detector properties.

A popular choice complying the first condition are so-called flavor ratios. These are ratios of the fluxes at the detector between different flavors. Their main advantage is that in case of the ratios the flux normalization cancels. The experimentally easiest ratio to obtain is the ratio of muon track to shower events, taken from Ref. [40]:

$$R = \frac{\phi_{\bar{\nu}_\mu+\nu_\mu}}{\phi_{\bar{\nu}_e+\nu_e} + \phi_{\bar{\nu}_\tau+\nu_\tau}} \quad . \tag{3.12}$$

Here, ϕ is the flux at the detector, with contributions from neutrinos and antineutrinos summed over. The summation of ν_e and ν_τ is equivalent with the non-discrimination of electromagnetic and hadronic showers. As stated before, this ratio is limited by the number of detected shower events as well as the background of atmospheric particle showers and neutral current showers. As a second observable

the ratio of electron neutrino to tau neutrino can be defined:

$$S = \frac{\phi_{\bar{\nu}_e+\nu_e}}{\phi_{\bar{\nu}_\tau+\nu_\tau}} \quad . \tag{3.13}$$

This corresponds to the number of electromagnetic to hadronic showers, or electromagnetic showers to double bang or lollipop events, if the tau track can be resolved. This is, however, experimentally far more complicated than to measure the ratio R. Furthermore, the so-called Glashow resonance $\bar{\nu}_e + e^- \to W^- \to ...$ at about 6.3 PeV may be used for (electron) antineutrino identification. This can be used to define

$$T = \frac{\hat{\phi}_{\bar{\nu}_e}}{\phi_{\bar{\nu}_\mu+\nu_\mu}} \quad , \tag{3.14}$$

which represents the ratio of Glashow resonance electron antineutrino events (described by $\hat{\phi}_{\bar{\nu}_e}$) to the muon tracks. Note that the above ratios are somewhat idealized quantities. They neglect neutral current processes, different statistics between numerator and denominator, and backgrounds. Therefore, results from these flavor ratios have to be interpreted with care. There have been numerous studies in the literature utilizing these ratios to look for new physics effects, see Ref. [41] for a review. However, in this work we will only focus on the flavor ratio R, as in Eq. (3.12). We will use this ratio to classify the GRB emission depending on energy, and take the source classes from Ref. [20] as reference, see the Appendix C. Moreover, we discuss what information could be obtained from such a flavor ratio measurement.

After all these methods of detecting high energy neutrinos, we now want to mention the current experimental bound on the cosmic neutrino flux. There are several experiments probing the cosmic neutrino flux. However, up to now there has been no detection of such a neutrino flux. Thus, the current 90% C.L. bound from IceCube for a generic E^{-2} spectrum, see Ref. [42], is set to

$$E_\nu^2 \phi_\nu \leq 8.9 \cdot 10^{-9} \text{ GeV cm}^{-2} \text{ s}^{-1} \text{ sr}^{-1} \quad . \tag{3.15}$$

4. Gamma-ray bursts as astrophysical neutrino sources

In the following chapter we discuss one of the potential astrophysical sources in more detail: gamma-ray bursts. We will recount the general considerations for astrophysical neutrino sources and give estimates of the diffuse flux. We will establish the general concept of a GRB, which will be used in the later simulations, and we take a look at the distribution of measured parameters.

4.1. Overview and principle models of gamma-ray bursts

On the other end of the size scale compared to neutrinos are events or objects that can be seen over cosmic distances. Light of stars or galaxies can travel for millions of years before it is finally observed. While galaxies host millions of stars or even radiation from supermassive black holes in their center (Active Galaxy Nuclei, AGN) there is a certain class of events that even outshines galaxies for a short period of time. So-called gamma-ray bursts (GRBs) are the brightest events in the currently known universe. They are some cataclysmic event in which (isotropic) energies of the order of the solar mass $M_\odot c^2 (\sim 2 \cdot 10^{54}\text{erg})$ are released in form of a burst which lasts only up to tens of seconds.

The first bursts were discovered in 1967 by satellites flown by the US Department of Defense. The *Vela* satellites had omnidirectional gamma-ray detectors to detect any nuclear explosions which might violate the Nuclear Test Ban Treaty. It could already be established from the first measurements that these short blips of gamma-rays came from space and not from the Earth's direction. Being detected by the military the results were only made public in 1973, see Ref. [43], six years after the first events. Even though detected for years it was at that point not possible to determine the exact origin of the bursts, mostly due to two key problems: First of all

the bursts were too short for extensive measurements and detection happened only by chance. And secondly, gamma-rays are hard to focus with any kind of devise. Sharp "images" of bursts are therefore impossible to take, even now more than 40 years after the first discovery. These uncertainties led to a fast amount of models as astrophysicists have tried to decipher this peculiar phenomenon, see *e.g.* Ref. [44]. It took nearly 25 years from the first detection to the next significant step in the history of GRBs.

An important mission in the process of understanding GRBs was the launch of the *Compton Gamma-Ray Observatory (CGRO)* in 1991. The results of this mission are summarized in Ref. [45]. The main point of these observations was that the distribution of the bursts detected in the all-sky survey of the BATSE instrument were isotropically distributed with nearly no dipole or quadrupole components [46]. This strongly suggested that the bursts originated at cosmological or possibly extended galactic halo distances. If one now considers bursts from cosmological distances, the fluxes of the observed GRBs imply an enormous amount of energy which is released in a very short period of time in a small volume. The latter two conclusions result from the short variability times of the measured bursts. From these conclusions the formation of a relativistically expanding $e^{\pm}$-γ fireball can be derived. The main problem of such a model is the distribution of energy. In basic expanding fireball most energy would be converted into kinetic energy of accelerated baryons, rather than photons, and would lead to a quasi-thermal spectrum. Furthermore, the timescales could not explain events much longer than milliseconds. To address these issues the possibility of shocks being part of the generation of radiation was introduced. The "fireball shock scenario" uses shocks created when fireball ejecta run into the surrounding medium to accelerate particles and create the observed non-thermal radiation spectrum (after the fireball has become optically thin). With the help of Fermi acceleration kinetic energy is re-converted into non-thermal radiation. Moreover, the fast varying structure of the temporal curve can be explained by these models, *e.g.* due to internal shocks with different velocities which collide before running into the external medium. For an introduction to these models see Refs. [47, 48] and references therein.

One of the predictions of the generic fireball shock model is the existence of low energetic afterglows. The detection of these was finally possible after 1997 with the help of the Italian-Dutch satellite Beppo-SAX, which detected fading x-ray images,

see Ref. [49]. After a delay of 4-6 hours from processing these images a position of a burst could be extracted and allowed for follow-up observations in the optical or other wavelength bands, see *e.g.* Ref. [50]. Capitalizing from these multi-wavelength measurements it was possible to obtain the redshift distance of the bursts, identify candidate host galaxies and the confirmation that they were indeed at cosmological distances, see Refs. [51, 52]. After the end of the CGRO and Beppo-SAX missions the HETE-2 satellite followed with accurate measurements of GRB afterglows. The delay between the first detection of a burst and the afterglow measurement by satellite was still some hours. Nonetheless HETE-2 detected the first unambiguous association of a GRB with a SN with the correlation of GRB 030329 to SN2003dh, see Refs. [53, 54].

The third wave of significant advances came from the *Swift* multi-wavelength afterglow satellite, which was launched in November 2004, see *e.g.* Ref. [55] and references therein. This mission finally achieved the goal of measuring the afterglow just minutes after first burst trigger. This yielded important information on the transition of the light curves from prompt emission to the subsequent long term afterglow, measured at gamma-ray, x-ray and optical wavelengths. Moreover, it detected the long-awaited afterglow of short bursts (hard gamma-ray emission is shorter than 2 s). Furthermore, it broke through the symbolic barrier of redshift $z = 6$, even though only very few events at these distances were detected. These measurements helped to refine several parts of the models, especially how the transition from prompt emission to afterglow can be described, and if information can be obtained from high redshifts, $z \geq 6$. And currently the *Fermi* satellite is on the verge of providing an even more detailed range of data. *Fermi* is equipped with two instruments which can measure gamma-rays in different energy ranges. The lower energy range, from $< 10\,\mathrm{keV}$ up to $> 25\,\mathrm{MeV}$, is observed by the GLAST Burst Monitor (GBM), taken from Ref. [56]. The burst monitor can has a full sky field of view (minus the part occulted by the Earth). Therefore, it is used to record pre-trigger information, and can reposition the whole satellite when a burst is detected. The GBM is complimented by the Large Area Telescope (LAT), which can detect events in the range from 20 MeV up to 300 GeV. The field of view of LAT is with 2 sr much smaller than the one of GBM, but, therefore, the angular resolution of LAT is much better ($< 0.5'$ to $\sim 3°$), taken from Ref. [56]. Both instruments together can record the photon flux over roughly seven orders of magnitude with nearly seamless transition between energy ranges, which should bring new insight on GRBs. A first catalog of 438 *Fermi*/GBM bursts has only recently been published, see Ref. [57].

Thanks to observational data it is firmly believed that the following progenitor models, who associate GRB with cataclysmic events at the end of the life of a small fraction ($\sim 10^{-6}$) of stars, are correct. In general two main populations of GRB are distinguished depending on the observed duration of a burst. If the duration is shorter than 2 s then the burst is considered "short" and, correspondingly, if the duration is longer than 2 s then the burst is called "long". For long bursts the candidates are massive ($m \gtrsim 30\,M_\odot$) stars whose core collapses to a black hole, either directly or after a short accretion period with the accretion possibly being the merger with a smaller companion. This so-called collapsar or hypernova model is supported by the detection of an associated supernova through spectroscopic measurements, see Refs. [58, 59]. Another possibility is the formation of a fast-rotating ultra-high magnetic field neutron star from a stellar collapse, a so-called magnetar. For the short bursts currently favored models are mergers of compact objects such as neutron star binaries (NS-NS) or neutron star-black hole (NS-BH) binaries, see Refs. [60, 61]. These loose rotational energy and orbital angular momentum by gravitational waves and then release even more energy during the merger. The scenario for short bursts still needs to be confirmed. Neglecting this missing verification one can conclude that all GRB models end in the formation of a black hole of a few solar masses.

One of the newer additions to the fireball model is the introduction of jet-like outflows (instead of isotropical emission). This consideration is backed by afterglow observations as well as by theoretical aspects. On one hand the observations of x-ray and optical afterglows show a break or steepening which can be interpreted as a sign for the edge of a jet which becomes visible when the jet slows down. For long GRBs the typical jet opening angles are suspected to be $\theta_j = 5^\circ - 20^\circ$. This essentially affects the fireball model since now the emission is no longer from an isotropically expanding fireball but from a jet. However, as long as $\theta_j > 1/\Gamma$ is valid, the fireball model still can be applied, see Eq. (2.26) and the discussion of this equation. Moreover, as a positive effect this results in a reduction of the total amount of energy required for a burst of the observed strength from $10^{53} - 10^{54}$ erg to $\sim 10^{52}$ erg. Instead of an emission from the full surface of a sphere, radiation is only emitted from the surface of the jets. The actual energy amount E_{tot} and the actual luminosity L can be obtained by multiplying the isotropic total energy $E_{\mathrm{tot,\,iso}}$ or, correspondingly, the isotropic luminosity L_{iso} with the fraction of the surface that is actually emitting, *i.e.* the jet surface. However, details depend on the model of

the assumed jet. Until now there is no conclusive jet model and the discussion is going on which kind of model could describe observations. The models range from uniform jets over structured jets to two jet models. We will assume simple case of a uniform jet.

4.2. Parameters of a GRB in the internal shock model

As stated before GRB are considered to be produced from the collapse of stars or the merger of compact objects with the central object being a black hole (or in case of the magnetar model a fast rotating high-mass neutron star which eventually collapses into a BH). During the collapse the release of high amounts of gravitational energy during a short time in a small volume leads to an explosion or expansion. The ejected plasma and photons from the burst interact, eventually producing the so-called prompt emission of a GRB. The photons are assumed to be emitted from co-accelerated electrons in the plasma expanding in form of a jet, the protons are part of the plasma. Depending on the model of choice these relatively general considerations set limits to several parameters of a burst. In this section we want to discuss which parameters of a burst have already been constrained by measurements or theoretical considerations.

We will consider the internal shock model, as proposed in Refs. [62, 63, 64]. In this model the collision of emitted shells leads to the main acceleration, before the ejecta reach the interstellar medium. These collisions are assumed to take place at a distance R_c (in the observer's frame) from the central engine, leading to a delayed acceleration in the GRB, see Fig. 4.1. In case of the internal shock model this distance $R_c^{'}$ is called the collision radius (in the SRF) and can be calculated from observed parameters of a burst as explained in Ref. [30]:

$$R_c^{'} \simeq 2\Gamma^2 c t_v \quad . \tag{4.1}$$

Here Γ is the bulk Lorentz factor, see Eq. (2.2), and t_v is the observed variability time scale. As stated in Ref. [30] both of these quantities can be obtained from the measured light curves including prompt emission as well as the afterglow. Typical values are assumed to be of the order of $R_c^{'} \sim 10^{14} - 10^{15}\,\mathrm{cm}$.

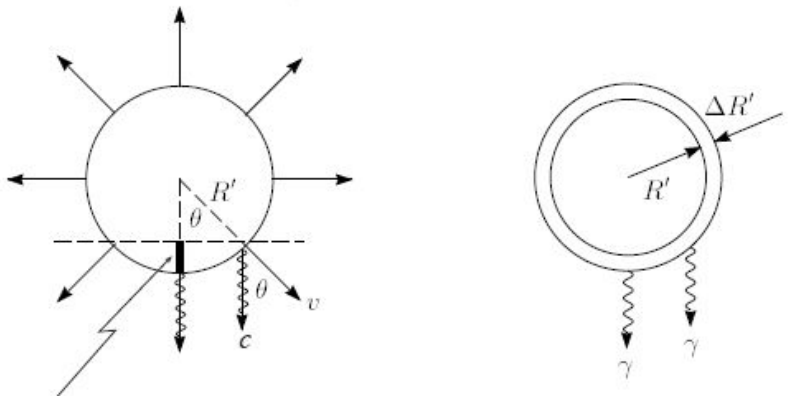

Figure 4.1: These are basic sketches of the emission in the internal shock model and of the shells. They are taken from Ref. [65] to illustrate the basic concept of the internal shock model. The left sketch depicts the emission from different parts of the sphere, leading to the distorted shape in Fig. 2.1. The right sketch shows a shell in the internal shock model. The collision radius $R^{'}$ is our $R^{'}_{C}$ from the text, as well as the shell thickness $\Delta R^{'}$ being our $\delta R^{'}_{C}$.

The variability time t_v describes how fast the temporal structure of the light curve varies. The temporal structure of the GRB light curves is different for every burst, with values of t_v ranging from $\sim 10^{-3}\,\mathrm{s}$ up to 1 s, see Ref. [66]. In the internal shock model it is connected to the shell width and the difference in velocity among shells as well as possibly the distance between these. The width of a shell δR is approximately $10^7\,\mathrm{cm}$, see Fig. 4.1. The variability time is one of the few parameters that can be directly extracted from the measured light curves. However, the result of t_v can vary depending on the energy band. This can either be an effect of the measurement process, or some aspect of the acceleration that has not been understood yet. Moreover, there is so far no clear definition of t_v. Therefore, even the measurement of t_v is subject to high uncertainties.

The other quantity needed in Eq. (4.1) is the bulk Lorentz factor Γ. For a quick explanation of what this quantity describes let us make a comparison to wave descriptions. The bulk Lorentz factor of a burst corresponds to the group velocity is in a wave packet. Accordingly the Lorentz factor of a single shell is equivalent to the phase velocity. For bounds on Γ one can use general considerations on the emission from the jet. As mentioned earlier the fireball has to become optically thin for photons to escape the jet. For the source to be optically thin to non-thermal high energy photons the Lorentz factor has to be at least 100, see Ref. [67]. This approximation is done by calculating the minimal Γ required for the maximal (observed) energy photons to still participate in $e^{\pm}$-pair production inside the source. On the

other hand the Lorentz factor cannot be much higher than 1000 since then the protons would loose most of their energy due to synchrotron radiation, see Ref. [68]. The value of Γ needs to be derived from other observable quantities. In Ref. [30] a method to calculate Γ from observational data is described. In mentioned reference an analysis of a sample of bursts from the *Swift* data is done using two different formulas. The main criteria is the dependence on the observed break energy in photons. From this the minimal needed Γ is constrained, for which the observed radiation is reasonable and not suppressed by some process. It is stated in Ref. [30] that bursts with high observed break energies, $\varepsilon_{\gamma,\mathrm{break}} \gtrsim 500\,\mathrm{keV}$, have a Lorentz factor Γ that does not differ significantly from the minimum value for which the fireball becomes opaque to photons due to pair production near the maximum energy of γ-rays, $\varepsilon_{\gamma,\mathrm{max}}$.[1] Guetta chose 100 MeV as their default maximum photon energy $\varepsilon_{\gamma,\mathrm{max}}$ leading to the formula

$$\Gamma \sim 250 \left[L_{\gamma,52} t_{v,-2}^{-1} \left(\frac{\varepsilon_{\gamma,\mathrm{max}}}{100\,\mathrm{MeV}} \right) \right]^{1/6} \quad . \tag{4.2}$$

This formula describes the extraction of the Lorentz factor Γ out of observational data. As can be seen from the formula it depends weakly on the observed luminosity $L_{\gamma,52}$ (in units of $10^{52}\,\mathrm{erg\,s^{-1}}$) and the observed variability time $t_{v,-2}^{-1}$ (in units of $10^{-2}\,\mathrm{s}$) apart from the aforementioned maximal observed photon energy. On the other hand bursts with low break energy can be analyzed by using some assumptions stemming from synchrotron radiation. In this case the Lorentz factor Γ is related to the peak energy of the γ-ray spectrum, $\varepsilon_{\gamma,\mathrm{break}}$,

$$\Gamma = \epsilon_B^{1/4} \epsilon_e^{3/4} \frac{L_{\gamma,52}^{-1/4}}{\varepsilon_{\gamma,\mathrm{break;MeV}}\, t_{v,-2}^{-1}}\, 10^{2.5} \quad . \tag{4.3}$$

Here, ϵ_B is the fraction of the total energy stored in the magnetic field, and ϵ_e is the fraction carried by the electrons. For details please refer to Ref. [30] and references therein. Using these two formulas Guetta et al. analyzed a sample of *Swift* bursts. The obtained distribution can be found in Fig. 4.2 taken from Ref. [30]. As one can see from the Fig. 4.2 the most observed bursts have a Lorentz factor $\Gamma \sim 300$, a value that is commonly used in the literature, see *e.g.* Refs. [30, 48, 66, 68]. This will later be our reference distribution even though *Fermi* has already produced very interesting new data indicating higher values of Γ. A first catalog with the spectral properties of 438 *Fermi*/GBM bursts has been published recently, see Ref. [57].

[1] Note that in this case $\varepsilon_{\gamma,\mathrm{max}}$ is the real observed maximum photon energy, not the to certain extent arbitrary cut introduced by our model. A discussion of the effect of $\varepsilon_{\gamma,\mathrm{max}}$ can be found in the Appendix A.4.

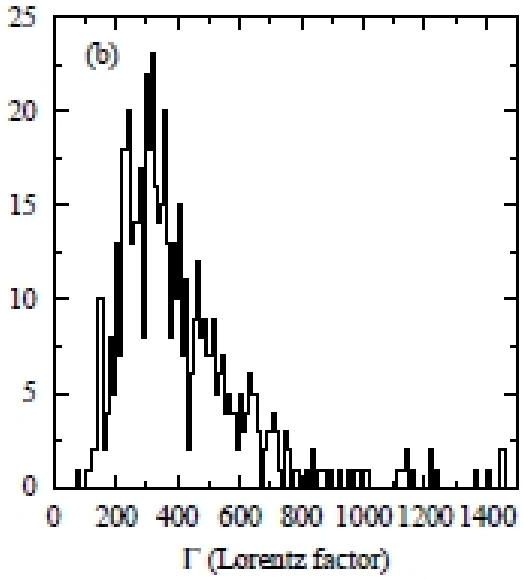

Figure 4.2: This figure shows the distribution of the Lorentz factors Γ obtained by Guetta et al., taken from Ref. [30]. They used the equations, denoted as Eqs. (4.2) and (4.3) in this current work, to calculate the Lorentz factors from the observed light curves. As one can see most of the observed bursts have $\Gamma \sim 300$. The distribution is asymmetric on the displayed linear scale. Namely, the number of bursts with a $\Gamma > 500$ is much smaller than the number of bursts with $\Gamma < 500$. We will try to reproduce this distribution in section 7.1.

However, this comprehensive study only includes properties of the light curves, and none explicitly on the Lorentz factors. Therefore, we have to compare our simulations in section 7.1 with the "old" *Swift* data from Ref. [30].

Since GRB, or more correctly long GRB, are connected to the death of massive stars it is natural to assume that GRB trace the star formation history in redshift z. Since GRB events are only a small fraction of all visible objects it is easier to obtain a distribution of the redshift dependent star formation rate (SFR). There are several models parameterizing the star formation in redshift. A recent work by A. Hopkins and J. Beacom uses a piecewise steady approach to parameterize the star formation rate density, which is denoted as $\dot{\rho}_*$, depending on the redshift z, see Ref. [21]. Note that the dot refers to a differential of cosmic time, which can also be expressed in terms of z, as well as density referring to the z-dependent volume. Therefore, the distribution of $\dot{\rho}_*$ only depends on z, but is given in units of $M_{odot}\,\mathrm{Mpc}^{-3}\,\mathrm{yr}^{-1}$. They obtained the best result from a parameter fit using the initial mass function

proposed by Baldry and Glazebrook, Ref. [69], leading to the following function:

$$\dot{\rho}_* \propto \begin{cases} (1+z)^{3.44} & 0 < z \leq 0.97 \\ 10^{1.09} \cdot (1+z)^{-0.26} & 0.97 < z \leq 4.48 \\ 10^{6.66} \cdot (1+z)^{-7.8} & 4.48 < z \end{cases} \quad . \tag{4.4}$$

As a maximum value for the redshift Hopkins and Beacom introduced a cut-off at $z_{\max} = 6$. As stated in Ref. [21] this is due to the low statistics at even higher redshifts. The universe at higher redshifts is hard to probe, so for now we will only consider the region up to $z = 6$. To get the number of bursts depending on redshift several factors apart from the star formation rate are needed, such as the comoving volume per unit redshift $\frac{\mathrm{d}V/\mathrm{d}z}{1+z}$ or correction factors as in Ref. [70]:

$$\frac{\mathrm{d}\dot{N}}{\mathrm{d}z} = F(z) \, \frac{\mathcal{E}(z) \, \dot{\rho}_*(z)}{\langle f_{\mathrm{beam}} \rangle} \, \frac{\mathrm{d}V/\mathrm{d}z}{1+z} \quad . \tag{4.5}$$

Here $F(z)$ is the fraction of bursts that can be observed at a certain redshift as well as the possibility to obtain a redshift. For simplicity reason we will set this fraction to a constant value, which is feasible if one considers bursts with luminosity L which is high enough to be observed over the whole redshift range, *e.g.* $L - \mathrm{iso} = 10^{52}\,\mathrm{erg\,s^{-1}}$ would be sufficient to be observable up to $z_{\max} = 6$. $\langle f_{\mathrm{beam}} \rangle$ is a correction if a burst is observable or not due to beaming effects. The last factor $\mathcal{E}(z)$ is a correction introduced by Kistler et al. in Ref. [70] to account for the fraction of stars resulting in GRBs. In that work 66 *Swift* GRBs, with well measured redshifts in the range of $z = 0 \to 4$ and $L_{\mathrm{iso}} > 10^{51}\,\mathrm{ergs^{-1}}$, were analyzed and compared to the expected distribution derived from the SRF by Hopkins and Beacom [21]. They conclude that a function $\mathcal{E}(z) = \mathcal{E}_0(1+z)^{1.2}$ describes observational data of GRB best and applies to redshifts higher than the analyzed range as well. This suggests that the death of stars is more likely to result in a GRB at higher redshifts. The "typical value" for the redshift of a GRB according to Ref. [66] is roughly between $z = 1 - 2$. This corresponds to the peak obtained from the star formation rate in Eq. (4.4). With the correction factor these values are shifted to higher redshifts with a broad peak between roughly $z = 2 - 3$. We will discuss the connection between the number of bursts and the star formation rate in more detail in section 7.2.

Another quantity, which is mandatory to consider when talking about shocks and accelerated charges, is the magnetic field. There is still great debate about what values the magnetic field can reach in the relevant acceleration areas. According

to Ref. [71] it is expected to range from 10^4 to 10^7 G for GRBs with no definite restrictions on its value. There is so far no model for the distribution of the magnetic field values, partly due to the lack of a certain method to determine the magnetic field of a GRB. As pointed out by Guetta et al. [30] the magnetic field in the SRF can be calculated by comparing the energy density stored in the magnetic field times the surface of a boosted sphere to the luminosity in the magnetic field. For this derivation several quantities are needed:

$$B^{'} = \sqrt{\frac{\epsilon_B \, L_{iso}}{2\,\Gamma^6\, c^3\, t_v^2}} \quad . \tag{4.6}$$

As can be seen from Eq. (4.6) it has to be noted that the derivation of the magnetic field values strongly depends on the bulk Lorentz factor Γ. The isotropic luminosity can be obtained from the measured flux of a burst, see Eq. (2.20). In Ref. [66] the quoted "typical burst luminosity" L_{iso} is roughly $10^{52}\,\mathrm{erg\,s^{-1}}$, which is the same as our threshold luminosity mentioned in the paragraph on the redshift (in this section). Furthermore, we can again use the values that we previously mentioned in this section, such as $t_v =\sim 10^{-3} - 1\,\mathrm{s}$ and $\Gamma \sim 300$. The last parameter, the fraction of energy stored in the magnetic field ϵ_B, is so far not measurable, and one can only make assumptions for its value. A value of $\epsilon_B = 0.1$ (or similar order) is reasonable but cannot be confirmed by current data. By inserting the quoted typical values from Ref. [66] into Eq. (4.6), one can calculate that the possible values for a typical GRB are between 431 and $4.31 \cdot 10^5$ G.

4.3. The Waxman-Bahcall model of the GRB neutrino spectrum

As mentioned in section 3.1 the calculations by Waxman and Bahcall, taken from Ref. [25], are a simple and solid upper bound for the diffuse flux of neutrinos. In the progress of their calculations Waxman and Bahcall also proposed a flux shape for the muon neutrinos produced in GRBs via photohadronic interactions. This flux shape is the result of relatively general considerations depending on the photon and proton spectra. The observed spectra can be parameterized as following. The steady

target proton field in the rest frame of the source can be written as in Ref. [31]

$$N_p^{'}(E^{'}) = C_p^{'} \cdot \begin{cases} E^{'-2} \cdot \exp\left(-\frac{E^{'2}}{\varepsilon_{p,\max}^{'2}}\right) & \varepsilon_{p,\min}^{'} \leq E^{'} \\ 0 & \text{else} \end{cases} \tag{4.7}$$

with the cut-off energy $\varepsilon_{p,\max}^{'}$ being derived from comparison of acceleration time and synchrotron loss time, see Eq. (4.18) later this section. For computational reasons we include a low energy cut-off $\varepsilon_{p,\min}^{'}$. $C_p^{'}$ is the normalization of the spectrum. The flux shape of the protons is derived from the observed extragalactic component of the cosmic ray spectrum in the energy range between 10^{10} and $10^{12}\,\mathrm{GeV}$, taken from Ref. [72]. The steady target photon field $N_\gamma^{'}(E)$ is derived from observed GRB photon spectra and is parameterized by the Band function[2], see Ref. [73]:

$$N_\gamma^{'}(E^{'}) = C_\gamma^{'} \cdot \begin{cases} E^{'\alpha_\gamma} & \varepsilon_{\gamma,\min}^{'}\,\mathrm{eV} \leq E^{'} < \varepsilon_{\gamma,\mathrm{break}}^{'} \\ \varepsilon_{\gamma,\mathrm{break}}^{'} \cdot E^{'\beta_\gamma} & \varepsilon_{\gamma,\mathrm{break}}^{'} \leq E^{'} < \varepsilon_{\gamma,\max}^{'} \\ 0 & \text{else} \end{cases} . \tag{4.8}$$

Again $C_\gamma^{'}$ is the normalization factor. The spectral indices α_γ and β_γ can be obtained from GRB observations. The median values are $\alpha_\gamma \approx -1$ and $\beta_\gamma \approx -2$. The break energy $\varepsilon_{\gamma,\mathrm{break}}^{'}$ is normally retrieved from the photon spectrum of a burst, but we will need it as a parameter in our model as we will show later on in this section. Moreover, the energy $\varepsilon_{\gamma,\max}^{'}$ is the maximum photon energy, and $\varepsilon_{\gamma,\min}^{'}$ is the lower energy cut-off of the photon spectrum.

From these spectra Waxman and Bahcall concluded a power-law spectrum of muon neutrinos at the observer [25]. The analytic formula normally given (in the language of Ref. [66]) is

$$E_\nu^2 \frac{\mathrm{d}N_\nu}{\mathrm{d}E_\nu} = C_\nu \cdot \begin{cases} (E_\nu/\varepsilon_\nu^b)^{-\alpha_\nu} & \text{for } E_\nu < \varepsilon_\nu^b \\ (E_\nu/\varepsilon_\nu^b)^{-\beta_\nu} & \text{for } \varepsilon_\nu^b \leq E_\nu < \varepsilon_\nu^s \\ (E_\nu/\varepsilon_\nu^b)^{-\beta_\nu}(E_\nu/\varepsilon_\nu^s)^{-2} & \text{for } E_\nu \geq \varepsilon_\nu^s \end{cases} . \tag{4.9}$$

Here $\frac{\mathrm{d}N_\nu}{\mathrm{d}E_\nu}$ (our ϕ_ν) is the observed neutrino spectrum with E_ν being the neutrino energy at the observer. α_ν and β_ν are spectral indices. They are connected to the photon spectrum indices as follows: $\alpha_\nu = \beta_\gamma + 1 \approx -1$ and $\beta_\nu = \alpha_\gamma + 1 \approx 0$ [66].

[2]Note that the original Band function has an additional exponentially decaying component above the photon break. We neglect this feature only for the sake of a better recalculation of the WB flux shape. This is not needed for a calculation to be successful, but purely cosmetic.

This simple shape is often used as the expected neutrino flux shape for a stacking analysis, as in *e.g.* Ref. [74]. In such a stacking analysis the spectra of several bright bursts are used individually to calculate the single source neutrino fluxes. These different fluxes are then added up to obtain a quasi-diffuse limit. These this analysis utilizes the assumption that only a few bright bursts dominate the total flux.

The first break of the WB spectrum ε_ν^b is connected to the break in the photon spectrum $\varepsilon_{\gamma,\mathrm{break}}^{'}$ via the energetics of the Δ-resonance. As can be seen in Eq. (4.9), or in the resulting Fig. 6.1 in section 6.1, the observed first break is set to be at $10^5\,\mathrm{GeV}$ [25, 66]. Following the argumentation of Ref. [30], this first break in the expected neutrino spectrum can be derived from the available center of mass energy of the photohadronic interaction leading to the $\Delta(1232)$-resonance:

$$E_\gamma^{'} E_p^{'} \geq \frac{m_\Delta^2 - m_p^2}{2\,(1-\cos\theta_{p\gamma}^{'})} \quad . \tag{4.10}$$

Here m_Δ and m_p are the rest mass of the Δ-resonance and of a proton, respectively. It has to be noted that this approach slightly differs from the treatment in Ref. [30] since our kinematics treatment takes the collision angle between photon and proton $\theta_{p\gamma}^{'}$ into account. When integrating out the angular dependence, most of the interactions take place at higher center of mass energy. Thus no longer a head on collision ($\theta_{p\gamma}^{'} = \pi$) but an average scattering angle of $\langle\theta_{p\gamma}^{'}\rangle \simeq \pi/2$ corresponds to the peak in the cross-section, see Ref. [29] or the SOPHIA code [75]. By inserting this value of the collision angle into Eq. (4.10) one sees that the cos-term vanishes instead of giving an additional factor of 2 ($= 1 - \cos\pi$). Because of this the needed break energy $\varepsilon_{\gamma,\mathrm{break}}^{'}$ will be larger by a factor of two compared to the result in Ref. [30]. To emphasize the difference in the calculation we will keep the angular dependence in the following formulas, even though it vanishes during calculations in the case of our assumptions. We now need an approximation of how much energy is passed from the parent protons to the neutrinos (after pion decay). It is possible to estimate the fraction of energy f_π passed on from the protons to the pions. In the subsequent decay of the pions about 1/4 of the pion energy is transformed into neutrinos, see Ref. [30]:

$$\begin{aligned} E_\nu^{'} &= \frac{1}{4}\, f_\pi\, E_p^{'} \\ &= \frac{1}{20} \cdot \frac{m_\Delta^2 - m_p^2}{2\,(1-\cos\theta_{p\gamma}^{'})\; E_\gamma^{'}} \quad . \end{aligned} \tag{4.11}$$

Here $f_\pi \approx 0.2$ is used, taken from Ref. [30]. This result then has be boosted to the observer's frame as well as shifted due to cosmologic effects to obtain the observed values, see section 2.3. Note that in Eq. (4.12), the Lorentz factor Γ is used instead of the Doppler factor $\mathcal{D}$ to match conventions in the literature. This is a valid result of Eq. (2.5) when $\theta = 1/\Gamma$ is assumed (in case of large Γ), leading to

$$E_\nu \approx \frac{\Gamma^2}{(1+z)^2} \cdot \frac{1}{20} \cdot \frac{m_\Delta^2 - m_p^2}{2\,(1-\cos\theta_{p\gamma})\,E_\gamma} \quad . \tag{4.12}$$

It was already suggested in Ref. [25] that the charged intermediate particles could loose energy through synchrotron cooling. Following this suggestion it is shown in Ref. [30] that the second break of the WB spectrum ε_ν^s can be obtained by considering synchrotron cooling of the pions. To calculate the energy of this break one has to compare the particle life time $\tau^{'}$ to the synchrotron loss time $t_{\mathrm{syn}}^{'}$. The reasoning for this assumption is that synchrotron losses start to dominate if the synchrotron loss time is shorter than the particle life time, see Ref. [30]. Since Waxman and Bahcall looked specifically into neutrino production resulting from the Δ-resonance, the main charged particles of interest are pions. Nevertheless, the same reasoning applies for other charged particles. The particle specific quantities have to be inserted accordingly in case of *e.g.* muons. The synchrotron loss rate is defined (in SI units) as

$$t_{\pi,\mathrm{syn}}^{'-1}(E_\pi^{'}) = \frac{e^4\ B^{'2}\ E_\pi^{'}}{9\pi\ \varepsilon_0\ m_\pi^4 c^5} \tag{4.13}$$

with ε_0 being the vacuum permittivity (in $\mathrm{A\,s\,V^{-1}\,m^{-1}}$), m_π the rest mass of a pion (in kg), E_π the pion energy (in J), e the elementary charge (in C) and B the magnetic field (in T). It is important for calculations to use the correct units of quantities. Because of this it will be noted in the text if units differ from the normally used units, as in the case of Eq. (4.13). As stated before this needs to be compared to the energy dependent decay rate of the pion $\tau_\pi^{'-1}$ (in SI units):

$$\tau_\pi^{'-1}(E_\pi^{'}) = \tau_{0,\pi}^{-1}\ \frac{m_\pi c^2}{E_\pi^{'}} \quad . \tag{4.14}$$

Here $\tau_{0,\pi}^{-1}$ is the decay rate of the pion at rest. This is tabulated to be $2.6033 \cdot 10^{-8}\,\mathrm{s}$ in Ref. [33]. By assuming equipartion between the synchrotron loss rate and the decay rate, an analytic formula for the energy $\varepsilon_\pi^{'}$ in the shock rest frame is obtained:

$$\varepsilon_\pi^{'} = \sqrt{\frac{9\pi\ \varepsilon_0\ (m_\pi c^2)}{c\ \tau_{0,\pi}^{'}}} \cdot \frac{(m_\pi c^2)^2}{e^2\ B^{'}\ c} \quad . \tag{4.15}$$

Again Eq. (4.15) is in SI units. From this "pion break energy" it is possible to calculate the resulting break in the neutrino spectrum. Such as before, the result needs to be transformed to the observer's frame as well as considering that only about 25% of the pion energy are transfered to the neutrinos. This is done analogous to Eq. (4.12):

$$\varepsilon_{\nu}^{s} = \frac{1}{4} \cdot \frac{\Gamma}{(1+z)} \cdot \sqrt{\frac{9\pi\ \varepsilon_0\ (m_\pi c^2)}{c\ \tau'_{0,\pi}}} \cdot \frac{(m_\pi c^2)^2}{e^2\ B'\ c} \quad . \tag{4.16}$$

The other parameter we can obtain in a similar fashion is the proton cut-off energy $\varepsilon'_{p,\mathrm{max}}$. It can be determined by comparing the energy dependent acceleration rate (Eq. (4.17)) and the synchrotron loss rate (Eq. (4.13)). This method is in principle the same as the one used to calculate the second break of the WB spectrum, but with the acceleration rate (see Ref. [76])

$$t'^{-1}_{\mathrm{acc}} = \eta \frac{c^2\ q\ B'}{E'} \tag{4.17}$$

instead of the particle decay rate. The factor η is the acceleration efficiency, and q the particle charge. Then one can calculate the energy at which the acceleration time is equal to the synchrotron loss time of the protons. This leads to the mentioned maximum proton energy, if we insert proper values for protons:

$$\varepsilon'_{p,\mathrm{max}} = \sqrt{\eta} \cdot \sqrt{\frac{9\pi\ \varepsilon_0\ m_p^4\ c^7}{e^3\ B'}} \quad . \tag{4.18}$$

By inserting the obtained magnetic field B' from Eq. (4.16) and setting a value for η we can calculate $\varepsilon'_{p,\mathrm{max}}$ directly during computation through Eq. (4.18).

5. Numerical Methods

In the next chapter we will explain how the astrophysics and particle physics are implemented in our simulations. We will give a brief overview on our code that we use to simulate photohadronic interactions. In the second part of the chapter we explain the Monte Carlo techniques used to generate the parameter distributions.

5.1. The NeuCosmA code - simulating neutrino production in cosmic accelerators

When calculating neutrino spectra from astrophysical sources there is currently a tradeoff between speed and precision. Either one uses sophisticated Monte Carlo methods such as the SOPHIA software [75] or one uses a rather simple approximation of the interaction cross section with the Δ-resonance approximation, see Eq. (3.2) in section 3.2. Therefore current software is either too slow (SOPHIA) or too inaccurate (Δ-resonance approximation) for detailed parameter studies. Because of these limitations we use our C-software NeuCosmA ("Neutrinos from Cosmic Accelerators") for the calculation of the neutrino spectra.

NeuCosmA is specifically designed to model neutrinos from cosmic accelerators. The current version developed by our group and collaborators can very efficiently calculate photohadronic interactions and subsequent particle decays. This is possible by analytically approximating the photohadronic interaction treatment of the SOPHIA code with a parametric description as proposed in Ref. [77]. This comes at the expense of a simpler kinematics treatment compared to SOPHIA, however, as it is shown in Ref. [29] this treatment reproduces the SOPHIA result with high accuracy. The code can simulate the production of π^+, π^- and π^0 as well as K^+ and n separately and can easily be extended with further particles, *e.g.* K^0. All of these production processes include the Δ-resonance, higher resonances, direct (t-channel) production and at high energies statistical multi-pion production. The code can

calculate the decay of the secondary particles into neutrinos without integrating out the intermediate particles. This is necessary to include the effect of energy losses of intermediate particles before they further decay. To correctly calculate these energy loss effects particle properties such as charge and mass are already included for each particle. For each step spectra are generated with the help of interpolating functions to reduce numerical errors. This form of generality allows for the application of the code for arbitrary photon and proton (target) spectra.

Our simulations use model Sim-B from Ref. [29] which includes direct production (t-channel), different resonances, and high energy processes. Also muon decays are treated helicity dependent as in Ref. [31]. The resulting neutrino spectra have to be Lorentz boosted (and redshifted) to obtain the spectra at the Earth. We assume that the source is optically thin to neutrons, which means that neutrons produced by the photohadronic interactions will decay via beta decay and lead to an additional electron antineutrino flux. For all charged particles we include the effect of adiabatic and synchrotron energy losses, and we assume that these dominate such that energy losses due to inverse Compton processes, Bethe-Heitler pair production, and photohadronic interactions (the source is optically thin to neutrons) are subleading. Although not all spectral features of some sources may be described by this method, it has the advantage that the electron-positron (or proton) ratio is not needed as parameter, and that only the product of photon and proton injection spectrum enters the total normalization.

To summarize, we show in Fig. 5.1 a flowchart describing the computation of the neutrino spectra in the shock rest frame (SRF). As introduced in section 2.3 $Q(E)$ (rectangular boxes) stands for (injection) spectra per time frame and $N(E)$ (boxes with rounded corners) for steady spectra derived from the balance between injection and losses or escape. Dashed arrows stand for solving the steady state differential equation balancing energy losses and escape with injection. Weak decays and photohadronic interactions are denoted by the horizontal lines. The resulting neutrino spectra are marked by a double border and a colored background. Below the boxes we indicate in which decay the neutrinos are produced.

For the charged species we consider possible energy losses, such as synchrotron radiation, before they decay. The kinetic equation for the particle spectrum, assuming

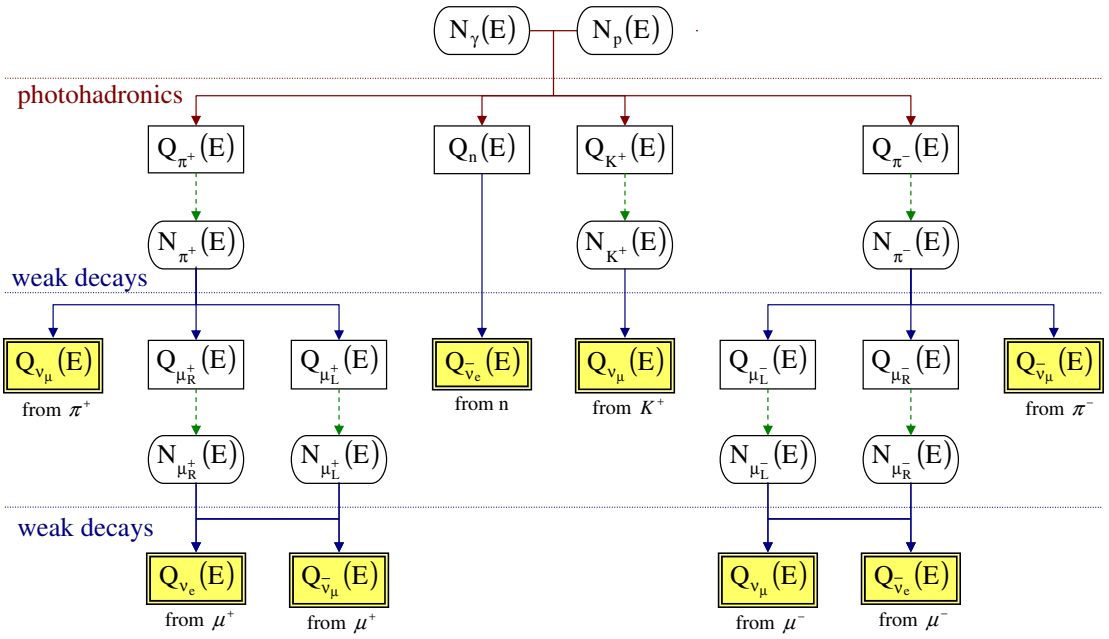

Figure 5.1: Flowchart describing the model. The functions $Q(E)$ denote the time dependent (injection) spectra $[(\mathrm{GeV\,s\,cm^3})^{-1}]$ and $N(E)$ the time independent ones $[(\mathrm{GeV\,cm^3})^{-1}]$. Dashed arrows stand for solving the steady state differential equation Eq. (5.2). The decay of kaons is depicted without the resulting muons, see Eq. (3.5). It is analogous to decay of π^+.

continuous energy losses, is given by (see, *e.g.*, Ref. [78]):

$$\frac{\partial N(E)}{\partial t} = \frac{\partial}{\partial E}\left(-b(E)\,N(E)\right) - \frac{N(E)}{t_{\mathrm{esc}}} + Q(E) \tag{5.1}$$

with $t_{\mathrm{esc}}(E)$ the characteristic escape time, $b(E) = -E\,t_{\mathrm{loss}}^{-1}$ with $t_{\mathrm{loss}}^{-1}(E)$ the rate characterizing energy losses, $Q(E)$ the particle injection rate $[(\mathrm{GeV\,s\,cm^3})^{-1}]$ and $N(E)$ the time independent particle spectrum $[(\mathrm{GeV\,cm^3})^{-1}]$. For different energy loss or decay mechanisms, the inverse timescales are summed over. Because the statistics in neutrino observations is not expected to be as high as that time dependent features can be reasonably resolved, we assume that energy losses and escape are in balance with the particle injection and that $\partial N(E)/\partial t = 0$, which leads to the so-called steady state spectrum $N(E)$ described by the differential equation

$$Q(E) = \frac{\partial}{\partial E}\left(b(E)\,N(E)\right) + \frac{N(E)}{t_{\mathrm{esc}}} \quad . \tag{5.2}$$

Our computations will only consider the energy range from $1(=10^0)$ to $10^{10}\,\mathrm{GeV}$.

5.2. Monte Carlo simulation of diffuse fluxes

In our simulations we also want to take into account that each GRB is different. Even though there are certain "typical" values, the parameters, such as the Lorentz factor Γ, the redshift z, or the magnetic field B, vary significantly from burst to burst. Therefore, we need to simulate a certain number of bursts to understand how the (measured) distribution of a parameter affects the spectrum of a single burst, and the diffuse flux. This simulation of several bursts with different parameters can be done by randomly picking values for the distributed quantities. Simulations utilizing random numbers as an integral part of their calculations are called Monte Carlo simulations.

Monte Carlo simulations are a junction between the mathematical description of an event and its measured results. The mathematical description of an event is generally continuous, the results, however, are divided in "steps" due to the finite resolution of measurements. The law of large numbers tells us that only for an infinite number of events measured with infinite resolution the result is identical to the continuous mathematical description. However, real measurements are always done for a finite number of events and with a certain resolution, leading to deviations from the expected empirical result. Here, computers have opened the possibility to simulate a finite number of randomly distributed events, which can be compared to experimental results. Monte Carlo simulations use the laws of statistics to randomly pick values according to the continuous description. The correct input in form of the mathematical description is essential for the simulation to return useful results. Thanks to advances in the hardware sector in the last two decades, it is now possible to run (smaller) simulations on desktop PCs. The current standard of multi-core CPUs as well as programmable GPUs allow for efficient computation on low budget hardware with the possibility of parallelizing the programs.

The simulation of the diffuse flux has already been done with the help of Monte Carlo simulations, see *e.g.* Ref. [71]. However, in previous studies the calculation was done with help of Monte Carlo integration. Hence, the calculation of the flux was done with integrals, which were solved numerically. But, the result of an integration over the continuous distribution represents the limit of an infinite number of sources. This is, however, not the realistic case for a measurement. The result of the integration does not represent the measured result of only a few events. There-

fore, the use of Monte Carlo integration is highly limited for the diffuse flux. Low statistics samples, or stacking analyses for a quasi-diffuse flux cannot be done by it. Thus, we will use another technique called Monte Carlo sampling. This technique utilizes to the original intention to pick a certain number of bursts with distributed parameters. Here, the values for the parameters are generated for each burst separately and each burst is calculated individually. In chapter 7 we will first calculate the (quasi-)diffuse flux for a high number of bursts. Then, we will show in chapter 8 that we can calculate even low statistics samples with Monte Carlo sampling. For our simulations we generate sets of variables with (known) complicated probability density functions. Therefore, it is necessary to first generate uniform statistically independent values on the half open interval $[0, 1)$ with a "random number generator". There are several different algorithms available in software libraries which differ in quality and speed. We use the random number generator and functions provided by the GSL utilizing the standard gsl_rng_mt19937 generator. This is the "Mersenne Twister" generator by Makoto Matsumoto and Takuji Nishimura, Ref. [79], using "the second revision of the seeding procedure published by the two authors above in 2002" as stated in the GSL manual, Ref. [GSL Manual]. The seed is left unchanged at zero, if not stated otherwise.

To generate parameter sets for variables with measured distributions we need to transform a uniform distribution of random numbers into an arbitrary one. For this purpose we will use the inverse transform method. The general approach is that if a probability density function is $f(x)$ on $-\infty < x < \infty$, it is possible to define a cumulative distribution function

$$F(a) = \int_{-\infty}^{a} f(x)\,\mathrm{d}x \tag{5.3}$$

describing the probability that $x \leq a$. If we assume that $f(x)$ is normalized then $F(a) \in [0, 1]$. For a real probability density function this addition is not necessary since normalization is implicitly assumed. In our case where we want to apply this concept to measured distributions it is essential that all distributions have to be normalized. Also measured distributions introduce cuts so that the endpoints are no longer $\pm\infty$ but $x_{\min}$ and $x_{\max}$. In that case the normalization is performed over the interval $[x_{\min}, x_{\max}]$. We can now assume that $F(x)$ is a uniformly distributed random variable u we can find a connection between u and x:

$$x = F^{-1}(u) \quad . \tag{5.4}$$

This relation is true as long as there is a unique inverse of $F(x)$. This inverse allows us to generate parameters x with a probability density $f(x)$ from a uniform distribution u. In some cases no analytic inverse function can be found. In those cases a numerical inversion has to be done.

In some cases we have to use distributions with complicated dependencies in order to correctly simulate these parameters. In these cases it is essential to ensure that the probabilities are conserved. If we have to random variables x and y with $y = y(x)$ then the probability distribution function $P(y)$ depends on x in this case since $P\,(y(x))$. The distribution $P(x)$ can be deformed to be unrecognizable, but probabilities always have to be conserved:

$$\begin{aligned} P(y)\,\mathrm{d}y &= P(x)\,\mathrm{d}x\,, \\ P(y) &= P(x)\,\frac{\mathrm{d}x}{\mathrm{d}y}\,. \end{aligned} \tag{5.5}$$

In chapters 7 and 8 we will use these methods to generate parameter sets for different quantities, such as the bulk Lorentz factor of a burst, see section 7.1, the distance to the observer in form of the redshift, see section 7.2, as well as the magnetic field in the emission region of a burst, see section 7.3.

6. The simulation of a single burst Waxman-Bahcall GRB neutrino spectrum

In this chapter we discuss the spectrum of a single burst. We first reproduce the commonly used flux shape for GRB neutrinos proposed by Waxman and Bahcall. Then, we show how this shape changes, if additional production channels of the photohadronic cross section are included. In the last step we include the effect of flavor mixing, which further alters the flux shape.

6.1. The numerical reproduction of the original Waxman-Bahcall flux shape

The estimates of Waxman and Bahcall are currently seen as an approximation of the neutrino flux stemming from the prompt emission of GRBs on the basis of cosmic ray observations. In the simple Δ-resonance approximation used for the derivation of the flux shape only ν_μ from π^+ decay are considered, see Eqs. (3.2) and (3.3). The analytic version of the WB flux spectrum, see Eq. (4.9), is plotted in Fig. 6.1 as neutrino flux $E^2 \cdot \phi_\nu(E)$ as a function of energy E. The spectral indices of the analytic version have been set to $\alpha_\nu = -1$ and $\beta_\nu = 0$. The two break energies ε_ν^b and ε_ν^s are obtained from limiting calculations, as described in section 4.3. They are a result of the photohadronic interactions (ε_ν^b) or stem from synchrotron effects (ε_ν^s). In the literature these breaks are $\varepsilon_\nu^b \approx 10^5\,\mathrm{GeV}$ and $\varepsilon_\nu^s \approx 10^7\,\mathrm{GeV}$, Ref. [66]. In Fig. 6.1 we plot the analytical version of the Waxman-Bahcall spectrum (thin, dashed curve) and compare this with the numerical reproduction of the spectrum (bold, solid curve). We will now discuss how we can calculate the WB shape numerically.

We first need to calculate a parameter set that reproduces the WB flux shape. This is done with the equations in section 4.3. The bulk Lorentz factor is set to be $\Gamma = 10^{2.5} (\approx 300)$ since the analysis in Ref. [30] illustrated that most bursts have

such a value of Γ. As stated in section 4.2 the redshift, at which the most bursts are observed, depends on the star formation rate and further parameters. The values for this z differ in the literature. According to Ref. [24] the "typical redshift" would be $z \approx 1-2$, while Ref. [80] claims that $z = 3$ is more likely to be the most "productive" redshift. For our derivations we will assume the latter value, and use the according set of parameters as reference. Nevertheless, it is also possible to derive a parameter set with $z = 2$ which leads to the same result, see Table 6.1. By fixing the lower break to $\varepsilon_\nu^b = 10^5\,\mathrm{GeV}$ we can use Eq. (4.12) to calculate the break energy of the photon spectrum $\varepsilon_{\gamma,\mathrm{break}}^{'}$. Using the previously defined values we obtain $\varepsilon_{\gamma,\mathrm{break}}^{'} = 11.06\,\mathrm{keV}$ for our model, which would translate to an observed break at $\varepsilon_{\gamma,\mathrm{break}} = 874.37\,\mathrm{keV}$. From the considerations for the second break, see Eq. (4.16), we can calculate the magnetic field $B^{'}$ needed to get an expected break $\varepsilon_\nu^s = 10^7\,\mathrm{GeV}$. Keep in mind that we need a certain precision on our calculated values, which my be not justifiable from an experimental point of view, to reduce numerical errors during simulation. Therefore, the values given reflect the numbers we actually use for our simulations. We obtain $B^{'} \simeq 2.16 \cdot 10^5\,\mathrm{G}$, which is of the same order as the $1.5 \cdot 10^5\,\mathrm{G}$ obtained Razzaque et al. in Ref. [81]. However, the authors in Ref. [81] obtained their result from considerations on synchrotron radiation by protons for a particular burst, *i.e.* GRB 080916C, the most powerful burst measured so far [82]. All values are summarized in Table 6.1. With this first parameter set and using a Δ-resonance setting described in Ref. [25] we calculate the expected neutrino spectrum. The result, a comparison of the analytic and the numeric spectrum, can be found in Fig. 6.1. As one can see from the plot in Fig. 6.1 our numerical result matches the analytic function well, even though the second break is obscured by a small hump in front of it. This "hump" is the result of the synchrotron losses. While these lead to lower amounts of particles above the break the same mechanism gives rise to a pile-up effect just below the break. This feature can be seen for every particle species which is affected by synchrotron losses. This will be more important in the next section when we introduce further particles and decay channels.

Since our value for $\varepsilon_{\gamma,\mathrm{break}}$ is not the average value for the observed spectral break of a GRB photon spectrum we also calculate a version with the same parameter set obtained in the previous paragraph, but with different $\varepsilon_{\gamma,\mathrm{break}}$. For comparison we also add the resulting spectrum for an observed spectral break $\varepsilon_{\gamma,\mathrm{break}} = 300\,\mathrm{keV}$, which corresponds to $\varepsilon_{\gamma,\mathrm{break}}^{'} = 3.79\,\mathrm{keV}$ in the source rest frame, to Fig. 6.1. It is depicted as a bold, dashed line. As expected the first break in the neutrino spec-

Γ	$B^{'}$	z	$\varepsilon^{'}_{\gamma,\mathrm{break}}$	$\varepsilon^{'}_{p,\mathrm{max}}$	η	$E^{'}_{p,\mathrm{min}}$	$E^{'}_{\gamma,\mathrm{min}}$	$\varepsilon^{'}_{\gamma,\mathrm{max}}$
$10^{2.5}$	$2.16 \cdot 10^5\,\mathrm{G}$	3	$11.06\,\mathrm{keV}$	$1.37 \cdot 10^8\,\mathrm{GeV}$	0.1	$1\,\mathrm{GeV}$	$0.2\,\mathrm{eV}$	$300 \cdot \varepsilon^{'}_{\gamma,\mathrm{break}}$
$10^{2.5}$	$2.89 \cdot 10^5\,\mathrm{G}$	2	$14.76\,\mathrm{keV}$	$1.18 \cdot 10^8\,\mathrm{GeV}$	0.1	$1\,\mathrm{GeV}$	$0.2\,\mathrm{eV}$	$300 \cdot \varepsilon^{'}_{\gamma,\mathrm{break}}$

Table 6.1: Two sets of parameters capable of reproducing the WB flux spectrum from first principles. The first line the set of parameters we used in our line of reasoning. The second line represents the parameters we would need in our model, if we assumed that the redshift z was 2 instead of 3. Since all parameters are connected in one way or another a change in one parameter can still lead to lead to the same result if the other parameters are adjusted accordingly.

trum is now at higher energies, the other features including the second break stay the same. However, newest data from *Fermi*/GBM suggests that it is more realistic to assume $\varepsilon_{\gamma,\mathrm{break}} \simeq 160\,\mathrm{keV}$ as the average spectral break, taken from Ref. [57]. Therefore, the first break of real neutrino spectra is to be expected at higher energies than WB assume. However, we will for now focus on the reproduction of the original shape with the fixed expected breaks in the muon neutrino spectrum.

The normalization is taken from considerations by Waxman and Bahcall, Ref. [25], in an attempt to set an upper limit to the possible flux of neutrinos derived from proton flux measurements. It estimates the spectral bound by assuming that all energy in protons is lost via pions. From this reasoning it is obvious that actual results will be below this bound. Even though some of our later spectra exceed this bound it is only because we want to emphasize the effects our additions have on the spectral shape and the relative flux levels. We take the integrated energy amount $\hat{E}$ in ν_μ as the reference for the normalization of the spectra:

$$\hat{E} = \int E\,\phi_\nu(E)\,\mathrm{d}E \quad . \tag{6.1}$$

This allows us to incorporate energy conservation even if the spectral shape is slightly different from the analytical form. For this reason it was essential that we added a version of the Δ-resonance treatment to our software which incorporates the assumptions used by Waxman and Bahcall in Ref. [25]. The integrated energy in (only) muon neutrinos produced when using the aforementioned cross section was compared with the integrated energy in the analytical spectrum. The plateau of the analytical spectrum was set to the bound derived by WB. The value for the bound is taken from the update in Ref. [72] and is $E^2\,\phi^{\mathrm{WB}}_{\bar{\nu}_\mu+\nu_\mu}(E) \approx 0.9 \cdot 10^{-8}\,\mathrm{GeV\,cm^{-2}\,s^{-1}\,sr^{-1}}$ for the total muon neutrino $(\bar{\nu}_\mu + \nu_\mu)$ flux. We can also assume a flux of ν_e from the consideration that the source produces $\nu_e : \nu_\mu : \nu_\tau$ in a ratio of $(1 : 2 : 0)$

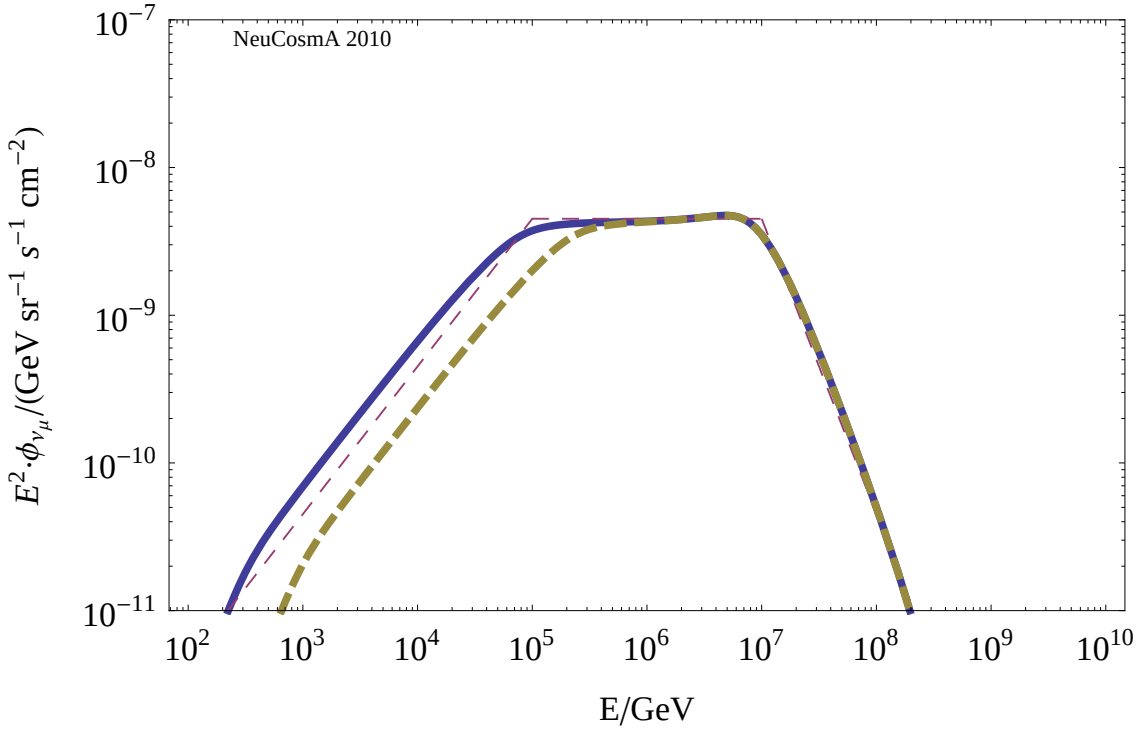

Figure 6.1: Comparison of the computed (thick curve) to the ideal (dashed curve) WB spectrum (of ν_μ). The idealized Waxman-Bahcall spectrum for ν_μ is as described in Eq. (4.9). The breaks are set to be at $\varepsilon_\nu^b = 10^5$ GeV and $\varepsilon_\nu^s = 10^7$ GeV. From these breaks we calculated the parameters needed to obtain the computed version of the spectrum. The used parameters can be found in Table 6.1. Additionally we computed the spectrum expected for $\varepsilon_{\gamma,\mathrm{break}} = 300\,\mathrm{keV}$ which corresponds to the average observed break in photon spectra (thick, dashed curve).

due to pion and subsequent muon decay. This leads to the flux of $E^2\,\phi_{\nu_e}^{\mathrm{WB}}(E) \approx 0.45 \cdot 10^{-8}\,\mathrm{GeV\,cm^{-2}\,s^{-1}\,sr^{-1}}$ for every species of neutrino - ν_e, ν_μ or $\bar{\nu}_\mu$ - in this basic WB model. This result is obtained in the following manner, as described in Ref. [25] and [72]. Starting from the measurement of the proton flux at Earth, the flux is analyzed using a two component model, *i.e.* a galactic and an extragalactic component. For GRBs, the extragalactic component is considered the relevant part of the flux spectrum. The level of this extragalactic proton flux can be derived by assuming the production rate of protons in the energy range of $10^{19}\,\mathrm{eV}$ to $10^{21}\,\mathrm{eV}$ to be

$$\dot{E}^{\mathrm{CR}} \approx 3 \cdot 10^{44}\,\mathrm{erg\,Mpc^{-3}\,yr^{-1}} \tag{6.2}$$

if coming from cosmologically-distributed sources with a power law differential energy spectrum $\mathrm{d}N_p/\mathrm{d}E_p \propto E^{-2}$. This corresponds to an energy per logarithmic

decade of protons of

$$E_p^2 \frac{\mathrm{d}\dot{N}_p^{CR}}{\mathrm{d}E_p} \approx 0.7 \cdot 10^{44}\,\mathrm{erg\,Mpc^{-3}\,yr^{-1}} \quad . \tag{6.3}$$

This energy generation rate sets an upper limit to the production of neutrinos in extragalactic sources which are optically thin to pion producing photohadronic interactions of protons with source photons, *e.g.* GRBs or jets of AGNs. If one now assumes that the high-energy protons loose a fraction $\epsilon < 1$ in photohadronic interactions creating pions before leaving the source, the resulting present-day energy density of muon neutrinos is $E_\nu^2 \mathrm{d}N_\nu/\mathrm{d}E_\nu \approx 0.25 \epsilon t_H E_p^2 \mathrm{d}\dot{N}_p^{CR}/\mathrm{d}E_p$. Here t_H is the Hubble time which is taken to be $\approx 10^{10}$yr as in Ref. [72]. It is now considered that for energy independent ϵ the neutrino spectrum follows the proton spectrum since the amount of energy carried away in form of neutrinos through a photo-meson interaction, $E_\nu \approx 0.05 E_p$, is energy independent. This fraction, 0.05, consists of the fraction of proton energy converted to pions, $f_\pi \approx 0.2$, and the fraction of pion energy resulting in neutrinos, $f_{\pi\to\nu} \approx 0.25$. Ref. [72] states that the factor of 0.25 arises because only half of the produced pions are charged and again about half of the charged pion energy is carried away by neutrinos in weak decays.[1] Waxman and Bahcall also consider that the fraction of proton energy converted pions f_π is not necessarily fixed. However, for the calculation of the bound we will use $f_\pi = 0.2$, independent of energy, as suggested in Refs. [72, 30]. A more detailed, and energy dependent, treatment of this fraction is implicitly included in our NeuCosmA code. With this reasoning a value depending on ϵ can be determined,

$$\begin{aligned} E_\nu^2 \phi_\nu &\leq E_\nu^2 \phi_\nu^{\mathrm{WB}} \approx f_\pi\, f_{\pi\to\nu}\, \epsilon\, \xi_Z\, t_H\, \frac{c}{4\pi}\, E_p^2 \frac{\mathrm{d}\dot{N}_p^{CR}}{\mathrm{d}E_p} \\ &\approx 1.5 \cdot 10^{-8}\, \epsilon\, \xi_Z\, \mathrm{GeV\,cm^{-2}\,s^{-1}\,sr^{-1}} \quad . \end{aligned} \tag{6.4}$$

The derivation of this bound neglects the redshift energy loss of neutrinos produced at cosmic time $t < t_H$ and implicitly assumes that the cosmic-ray generation rate per unit (comoving) volume is independent of cosmic time. The quantity ξ_Z has been introduced to describe corrections due to redshift evolution and energy loss. For details see Ref. [83]. In the derivation of the limit for GRBs ξ_Z will be set to $\xi_Z \approx 0.6 < 1$, which reflects the assumption that the energy generation rate does not evolve with redshift, and neutrinos are subject to redshift energy loss (with a

[1] These assumptions differ from our photohadronic treatment, but this should not be a hindrance to still use the WB bound since it is an upper bound which can be considered largely independent of the details of the theory. There is definitely potential for refinement but this shall not be considered in this work.

weak dependence on cosmology). This represents a more conservative bound than models including evolution with redshift. If we now assume that GRBs carry similar amounts of energy in high-energy protons and electrons and, therefore, account for the observed ultra high energy cosmic-ray flux, one can use Eq. (6.4) to obtain the expected GRB muon-neutrino flux. This flux still depends on the fraction of energy ϵ lost by the protons in form of pions. In the plots throughout the paper we will set $\epsilon = 1$ and will remember that this is an upper limit with the real limit being lower:

$$E_\nu^2 \phi_\nu 0.9 \cdot 10^{-8}\ \epsilon\ \mathrm{GeV\,cm^{-2}\,s^{-1}\,sr^{-1}}\,. \tag{6.5}$$

6.2. Particle production modes beyond the $\triangle$-resonance

We start our re-examination with the change of the cross section of photohadronic interactions. In Fig. 6.2 we show how the flux of ν_μ from π^+ increases when, starting from the $\Delta(1232)$-resonance. We successively add the higher resonances which contribute to the total photohadronic cross section in the observed energy range, direct (t-channel) interactions and high energy processes ("Multi-π"). Especially the multi-pion production enhances the flux in regions above 10^4 GeV and leads to a tilt of the plateau. Furthermore, it leads to a contribution of neutrinos from π^- decay. Because of these π^- we plot the flux of ν_μ and $\bar{\nu}_\mu$ together. As one can see from Fig. 6.2 the result for the full cross-section is up to one order of magnitude higher than the result for $\Delta(1232)$. Since the Δ-resonance approximation by Waxman and Bahcall includes more than just $\Delta(1232)$ the change compared to the WB approach (thick dashed line; "WB Δ^+-approximation") is only of the order of ≈ 3. If one compares the WB result in Fig. 6.2 to the different contributions one can tell that the WB Δ^+-approximation already includes the $\Delta(1232)$ resonance, higher resonance and probably contributions from direct interactions at energies below 10^6 GeV.

As mentioned in section 3.2 the Δ-resonance contributes more neutrinos than just ν_μ. To be more precise the energy independent (and therefore simplified) decay of π^+, Eq. (3.3), results in a flavor ratio ($\nu_e : \nu_\mu : \nu_\tau$) of (1:2:0) after production. As shown in Ref. [20] this is not true and can be easily verified by comparing the break energies from synchrotron cooling of pions and muons. While Eq. (4.16) is for ν from π decays simply changing the particle dependent quantities of the equation, such as the lifetime τ_0 and the mass m, to the values of muons one can calculate the break for muons. This is, as already stated in Ref. [25], roughly one order magnitude

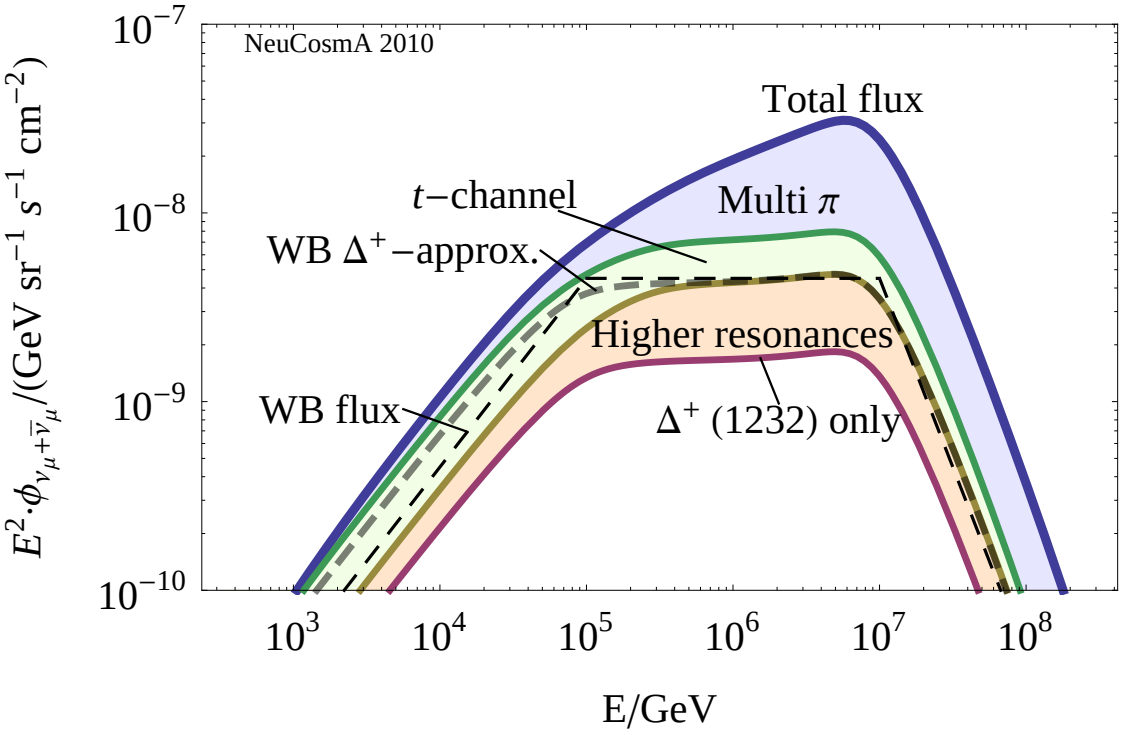

Figure 6.2: The change of the WB-like spectrum depending on the contributions to the cross section. We start with the Δ(1232)-resonance and then add sequentially higher resonances, direct (t-channel) interactions and high energy processes ("Multi-π") to obtain the full result for ν_μ from π^+ (Total flux). The curves are labeled accordingly. As one can see the so-called Δ-resonance approximation of Waxman and Bahcall (dashed thick line, see label "WB Δ^+-approximation") which we used in the previous section already includes the higher resonances as well as a contribution from the direct interactions at energies below 10^6 GeV. The plot also includes the analytic version of the WB spectrum as in Eq. (4.9) (thin dashed black line).

lower than the pion break. If we now include the contributions from further particles as stated in Eqs. (3.3) to (3.6) there are several changes. There are more channels which produce neutrinos and alter the shape of the spectrum. The high energy (multi π) processes lead to contributions from negative pions and muons, leading to more anti-neutrinos in comparison to the Δ-resonance. Apart from the inverted ratio of ν to $\bar{\nu}$ the different sign of charge has no effect on properties such as the cooling break. Because of this we will not distinguish between the charge signs in the following discussion. (The exception are kaons which will only contribute as K^+ and will be considered solely with positive charge. Contributions from K^- or K^0 are neglected.)

As one can easily see from Fig. 6.3 the dominating contribution depends on energy. The different particle species are produced with the "full" cross section of the

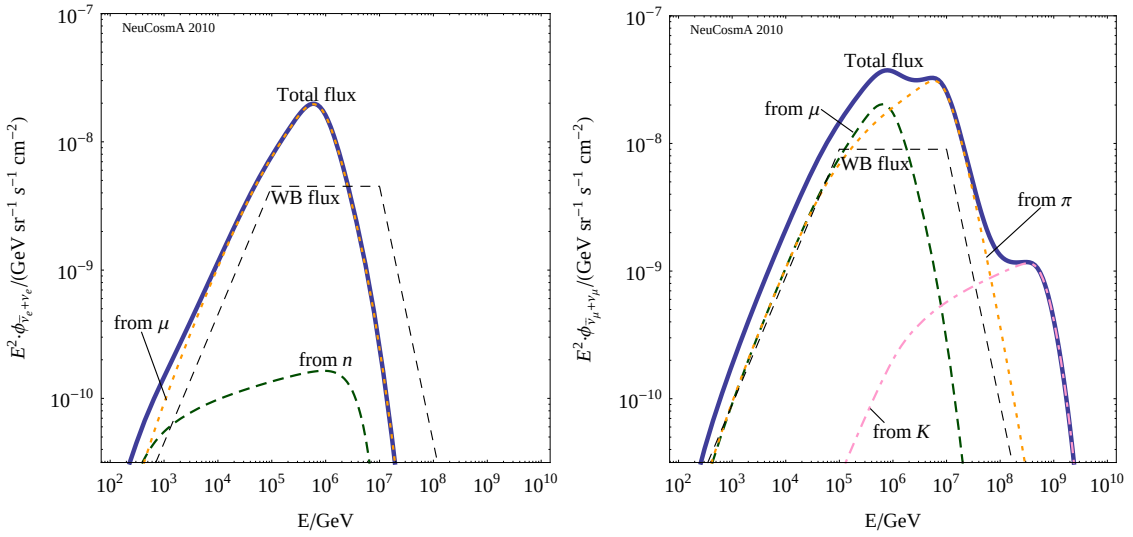

Figure 6.3: In the above graphs the contributions of different particles to the total neutrino flux of a flavor is depicted. On the left is the flux of ν_e with the contributions from n- (dashed) and μ-decays (dotted). The right hand side shows the spectrum of ν_μ with the contributions of muons (dashed), pions (dotted) and kaons (dot-dashed). The shaded area is both graphs the contribution calculated from the Δ-resonance only.

interaction model leading to in general higher values than the WB-bound. Especially, the additional breaks from muon decay at $5.43 \cdot 10^5$ GeV and kaon decay at $3.39 \cdot 10^8$ GeV can be seen in the ν_μ channel, as shown in the right graph of Fig. 6.3. The different contributions from different parent particles alter the shape of WB spectrum significantly. Pile-up effects lead to an excess of the parent particles (and subsequently of the neutrinos) in the region below the breaks while synchrotron losses lead to a steepening in energy by two powers of energy as assumed for the theoretical curve in Eq. (4.9). Instead of a plateau-like shape now we have a peak at the muon break, a peak at the pion break (still at 10^7 GeV) and a third peak coming from the kaon decays if we plot the combined flux of ν_μ and $\bar{\nu}_\mu$ as in right graph of Fig. 6.3. In the case of the ν_e the main change in the combined flux is that now $\bar{\nu}_e$ can contribute. Not only μ^- decays are a factor but also the neutrinos from neutron decays. For our chosen set of parameters the contributions from neutrons dominate at energies below 10^3 GeV, but could also dominate at high energies since neutrons are not affected by magnetic fields. In our case the neutrinos from neutrons extend only $10^{6.5}$ GeV due to the exponential cut-off in the proton spectrum.

6.3. Effects of flavor mixing on GRB neutrino spectra

In the last step we include neutrino mixing due to transitions among mass eigenstates contributing to a flavor eigenstate. As stated in section 3.3 we can assume averaged oscillation probabilities to describe flavor mixing in the case of cosmic neutrinos. The reasoning justifying this assumption is the following: According to quantum mechanics, we can assume that neutrinos are produced as finite wave packets. The different wave modes represent the mass eigenstates. Therefore, the existence of neutrino oscillations dictates that the initial wave packet needs to be a coherent superposition of the mass eigenstates. As for all coherent wave packets, there is a finite decoherence length after which there are no more transitions among mass eigenstates. For cosmic sources, the distance between the source and the observer on Earth is so huge that it can be assumed much larger than the decoherence length of the neutrinos. Hence, we can use averaged transition probabilities for flavor mixing. As we are only considering three neutrino mass eigenstates, the probability of a neutrino of flavor α being detected as a neutrino of flavor β is given by Eq. (3.10). If we apply Eq. (3.11) to the spectra from the previous section, then the observed values of ν_e and ν_μ are a mixture of the produced values. The resulting spectra can be seen in Fig. 6.4 where we have plotted the reference WB flux after mixing (thin, dashed line) and the total expected flux of neutrinos as a bold, solid line. The shaded area surrounding this line is the still possible range of the flux due to uncertainties on the mixing parameters. Furthermore, the contributions from ν_e (dark, dashed line) and ν_μ (light, dotted line) to the respective total (mixed) spectrum are included to better understand the resulting spectral shape. In case of the ν_μ we also added a rescaled version of the total flux to include "energy conservation" compared to the WB flux using Eq. (6.1). This was done to emphasize the deviations in the spectral shape due to the additional effects.

Due to the mixing both spectra now have features from both channels. The differences are more subtle than before mixing. Features such as the higher peak near the muon break in case of ν_e are possibilities to distinguish the spectra directly. Another possibility is taking flavor ratios into account since shower and track events are produced by different flavors. The commonly used ratio R is the ratio of track to shower events which can be associated to the flux ϕ of muon neutrinos (tracks) and electron and tau neutrinos (showers) at the detector, see Eq. (3.12). If we take Eq. (3.12) and insert the spectra after flavor mixing with full cross section we get an energy dependent ratio at the detector. Using the classifications from Ref. [20] one

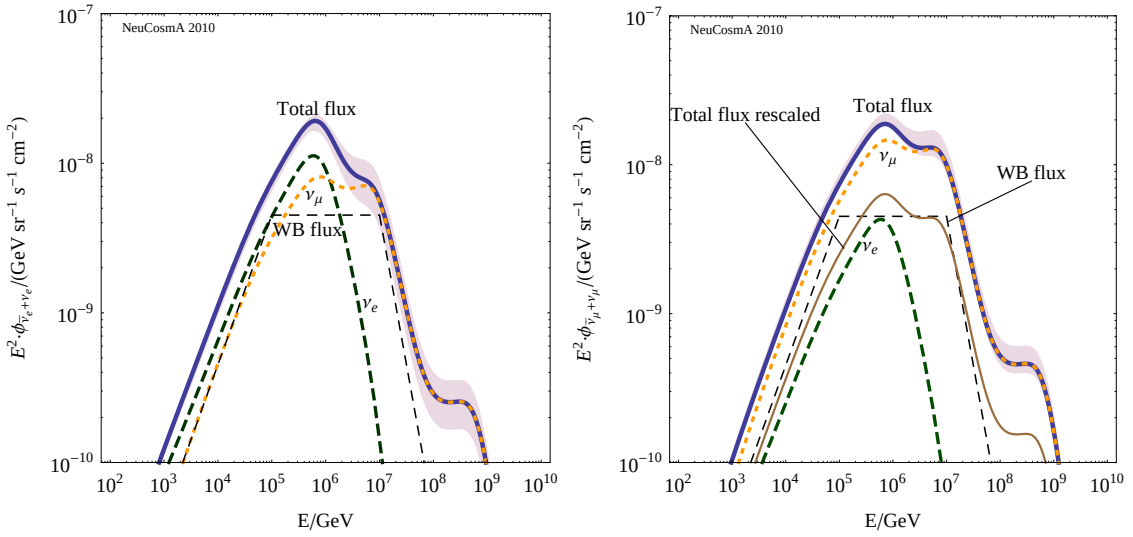

Figure 6.4: The spectra of the $\bar{\nu}_e + \nu_e$ (left) and of $\bar{\nu}_\mu + \nu_\mu$ (right) after flavor mixing is applied. In both graphs the dashed line is the contribution from the produced $\bar{\nu}_e + \nu_e$ and the dotted line is the contribution from $\bar{\nu}_\mu + \nu_\mu$. The features of both spectra are now nearly alike. Only the more pronounced peak near the muon break in ν_e is a directly visible difference. Additionally we included the standard WB-spectrum in both figures for comparison. We also included a rescaled version of the total flux to match the WB flux; bold, solid curve with label "Total flux rescaled". Furthermore, we included the error margins from the uncertainties on the mixing parameters. The effect is relatively small on the logarithmic scale. The visible shaded area represents the current (2010) uncertainties.

can obtain the source class depending on energy from the ratio presented in Fig. 6.5. The figure shows that our GRB has an energy dependent transition from pion beam to muon damped source. The energy range of the transition is independent of the cross section. Only low energy or high energy contributions alter the ratio slightly.

Furthermore, it is possible to obtain bounds on the possible ratios from the current bounds on the mixing angles. By using a χ^2-test to assess the variation of the mixing angles we calculated minimal and maximal possible values for the flavor ratio R. As can be seen in Fig. 6.5 we also included estimated bounds from upcoming experiments to get an idea how the bounds will look in 5 ("2015") and in 15 years ("2025"). As mentioned earlier we use the values by Schwetz et al. from their update in February 2010 [34] with the addition that we force the error margins to be symmetrical around the best-fit values for easier computation. The statistical

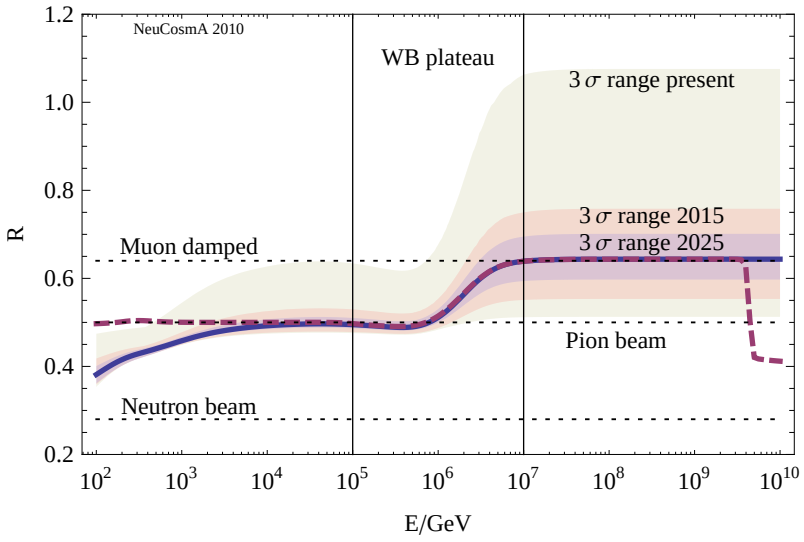

Figure 6.5: Flavor ratio R at the detector as in (3.12) for the full photohadronics treatment (solid curve) and for the WB-like treatment with only the Δ-resonance (dashed curve). Both curves use the best-fit values of the neutrino mixing angles as in Ref. [34]. As one can see only at low energies derivations are visible in the flavor ratio. The general tendency is a ratio of 0.5 (pion beam) at low energies which goes into ≈ 0.64 (muon damped) at higher energies with the transition above 10^6 GeV. At low energies (below ≈ $10^{3.5}$ GeV) the full photohadronic treatment leads to a ratio resembling the transition from neutron to pion beam while the WB-like spectrum has the features of a pure pion beam. For better orientation the levels of the three source classes are included as horizontal lines at $R \simeq 0.28$ (neutron beam source), $R = 0.5$ (pion beam source) and $R \simeq 0.64$ (muon damped source). The jump of the WB-like ratio at high energies (above ≈ $10^{9.5}$ GeV) is a numerical artifact. The shaded areas represent the current bounds to the ratio from the uncertainties of the mixing angles. The smaller sections are from the predicted bounds in the year 2015 and 2025 due to better experimental data.

measure χ^2 is defined as

$$\chi^2 = \frac{\left(\sin^2\theta_{12} - \sin^2\theta_{12}^{\text{B.F.}}\right)^2}{\left(\delta\sin^2\theta_{12}\right)^2} + \frac{\left(\sin^2\theta_{23} - \sin^2\theta_{23}^{\text{B.F.}}\right)^2}{\left(\delta\sin^2\theta_{23}\right)^2} + \frac{\left(\sin^2\theta_{13} - \sin^2\theta_{13}^{\text{B.F.}}\right)^2}{\left(\delta\sin^2\theta_{13}\right)^2} \quad . \tag{6.6}$$

Here $\sin^2\theta^{\text{B.F.}}$ denotes the best-fit value and $\delta\sin^2\theta$ is the σ deviation. The values of the angles in our scan were picked to be sufficient for $\chi^2 = 9$. To obtain the needed quantities we must extract the different parameters from the literature. $\sin^2\theta_{12} = 0.318^{+0.019}_{-0.016}$ from Table A1 in Ref. [34] will translate to $\sin^2\theta_{12}^{\text{B.F.}} = 0.318$ and $\delta\sin^2\theta_{12} = 0.016$ which is the simplified symmetric deviation. With the same method we get $\sin^2\theta_{23}^{\text{B.F.}} = 0.50$ and $\delta\sin^2\theta_{23} = 0.06$ as well as $\sin^2\theta_{13}^{\text{B.F.}} = 0$ (fixed) and $\delta\sin^2\theta_{12} = 0.009$. These are the values for the current bounds. The expected

sensitivities at around 2015 rely on the improved 3σ bounds on θ_{13} from Daya Bay $\sin^2\theta_{13} \leq 0.012$ and θ_{23} from T2K $0.426 \leq \sin^2\theta_{23} \leq 0.574$ [84]. Beyond these, a neutrino factory may improve the bounds even further: $\sin^2\theta_{13} \lesssim 1.5 \cdot 10^{-5}$ [85] and $0.46 \leq \sin^2\theta_{23} \leq 0.54$ [86], which we label "2025". For θ_{12}, the errors may improve somewhat, but new generations of experiments are not assumed here. Since θ_{12} is of secondary importance in Eq. (3.10), we do not consider future improvements. To show the impact of these uncertainties we included the possible ranges of the neutrino spectra and of the ratio R for current error ranges, for the projected errors in 2015 and in 2025 as shaded areas in Figs. 6.4 and 6.5.

7. Effect of parameter distribution on flux shape and flavor ratio

After having established the modified spectral shape expected for neutrinos from a single GRB we now want to look at the effect of certain parameters on the spectrum and how the sampling of a set of GRBs affects the diffuse flux. An important aspect when discussing the parameters of a model is to find a set of uncorrelated parameters. These parameters have to affect the results obtained with this model essentially. However, there are, in general, correlations and connecting conditions between different parameters resulting from the basic physics of the model. In the worst case for the identification of parameters there are "degenerate" results, obtained from slightly different parameter sets. As shown in Table 6.1 we can easily find two sets of parameters which reproduce (nearly)[1] the same spectral shape. Moreover, some parameters of a model might not be directly measurable, as it is the case for GRBs. Therefore, it is vital to define which variables will be varied, which will be assumed fixed and, also, in which reference frame the assumptions are made. Since our code designed to simulate the particle production at the source we hypothesize that we only need parameters characterizing the engine for the calculation of the neutrino flux. Therefore, quantities, such as the Lorentz factor Γ or the magnetic field B, are a consequence of the chosen engine. Thus, for long GRBs these parameters can be assumed to be determined by their progenitors. These are considered to be collapsing massive stars, as stated in section 4.1. Each star, with its mass, its metallicity and all its other properties, already defines how the eventual death of the star will look like. *E.g.* the stellar rest mass sets a limit on the total isotropically emitted energy amount E'_{iso}. Thus, the burst duration t' and the isotropic (total) luminosity L'_{iso} are already confined since their product is E'_{iso}. For other quantities similar reasoning applies. As described in section 6.1, we need the bulk Lorentz factor Γ, which may already be defined by the central engine of a GRB, for our simulations. Moreover, we need the magnetic field B at the collision radius R'_C, which we assume to be a property of the jet. As explained in the previous section, synchrotron

[1] There are some minor differences between the results of the two parameter sets, but they are negligible.

losses are considered to be the main loss mechanism. Therefore, the magnetic field is essential for our calculations. Note, however, that depending on the model all quantities are correlated. Even if we only vary the Lorentz factor or the magnetic field explicitly, the internal connections can also lead to a change of other parameters or measurable quantities of the burst. The third parameter we will consider for the effect of parameter distribution is the redshift z. It is somewhat disconnected from the other two properties since it is a property of the distance to the object and not of the object itself. However, the cosmic expansion affects observational data as well. As described in section 2.2 these effects have to be carefully discussed. A detailed discussion of the particular consequences of each parameter choice will be done in the next sections. Nevertheless, the general approach is to assume that the parameters of the engine (apart from Γ), such as the source luminosity $L'_{\rm iso}$ and the burst duration t', are fixed in the SRF. Moreover, for the jet parameters we assume that jet opening angle $\theta_j > 1/\Gamma_{\rm min}$. And, collisions are assumed to take place at a set distance R'_C. As a result of this assumption the scaling of the variability time needs to be $t_v \propto \Gamma^{-2}$. Generally, changes of observed quantities are in this model a result of the boost with different Lorentz factors. However, spectral features, which vary among bursts and are not necessarily described by our chosen values, are also assumed fixed. The discuss of their effect has to be done at some point in the future.

For our goal to simulate a (quasi-)diffuse flux of GRB neutrinos we need a sample of bursts. To obtain a relatively realistic sample of bursts one has to estimate the number of bursts expected to show up in a certain time window. As a quick and rough estimate we will assume 1000 GRBs per year over a time of ten years leading to a total of 10000 bursts. Hence, we will simulate a set of 10000 bursts for each parameter using a Monte Carlo algorithm to pick a value for the parameter. The actual number of detected bursts may be lower over the time of ten years since we neglect the detection efficiency and the field of view of the detectors. Furthermore, we assume that all GRBs are "long" GRBs. By this choice we omit the contribution of "short" GRBs, which amount for roughly 1/3 of all bursts, as stated in Ref. [24]. However, it is assumed that these bursts have a different precursor than the long bursts and, therefore, a different central engine. Furthermore, short burst display a harder photon flux spectrum. Hence, the restriction on long GRBs is a necessary simplification to ensure we can correctly calculate the neutrino flux, and simulate the diffuse flux.

7.1. The effects of the distribution of the Lorentz factor

The first parameter we consider is the Lorentz factor. Even though *Fermi* bursts represent the current state-of-the-art data there is so far only a comprehensive study of the spectral features of 438 GBM bursts, see Ref. [57], but none on parameters such as the Lorentz factor. Due to this we use the well analyzed BATSE data, as already mentioned in section 4.2. By this we confine our analysis to one measured data set and its analysis methods. The method used in Ref. [30] may not be correct, due to its assumptions leading to Eqs. (4.2) and (4.3). Other methods, such as the determination of the pair-creation cutoff, as used in *e.g.* Refs. [67, 87], or the observation of the rise of forward shock emission, *e.g.* Ref. [88], might give a different result from the same set of observational data. Nevertheless, we will try to reproduce the result obtained by Guetta et al. in Ref. [30], see Fig. 4.2. For this purpose we use Monte Carlo generation consisting of two steps. First, we generate a Lorentz factor Γ as

$$\begin{aligned} \Gamma \quad &= \quad 10^x + \mathit{offset} \\ &\text{with} \quad P(x) = \frac{1}{\sqrt{2\pi\,\sigma^2}} \exp\left(-\frac{(x-\bar{x})^2}{2\,\sigma^2}\right) \end{aligned} \tag{7.1}$$

with $\bar{x} = 2.6$, $\sigma = 0.25$ and $\mathit{offset} = 50$. Our ansatz for the parameter generation is to distribute the exponent x of 10^x using a Gaussian, which leads to an asymmetric shape on the linear scale. The *offset* had to be introduced to shift the whole distribution to match the minimal value $\Gamma_{min} \gtrsim 100$ as well as giving it a peak on linear scale at ~ 300. This part can be called the generation of a burst. Since we are trying to simulate an observed distribution, we still need to make sure that the burst is observed. Thus, the second step is to make sure that Eq. (2.26) is fulfilled. As described in section 2.3, the emission from a relativistic jet can only be observed if the viewing angle θ is smaller than $1/\Gamma$; see Eq. (2.26). In case of $\theta > 1/\Gamma$ the radiation is only weakly boosted or even suppressed to the point that a burst can no longer be separated from the background, see Fig. 2.1. Therefore, we take this limitation into account by additionally generating a viewing angle θ with uniform distribution from 0 to $\pi/2$. It is then tested, if the pair of generated viewing angle θ and Lorentz factor Γ obey the aforementioned condition $\theta \leq 1/\Gamma$. Only if it is fulfilled the burst is considered to be "observed" and taken for our sample. Note that this viewing angle is not considered for the calculation of the (Doppler) boost factor. The simplification from Eq. (2.27) is still valid, and we assume that the boost factor

inside the light cone is $\sim \Gamma$. However, this check of the viewing angle leads to a $1/\Gamma$ suppression of bursts with high Γ in the distribution. The final distribution of the burst parameters $P(\Gamma)$ can be quantified using Eq. (5.5):

$$P(\Gamma) = \frac{1}{\Gamma} \cdot \frac{1}{\sqrt{2\pi\,\sigma^2}} \exp\left(-\frac{(\log_{10}(\Gamma - 50) - \bar{x})^2}{2\,\sigma^2}\right) \cdot \frac{1}{\ln(10) \cdot (\Gamma - 50)} \quad . \tag{7.2}$$

The resulting distribution for 10000 simulated bursts on linear scale is plotted in Fig. 7.1. The depicted range from 0 to 1400 reflects the data range shown in Fig. 4.2. The theoretically obtained maximum of $P(\Gamma)$ from Eq. (7.2) using the aforementioned parameters is 268 (≈ 300). By comparing the histograms of the measured values, Fig. 4.2, and our theoretical distribution, Fig. 7.1 (left plot), it shows that our rather simple approach for the distribution of Γ at the source reproduces the observed distribution quite well. On another note, it should be mentioned that the relation between viewing angle and Lorentz factor must be carefully distinguished from the mostly given comparison of the jet opening angle θ_j to the Lorentz factor Γ. The relation of $\theta_j \geq 1/\Gamma$ is needed to apply the fireball model even though the emission is from jets, which we implicitly assume to be true.

For comparison we also simulate a distribution from the literature. A distribution of Γ was given in Ref. [89], which we will use as a second possibility. It is similar to our approach, using a Gaussian distribution for the exponent with $\bar{x} = 2.6$ and $\sigma = 0.3$. The main difference is that the Lorentz factors are only generated using the distribution as in Eq. (7.1) (with *offset* = 0). Our second step, the creation of a viewing angle and subsequent the application of Eq. (2.26), is missing. This leads to the generation of more high Γ values compared to our model. Moreover, due to the missing *offset* there are as well a number of bursts which have a Lorentz factor below 100, which is generally excluded by theory. As a result the probability of the Lorentz factor peaks at $\Gamma = 247$ in case of this second distribution model. Since we assume most parameters to be fixed at the source, the observed values vary proportional to the appropriate power of the Lorentz factor, see section 2.1.

We use the spectra of this sample to gain average values of the expected muon neutrino spectra by summing over all bursts and then normalizing the total spectrum with Eq. (6.1). As can be seen in Fig. 7.2 (left column) the averaged spectrum is for both Γ distributions shifted to higher energy values as well as being higher in flux. In our approach this is the result of relativistic boosting. The observed energy

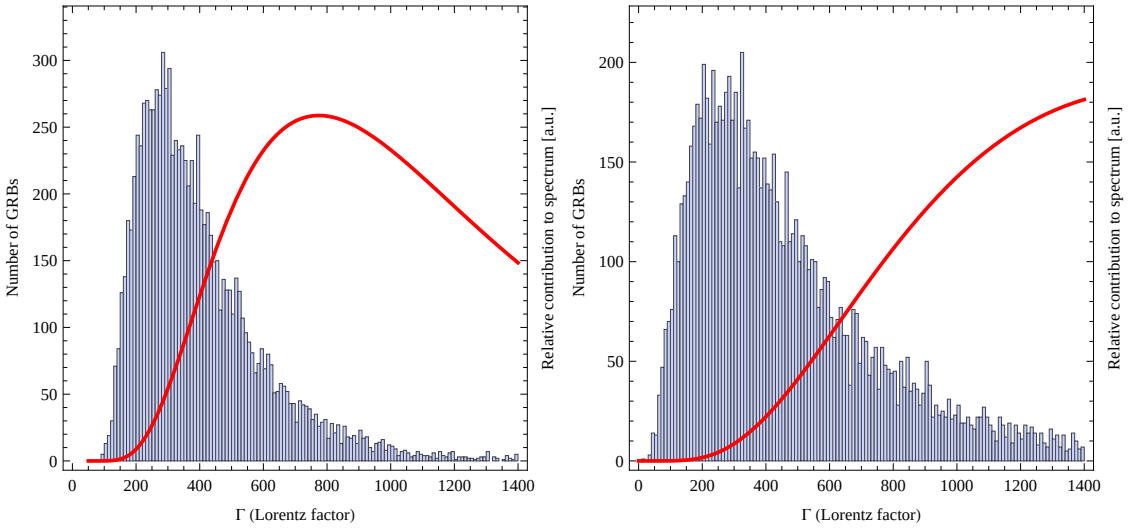

Figure 7.1: Distribution of the 10000 bursts on a linear scale in form of a histogram. The chosen distribution in the left plot tries to model the result of Ref. [30]. It was managed with a parameter generation in two steps, see text for details. Depicted on the right is the result for the distribution suggested in Ref. [89]. The red curve in each plot is the relative contribution. It weighs the probability of a burst with how the flux $E^2\,\phi(E)$ scales with Γ, *i.e.* $\Gamma^4 \cdot P(\Gamma)$.

depends linearly on the Lorentz factor; $E \propto \Gamma$. The effect on the flux is even stronger since $E^2\phi \propto \Gamma^4$. This leads to a dominance of bursts with high Γ even though most bursts have a value of around $10^{2.5}$. This is in contrast to results by Alvarez-Muniz, Halzen and Hooper in Ref. [90]. In the article the authors claim that low Γ bursts dominate, which only is true if values are assumed fixed at the observer. However, it has to be carefully discussed at some point in the future, if it is reasonable to assume that the parameters are fixed at the source and that higher Γ lead to higher contributions, or not. Here, we will always assume that the values at the source are fixed. To quantify which bursts dominate we also calculate the relative contribution to the total flux spectrum $\Gamma^4 \cdot P(\Gamma)$ and plot it in the histograms of Fig. 7.1, depicted as a red curve. As can be seen from the graphs our distribution (upper row) has a peak contribution from bursts with $\Gamma = 774$, while the second distribution is dominated by bursts with $\Gamma > 1400$ for our source assumptions. This leads to a discrepancy between the peak of the number of bursts compared to the contribution. The number of bursts contributing the most to the total flux is relatively low. In case of a smaller sample size this may lead to fluctuations in the flux. However, apart from the shift to higher values there are no effects on the spectral shape from our 10000 burst sample. The double peak shape is still clearly visible. To better understand the contribution from different values of Γ we also plot the flux spectrum for all

bursts with $\Gamma \leq 300$, ≤ 500 and ≤ 1000 in addition to the total flux in case of our chosen distribution (Eq. (7.1)), which is depicted in the upper left plot of Fig. 7.2. For the distribution suggested by Gupta and Zhang we include the same spectra, but as one can see from the lower left plot in Fig. 7.2 the contribution from bursts with $\Gamma \leq 300$ is so low that it is no longer in the chosen plot range. The effect of our chosen distribution (upper row) is not as strong as the one of the distribution given in Ref. [89] (lower row), which is due to the higher amount of high Γ bursts in the latter distribution. However, this change of Γ has implications on several other parameters. We assume that the luminosity at the source is fixed. If now the Lorentz factor changes, this leads to a change in the observed flux and therefore to different contributions depending on Γ, as mentioned before $E^2\phi \propto \Gamma^4$. Furthermore, the observed break in the photon spectrum scales $\propto \Gamma$, as in Eq. (2.23). This results in a variation of the observed $\varepsilon_{\gamma,\mathrm{break}}$ even though $\varepsilon'_{\gamma,\mathrm{break}}$ is assumed fixed. Moreover, just by using scaling relations, such as $\varepsilon_{\gamma,\mathrm{break}} \propto \Gamma$ and $L_{\mathrm{iso}} \propto \Gamma^2$, it may be possible to obtain observed relations, such as the Yonetoku relation $L_{\mathrm{iso}} \propto \varepsilon_{\gamma,\mathrm{break}}$, see Ref. [91] on the Yonetoku relation. The whole photon spectrum is affected by this, the minimal as well as the maximal energy. Following this line of argumentation it could also be possible to understand why *Fermi* LAT bursts tend to have Lorentz factors $\Gamma \geq 1000$. Only a few bursts detected with the GBM on *Fermi* are also detected in the higher energy range of the LAT detector. However, these few bursts generally have a high Γ. In our approach highest energy photons would naturally be associated to high Lorentz factors. But this has to be carefully studied in the future, when comprehensive data of all *Fermi* bursts is available. To conclude, the change of Γ leads to sensitive changes in many of the observable parameters.

We also calculate the change of flavor ratio R from Eq. (3.12) which is depicted in the right column of Fig. 7.2. Here the effect is similar to the one on the spectra themselves. The whole ratio evolution is shifted (or boosted) up in energy. Again the effect of the second distribution is stronger and the transition from "pion beam" to "muon damped" is at higher energies compared to the single burst. Also at low energies (below $10^1\,\mathrm{GeV}$) the transition to a "neutron beam" source is wearing of and the ratio seems to form another plateau at the value of $R = 0.4$. For the first distribution one can only guess if this will happen. However, for the second distribution this effect can be clearly seen, as depicted in the lower right plot of Fig. 7.2. In general the shift of the spectra may lead to the features being observable in different detectors, such as from IceCube to *Auger*. In particular, it would be interesting to observe the transition between the "source classes". Unfortunately, for

comprehensive result of the flavor ratios we would need results for all flavors over the whole energy range, which is not feasible at the moment. Thus, the information in the flavor ratios on the Lorentz factor Γ is restricted to certain energy ranges. It might be possible to measure the flavor ratio for $E \gtrsim 1\,\mathrm{TeV}$.

7.2. The effect of the distribution of the redshift

The next parameter we discuss is the redshift z. The basic assumption for our analysis is that long GRBs are the result of the collapse of massive stars (collapsar model). The initial mass of the progenitor has to be high enough that the death of the star results in a core-collapse supernova and the birth of a stellar mass black hole (BH). The initial mass of the progenitor therefore has to be $\geq 8\,M_\odot$. Depending on the initial mass function and the star formation history one is able to model the possible distribution of GRBs in redshift z. We test several models depending on the parameterization of the star formation history, which implicitly needs a certain initial mass function. Also we apply a recently proposed correction factor for one of the models. The differential flux ϕ_ν depending on z can be calculated with the following formula taken from Ref. [70]:

$$\begin{aligned} \phi_\nu(E_\nu) &= \Delta t \,\frac{\Delta\Omega}{4\pi} \int_{z_{\min}}^{z_{\max}} \mathrm{d}z \,\frac{\mathrm{d}\dot{N}}{\mathrm{d}z}\,\frac{\mathrm{d}N_\nu((1+z)E_\nu)}{\mathrm{d}E'_\nu} \\ \text{with } E'_\nu &= (1+z)E_\nu \quad . \end{aligned} \tag{7.3}$$

Here Δt and $\Delta\Omega$ are the observing time and the sky coverage which correct the observational data depending on the parameters of the experiment. The boundaries of the integral are chosen to be $z_{\min} = 0.023$ and $z_{\max} = 6$, as discussed in section 2.2. $\frac{\mathrm{d}N_\nu((1+z)E_\nu)}{\mathrm{d}E'_\nu}$ is the flux spectrum of a single burst at the source. It is however already relativistically boosted. $\frac{\mathrm{d}\dot{N}}{\mathrm{d}z}$ denotes the expected redshift distribution of GRBs. We will compute the expected redshift distribution with the formula given in Eq. (4.5). Note that $\dot{\rho}_*$ is normally given in $M_\odot\,\mathrm{yr}^{-1}\,\mathrm{Mpc}^{-3}$ in the literature. For this we would need a proportionality constant such as $\dot{\rho}_*(z=0)$, which we have neglected in all prior descriptions. We are able to do this since we only need the probability of a burst to appear for our Monte Carlo sampling, and not the real (measured) rate. In particular, all proportionality constants are absorbed in the total normalization of the quasi-diffuse flux spectrum.

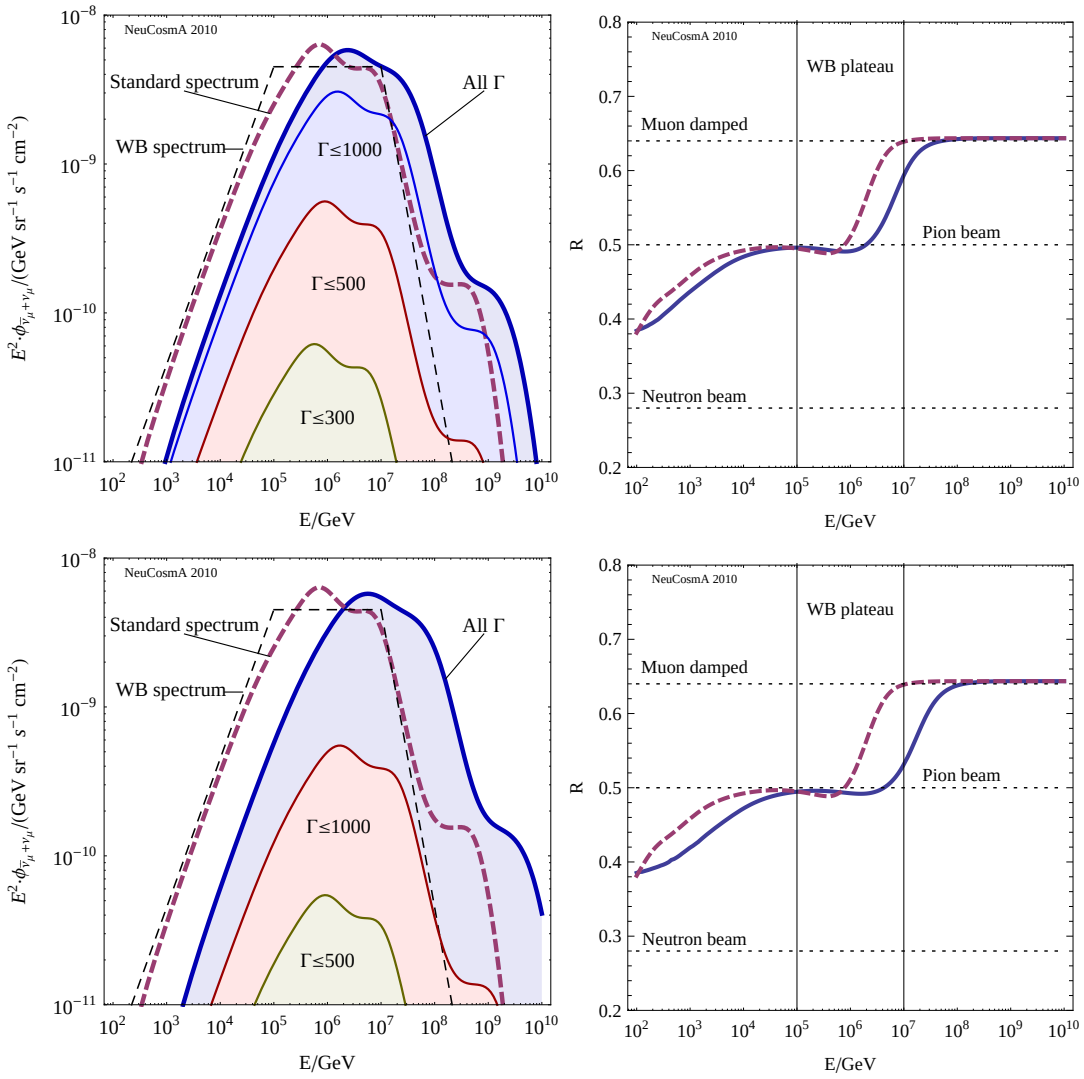

Figure 7.2: Effect of the Lorentz factor Γ on the muon neutrino spectrum (left column) and on the flavor ratio R (right column). The upper row represents the effect of our model of the Lorentz factor Γ distribution from Eq. (7.1). The lower row is showing the effect of a similar ansatz suggested in Ref. [89]. The strong dependence of the observed quantities on Γ leads to the shown shifts. High values of Γ lead to higher values of the flux and the whole shape is shifted to higher values of the observed energy.

The current "standard" parameterization of the star formation rate $\dot{\rho}_*(z)$ was proposed by Hopkins and Beacom in 2006 [21]. It utilizes the initial mass function by Baldry and Glazebrook, see Ref. [69], to calculate a function describing the formation of stars depending on the redshift z. The analytic version of their star formation rate can be found in Eq. (4.4). We will be considering the effect of this star formation rate with and without the correction $\mathcal{E}(z) \propto (1+z)^{1.2}$, see Eq. (4.5). For our Monte Carlo sampling we need to invert the result of the integration of Eq. (4.5) over z numerically, as explained in Eq. (5.3) from section 5.2. The two histograms of the generated number of bursts as a function of the redshift z can be seen in Fig. 7.3.[2] The first distribution (left plot of Fig. 7.3) is generated using the aforementioned star formation rate with a constant fraction of stars collapsing and producing a GRB. The proportionality fraction is absorbed in the total normalization. The second distribution (right plot of Fig. 7.3) has the additional factor of $\mathcal{E} \propto (1+z)^{1.2}$. As one can see from the plots the SFR without the correction factor leads to a peak in the burst distribution between $z = 1-2$ which is the quoted "typical range" from Ref. [66]. With the correction factor applied the range of highest burst production is spread roughly between $z = 1$ and $z = 4.5$ with the peak at approximately $z = 3$. Additionally we add the relative contribution we also introduced for the Lorentz factor Γ. In case of the redshift it goes as $(1+z)^{-4}\, P(z)$ with $P(z) \propto \frac{\mathrm{d}\dot{N}}{\mathrm{d}z}$. It is shown as a solid red curve in the plots of Fig. 7.3.

We then again use these parameters to simulate GRBs with the redshifts obtained in the previous step. We add up all the observed flux spectra $E_\nu^2\, \phi_\nu(E_\nu)$ and normalize the whole flux with the integrated energy from Eq. (6.1), as done in the previous sections. Again, we have to consider how quantities are changed by assuming a different value of z. As in section 7.1 we have assumed that the luminosity, the magnetic field, the total energy output, and, here, the Lorentz factor are fixed at the source. The cosmologic redshift leads a shift in energy, as described in Eq. (2.23). Thus, as for the Lorentz factor a different z leads to a different observed photon break $\varepsilon_{\gamma,\mathrm{break}}$, and maximum photon energy $\varepsilon_{\gamma,\mathrm{max}}$. Furthermore, the observed luminosity (or flux) decreases $\propto (1+z)^{-2}$. And, the observed time scales grow $\propto (1+z)$, if they are fixed at the source. The effect of the redshift is a bit decoupled from the source and it only shifts the parameters slightly, compared to the Lorentz factor. Consider, that $(1+z)$ is less than 10 for the highest redshift we consider. Therefore the effect of z is orders of magnitude smaller than the effect of Γ. So far, new bursts from *Fermi* have not

[2] The distribution depending on the redshift can also be analyzed with logarithmic binning. Since there is some confusion in the literature about what "log" stands for - either to the base of 10 or to the base of e - we stay on the linear scale. Both logarithmic versions for the distribution with the correction factor $\mathcal{E}(z)$ can be found in Fig. D.1 in the Appendix D.

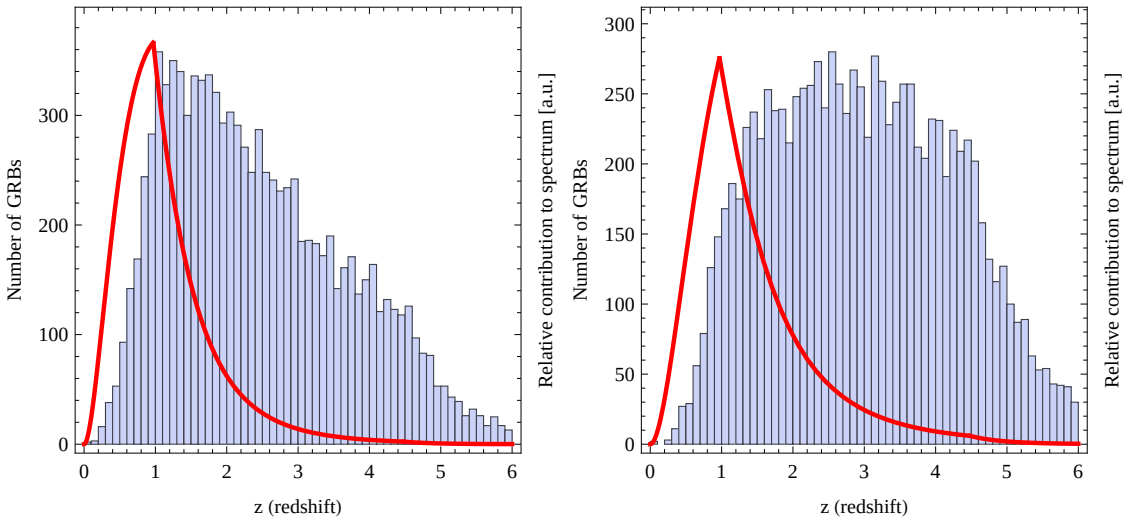

Figure 7.3: Histogramatic distribution of the 10000 bursts as a function of redshift. The chosen distributions try to model the GRB rate using the star formation history by Hopkins and Beacom [21] (left plot) and the same SFR with a correction by Kistler et al. [70] (right plot). From the spread of bursts depicted here one can see that for the pure SFR most of the burst have a redshift z between 1 and 2 while for the distribution with the correction for GRB the bursts are spread in a much broader range (roughly between $z = 1$ and $z = 4.5$. The relative contribution to the total flux is shown as a solid red curve (in arbitrary units).

altered the concept of long GRBs being the result of collapsing stars. However, there are a few bursts that cannot be classified in the current "short/long" scheme and the rate of high redshift bursts exceeds the estimates from star formation rates, see *e.g.* Ref. [92] and references within. As before we plot the muon neutrino spectrum at the observer (with neutrino mixing) and the flavor ratio R from Eq. (3.12). Both the muon neutrino spectrum and the flavor ratio R are for the averaged spectrum similar to the single burst versions but shifted to higher energies. Also the flux is higher compared to the single burst. This indicates that nearby bursts dominate this distribution. Since the spectral features such as the double peak structure or the peak from kaon decays are still visible it is reasonable to assume that low z bursts mainly contribute to the spectrum. In general, the redshift has the reciprocal effect of the Lorentz factor on the flux or the energy. As can be seen from the relative contribution that the main contribution comes from bursts with redshift just below $z = 1$ independent of the correction factor. We also plot the spectra for all bursts with $z \leq 0.1$, ≤ 0.5, and ≤ 1.0, see Fig. 7.4. As expected from the considerations on the order of the redshift, the contributions up to a certain redshift are much closer to the total value compared to the case of the Lorentz factor in Fig. 7.2. Moreover, when comparing the two distributions in redshift it is evident that the correction

factor leads to a slightly higher contribution from bursts with high redshifts but does not change the peak contribution itself. The theoretical analysis of $(1+z)^{-4}\,P(z)$ gives $z = 0.97$ as the peak of the contribution for both distributions.

For comparison reasons we also simulate three more star formation history models by Porciani and Madau taken from Ref. [93], that can be found as Eqs. (7.4)-(7.6) in this thesis. These model the star formation history with one steady function containing exponential functions. The three star formation rates taken from Ref. [93] are

$$\dot{\rho}_*^{SF1} \propto \frac{\exp(3.4z)}{\exp(3.8z)+45} \quad , \tag{7.4}$$

$$\dot{\rho}_*^{SF2} \propto \frac{\exp(3.4z)}{\exp(3.4z)+22} \quad , \tag{7.5}$$

$$\dot{\rho}_*^{SF3} \propto \frac{\exp(3.05z-0.4)}{\exp(2.93z)+15} \quad . \tag{7.6}$$

Again we are only interested in the dependence on z and not the proportionality constant. These functions were used in earlier studies, such as Ref. [71], and we will use them as well by inserting them in Eq. (4.5) to (eventually) show their effect on the ν_μ spectrum and the flavor ratio R. The main goal of these additional simulations is to show that the resulting diffuse neutrino flux is (nearly) independent from the chosen parameterization of the star formation history. As can be seen from the plots in Fig. 7.5. The histograms show that the number of bursts differs from the two previous models, see Fig. 7.3, however the relative contribution is similar. The main contribution is again from bursts with $z \lesssim 1$, more precisely $z = 0.94$ for SF1 from Eq. (7.4), $z = 0.91$ for SF2 from Eq. (7.5), and $z = 0.88$ for SF3 from Eq. (7.6). It can therefore be said quite safely that the current observational data suggests that the main contribution to the total neutrino flux comes from bursts with redshift $z \lesssim 1$.

The effect on the spectra for all the three distributions is similar and comparable with the effect of the distribution utilizing the star formation rate by Hopkins and Beacom. As said before, the bursts with redshift $z \lesssim 1$ contribute most leading to a shift to higher energies compared to our "standard" spectrum. Again, the loss due to cosmologic redshift is smaller for lower values of z. Therefore, the spectra are shifted to higher energies. However, the spectral features, such as the double peak and the kaon peak, are still visible, with only slight smoothing effects. And, furthermore, the contributions from the bursts with redshift $z \leq 0.1$, ≤ 0.5, and ≤ 1.0 are relatively close to the total flux. Also, the transitions in the flavor ratios are at higher energies

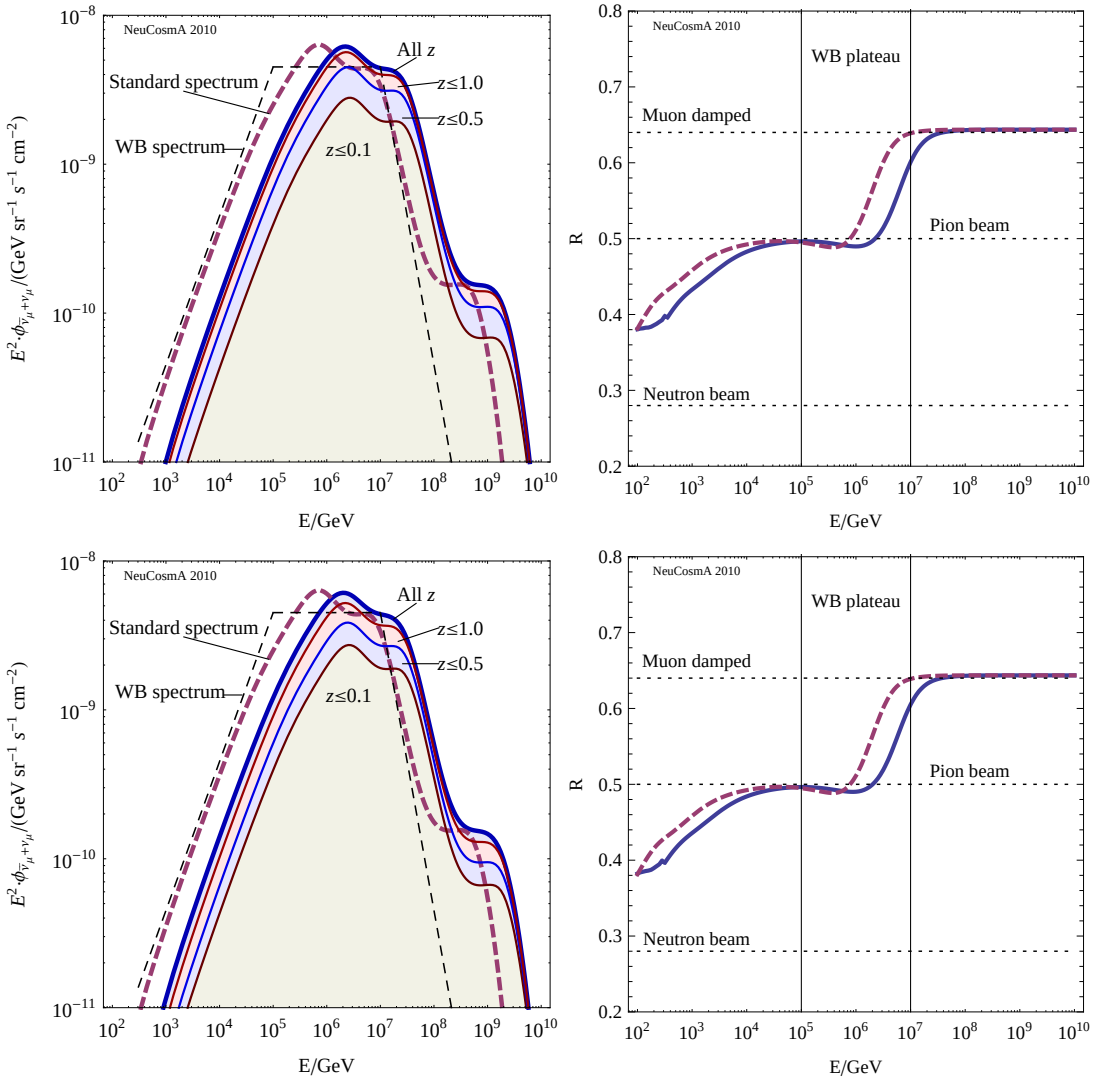

Figure 7.4: Effect of the redshift z on the muon neutrino spectrum (left) and the flavor ratio R (right). The spectrum (left panel) is again shifted to higher energies and is showing higher flux values. In context of the redshift this indicates that probably nearby (low z) bursts dominate the averaged spectrum. This conclusion is also supported by the fact that the smearing of the spectral features is very weak and the double peak structure and the peak from kaon decays are still visible. The flavor ratio of the averaged spectrum in the right panel shows nearly the same behavior as the one for the single burst but shifted to higher energies. Also the low energy behavior is perturbed. Partly due to low statistics. This leads to the jump in the ratio function at $3 \cdot 10^2$ GeV.

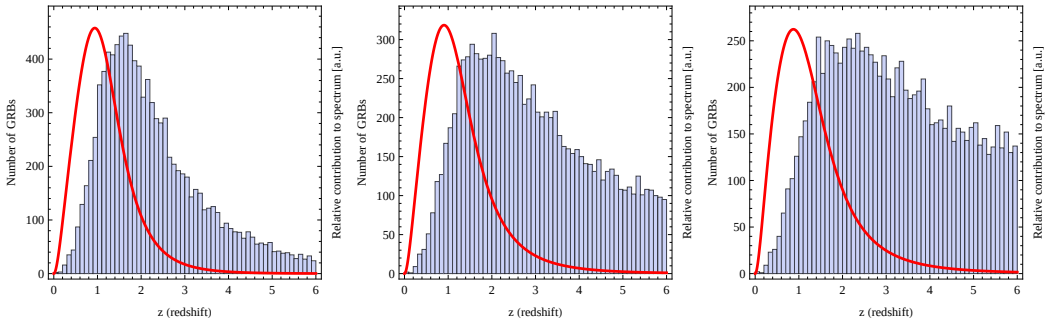

Figure 7.5: Distribution of the 10000 bursts as a function of redshift. The plotted distributions are (from left to right) the result for the star formation rates 1 to 3 by Porciani & Madau taken from Ref. [93]. The solid red curve is the relative contribution of bursts at a redshift to the total flux, $(1+z)^{-4} \cdot P(z)$.

compared to the single burst. The width of the transition region (on logarithmic scale) is, however, unaffected. Hence, we can conclude that the effect of the redshift is considerable, but relatively independent of the chosen distribution. As long as the luminosity at the source is assumed fixed, bursts at $z \lesssim 1$ will dominate the diffuse flux, even if the more discussed bursts from the *Fermi* sample are currently the bursts at highest redshifts.

7.3. The effect of the distribution of the magnetic field

On first glimpse the magnetic field is the simplest of the three parameters we want to look into. As stated at the end of section 4.2 the range of the magnetic field values is roughly between 10^3 and 10^6 G. The values we obtained just from synchrotron cooling considerations are still in the reasonable range, see Table 6.1. Unfortunately the uncertainties on the parameters and the lack of an accepted model to determine the value of B, limit the amount of data on the magnetic field strength. The reasonable and/or needed values depend on the model of the emission region. In our attempt to stay as general as possible we have only adopted all the features of the internal shock model and the fireball model to describe a GRB. This generality is necessary since up to now there is no theory or data on the distribution of magnetic

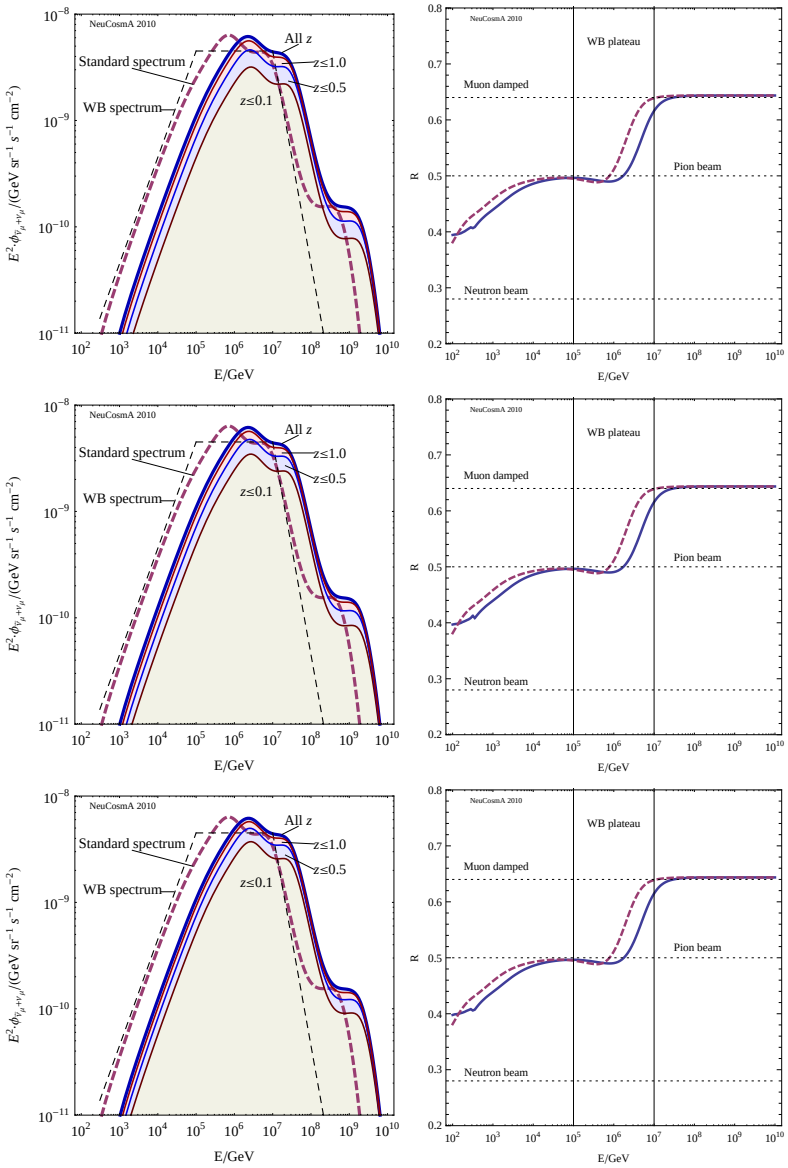

Figure 7.6: Effect of the redshift z on the muon neutrino spectrum (left) and the flavor ratio R (right). The rows show the result for the star formation rates 1 (top) to 3 (bottom) by Porciani and Madau. The spectrum (left panel) is again shifted to higher energies and is showing higher flux values. In context of the redshift this indicates that probably close (low z) bursts dominate the averaged spectrum. This conclusion is also supported by the fact that the smearing of the spectral features is very weak and the double peak structure and the peak from kaon decays are still visible. The flavor ratio of the averaged spectrum in the right panel shows nearly the same behavior as the one for the single burst but shifted to higher energies. Also the low energy behavior is perturbed, partly due to low statistics.

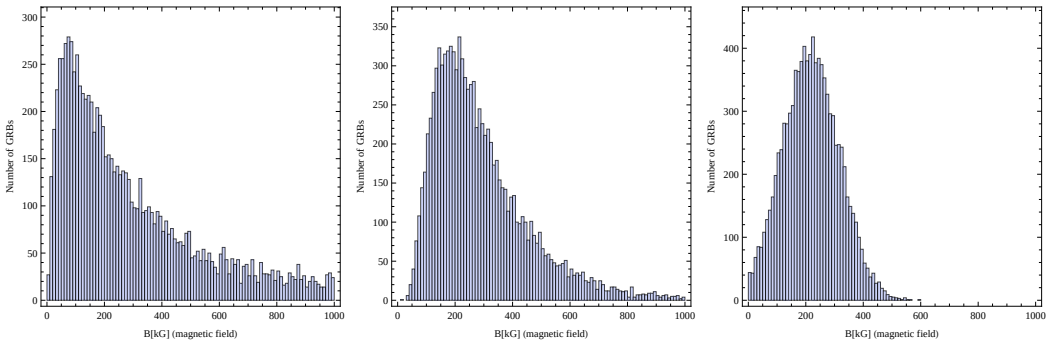

Figure 7.7: Depicted above are three possible distributions of the magnetic field values of 10000 bursts on a linear scale. The main goal was to spread the values between 10^4 and 10^7 G. The displayed distribution on the left is a Gaussian distribution of the exponent of the type 10^x, see Eq. (7.7). The standard deviation σ of this first exponent distribution is 0.75. The second distribution (middle) is using the same ansatz but with a standard deviation $\sigma = 0.25$. The third distribution (right) is a Gaussian distribution on the linear scale with a median value of $\bar{B} = 2.16 \cdot 10^5$ G and standard deviation $\sigma = 10^5$ G.

field strength in GRBs. Hence, we assumed a generic distribution:

$$\begin{aligned} B &= 10^x \\ &\text{with} \quad P(x) = \frac{1}{\sqrt{2\pi\,\sigma^2}}\,\exp\left(-\frac{(x-\bar{x})^2}{2\,\sigma^2}\right) \quad . \end{aligned} \tag{7.7}$$

Here $\bar{x}$ is the median assumed value of the exponent and σ is the width of the distribution. For the first distribution these parameters were set to be $\bar{x} = 5.4$ and $\sigma = 0.75$. Since we use a Gaussian on a logarithmic scale the median value is not the value of highest contribution when rescaled to a linear scale. This effect can be seen in Fig. 7.7. This effect is the result of the conservation of probabilities. Using Eq. (5.5) we can quantify this effect:

$$P(B) = P(x)\,\frac{1}{\ln(10)\,B} \quad . \tag{7.8}$$

As can be seen from Eq. (7.8) the transformation of variables brings an additional $1/B$ suppression of the probability to obtain a B field value. This leads to a shift of the peak from $10^{5.4}\,(= 2.51 \cdot 10^5)$ G to $10^{3.94}\,(= 8.77 \cdot 10^3)$ G. For the second distribution the same model is applied but with $\sigma = 0.25$. This results in a much smaller shift of the theoretical maximum to $10^{5.38}\,(= 2.41 \cdot 10^5)$ G. As a third distribution we test a Gaussian distribution on linear scale with the standard deviation being 10^5 G around the median $\bar{B} = 2.16 \cdot 10^5$ G.

This is a rather simplistic approach and we do not claim that this is the real distribution. The main goal is only to show the effects on the averaged spectral shape. However, as for Γ and z, changing the magnetic field affects other parameters of the GRB. The discussions in sections 7.1 and 7.2 show that it is possible to vary the Lorentz factor and the redshift with only affecting the observed quantities, which is a result of our assumption to fix all quantities at the source. Unfortunately, the magnetic field is more complicated since it is directly connected to the source engine. In our simulations we keep the luminosity at the source, the redshift and the Lorentz factor fixed. As a consequence either the fraction of the total energy stored in the magnetic field ϵ_B or the total energy itself change. While one can be assumed fix, it is mandatory to change the other. If the total energy changes and ϵ_B is constant, then, according to Eq. (4.6), the variation time t_v changes as well. And, for constant luminosity, the burst duration would change proportional to the total energy. Moreover, depending on the model it has to be carefully considered what the lowest possible magnetic fields are to still confine the particles in the shock. If in case of shells the shell thickness is to small, then the acceleration to the highest energies would not be possible. We still need to understand the consequences of changing the magnetic field in the internal shock model, however, this is work beyond this thesis.

As stated before we use a Monte Carlo algorithm to generate 10000 values using the distribution in Eq. (7.7). The normalization for the spectrum is obtained using the integrated energy as defined in Eq. (6.1) to allow "energy conservation". The plots in Fig. 7.8 show the muon neutrino spectrum after oscillation and flavor ratio R, see Eq. (3.12), for the three proposed distributions. In all the plots of the ν_μ spectra we show the averaged spectrum obtained from the 10000 simulated bursts (thick solid curve) and for comparison the spectrum of a single burst obtained in the previous section (thick dashed curve) as well as the standard WB spectrum (thin dashed curve) as in Eq. (4.9). For the first distribution (Gaussian in exponent, high σ) nearly all the features of the single spectrum are smeared out. Instead of the double peak structure with an additional high energy peak from kaons there is only one broad peak as can be seen in the upper left plot of Fig. 7.8. If this kind of distribution is found in reality, and the effect on the spectra is as described in Fig. 7.8, then it will be hard to trace the spectral shape back to GRB. There are no unique features left and the spectrum does not look like the spectrum of a single burst. This will lead to problems in the data analysis of the observed neutrinos. However, this ambiguous shape is a result of our chosen distribution. In the case of

the second distribution, which has a lower standard deviation compared to the first distribution, the spectral features of the GRB neutrino flux are still visible but not as pronounced as for a single burst. This can also be seen when looking at the plots of the flavor ratio R on the right hand side of Fig. 7.8. Here we only plotted the ratios from the averaged spectra and from the earlier obtained single burst. Furthermore, we added the ratios of certain source classes as reference as done in Fig. 6.5. (A description of the source classes can be found in the Appendix C.) The main effect of the magnetic field in this case can be seen in the transition from "pion beam" to "muon damped" source class at around 10^6 to 10^7 GeV. For the first distribution this transition is over a much wider energy range going from roughly $2 \cdot 10^5$ GeV to about 10^8 GeV. This is a clearly visible change from the single burst shape. Hence, if we can measure the flavor ratio from track and shower events we should be able to draw conclusions on the magnetic field distribution. This is also true for the second distribution, even though the effect can only be seen in direct comparison of single and averaged spectrum. The principal broadening stays the same and should be measurable. The third distribution, however, has a slightly different effect on the spectrum. The features are also smoothed out, but the spectrum is higher at high energies. While in the case of the first two distributions the smoothing looked like an averaging effect here the value of the spectrum at high energies is significantly higher than for the single burst. The levels of the single burst are only touched at the peak from kaon decays. Otherwise the value of the (third) averaged spectrum is higher as can be seen in the lower left plot of Fig. 7.8. This can be explained by the absence of high magnetic fields. The spectra extend to higher energies as all charged particles suffer less synchrotron losses. However, it still has to be discussed, if such an absence of high magnetic fields is viable in the different GRB models. The deviation can also be seen in the flavor ratio R as in the lower right plot of Fig. 7.8. Here the ratio calculated from the averaged burst spectra differs from the single burst ratio at energies above 10^6 GeV. As can be seen in the plot the ratio is slightly lower compared to the ratio from a single (standard) burst. This is also due to the missing high magnetic fields since muons are not completely "damped" by synchrotron losses. Thus, if such a lower flavor ratio should be resolvable, it would provide valuable information on the magnetic field. However, apart from this small deviation, the flavor ratios are relatively robust, even for a distribution of the magnetic field. They should, therefore, be similar for all bursts, even when the parameters are not known.

As this analysis shows the detection of a neutrino signal will help to set better bounds on the magnetic field in the emission region of GRBs. Currently, the calcula-

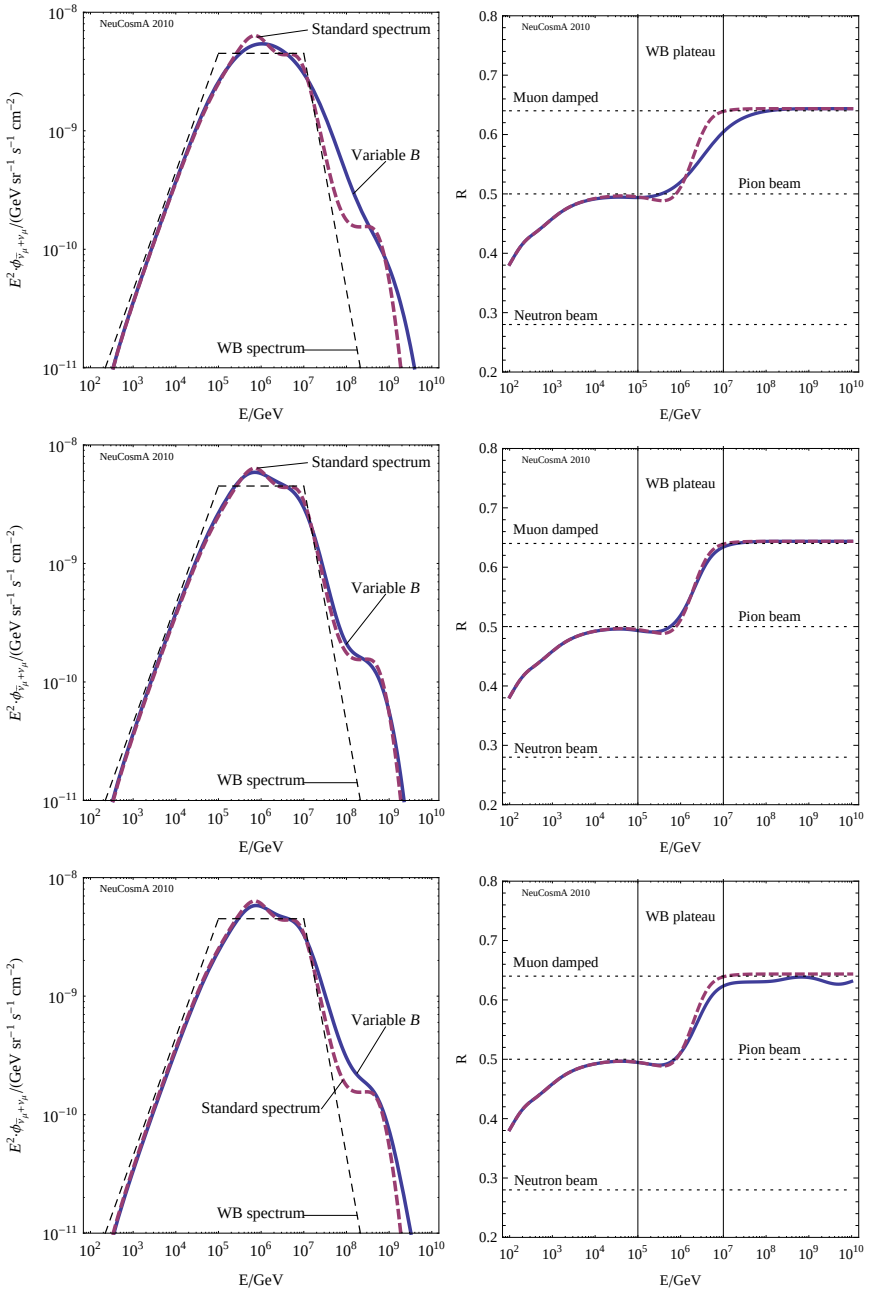

Figure 7.8: Effect of the magnetic field B on the muon neutrino spectrum (left) and on the flavor ratio R (right) for the three distributions from Fig. 7.7. The first two distributions (two upper rows of plots) smear out the features of the spectrum in the form of averaging with the magnitude of the effect depending on the used σ. The third distribution changes the spectrum above 10^6 GeV to higher values in the spectrum and lower values in the flavor ratio; see lower row of plots.

tions of the magnetic field are extremely model dependent. Some models describing the observed GRB light curves with synchrotron radiation from protons need magnetic fields of the order of 10^5 kG, see Ref. [81]. Hence, the detection of single burst spectra would already set far better bounds on the magnetic field of a single burst, the diffuse flux can do the same for all bursts. If the spectral shape predicted by our photohadronic interaction treatment is still visible the magnetic fields cannot have a high spread σ. Correspondingly, if the spectral shape is washed out the variation of B between bursts is high. Also as one could get information on the upper bound by looking at the high energy spectrum compared to the expected spectrum. As was shown by our third spectrum a lack of high magnetic fields would lead to a measurable deviation from the expected spectrum. Moreover, it would also be interesting to know if an effect was from the distribution of a parameter and therefore a systematic deviation or only the effect of low statistics (statistical deviation). We will take a look at this in the next chapter.

8. On the changes to the flux due to low count statistics

Since a high amount of statistics will take a vast amount of time - GRBs are still not detected very often and the amount of GRBs with measured redshift is only a fraction of the detected number - it is more realistic for current studies to take a lower amount of data. As mentioned earlier Ref. [24] suggests that roughly 667 long bursts take place each year over the whole sky. Since IceCube has only access to the northern hemisphere of the sky we can expect that only half of the bursts can be seen with the aforementioned neutrino telescope. A more realistic number is therefore a sample of 300 bursts, which could already be recorded in one year of data acquisition in a stacking analysis. However, for the derivation of the redshift or the Lorentz factor additional requirements on the light curves and afterglow measurements need to be met. For these two parameters we simulate samples of 66 bursts, which reflects the number of bursts used in a recent analysis, see Ref. [70]. For this reason we also computed low statistics samples for the magnetic field B, Lorentz factor Γ and redshift z distribution. We will show that the extrapolation from the low statistics limit, *e.g.* obtained from stacking analysis, to the high statistics limit of the diffuse flux introduces unwanted uncertainties. Moreover, if it is possible to measure single bursts, it might be possible to probe the redshift of GRBs in neutrinos. This would add an additional contribution to the multi-messenger studies of the star formation rate.

We first look at the magnetic field B. We use the distribution given in Eq. (7.7) with $\bar{x} = 5.4$ and $\sigma = 0.75$, which is the first distribution discussed in section 7.3, and generate 300 bursts. The histogram of the distribution of the bursts can be seen in Fig. 8.1.

The main effect expected from the low statistics is that the contribution of the single bursts is higher and that this may lead to additional effects on the total flux. We again use the "energy conservation" method to normalize the total flux of the neutrinos. The resulting spectra of flux $E_\nu^2\,\phi_\nu$ as a function of energy E_ν is

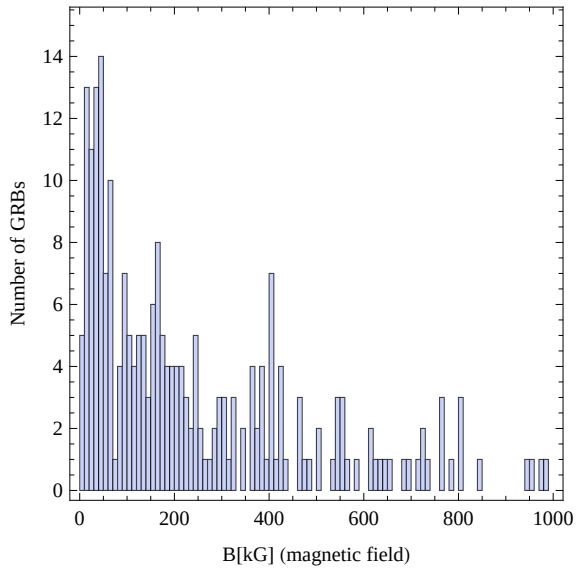

Figure 8.1: Distribution of only 300 bursts following the distribution described by Eq. (7.7) with $\bar{x} = 5.4$ and $\sigma = 0.75$ displayed on a logarithmic scale (with base 10).

depicted as a thick, solid curve in the left plot in Fig. 8.2. Compared to the high statistics result (thin, solid curve) the smearing is even stronger. Instead of the double peak structure, which one sees for a single burst (thick, dashed curve), all kinds of features are washed out in the low statistics version of the total flux. The double peak from μ and π decays is perturbed to one broad peak. The drop of the spectrum after its peak is not as steep as for the single burst and does not have the third peak from the K decays. For comparison, the high statistics result still has a slight nudge left from the kaon peak; see relative position of thick, solid and thin, solid curve in Fig. 8.2. For the flavor ratio R the changes are significant as well. While there is no visible deviation at low energies there is a large change in the size of the transition (energy) range in which the source goes from "pion beam" to "muon damped", that now extends over nearly four orders of magnitude from $10^5\,\mathrm{GeV}$ to roughly $10^9\,\mathrm{GeV}$. Still, the basic flavor ratios stay relatively robust and only the range of the transition between two source classes changes. As stated before this should be measurable in the flavor ratios, leading to information on the magnetic field at the source. However, the uncertainties on the magnetic field are nevertheless high, even when obtained from the flavor ratio.

For the Lorentz factor Γ we use our distribution given by Eq. (7.1) with $\bar{x} = 2.6$, $\sigma = 0.25$, and *offset* $= 50$. In the literature analysis mostly have been done for smaller samples. The correctional factor to the star formation rate was obtained from a 66 burst sample, see Ref. [70]. For this reason we generate five samples with 66 bursts each. We use a different seed for the random number generator for each

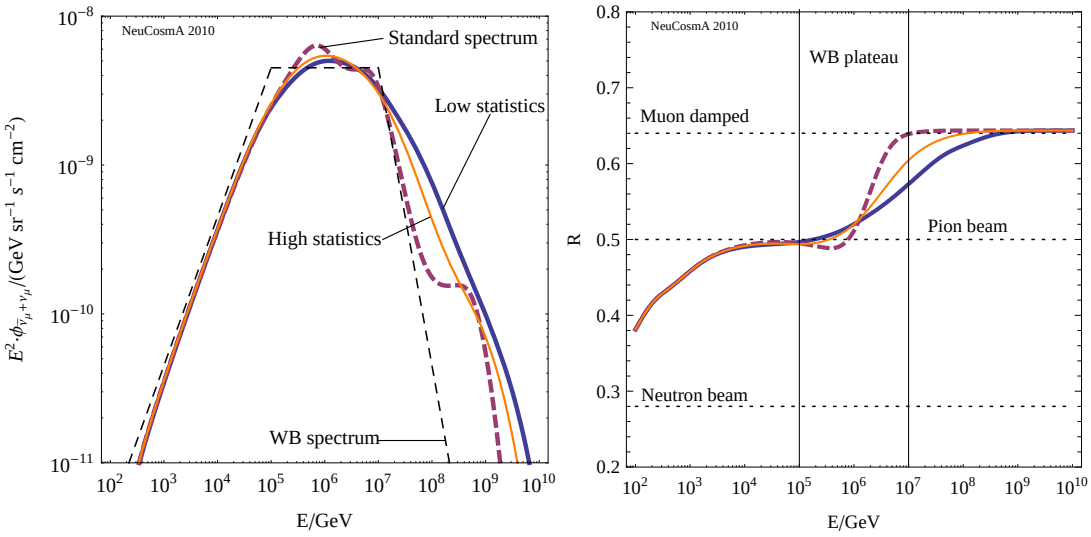

Figure 8.2: The flux of 300 simulated bursts with the magnetic field distributed as shown in Fig. 8.1. The left plot shows the flux spectrum of the ν_μ. Compared to the single burst all the significant features such as the double peak from μ and π decays or the high energy peak from K decay is washed out due to the distribution of the magnetic field. Also the flavor ratio R (right plot, thick solid curve; given by Eq. (3.12)) changes compared to the version for higher statistics (thin solid curve). In case of the low statistics the transition from "pion beam" to "muon damped" source extends over four orders of magnitude which is roughly two orders more than expected. For comparison we included the flavor ratio of a single burst with our standard set of parameters as a dashed curve.

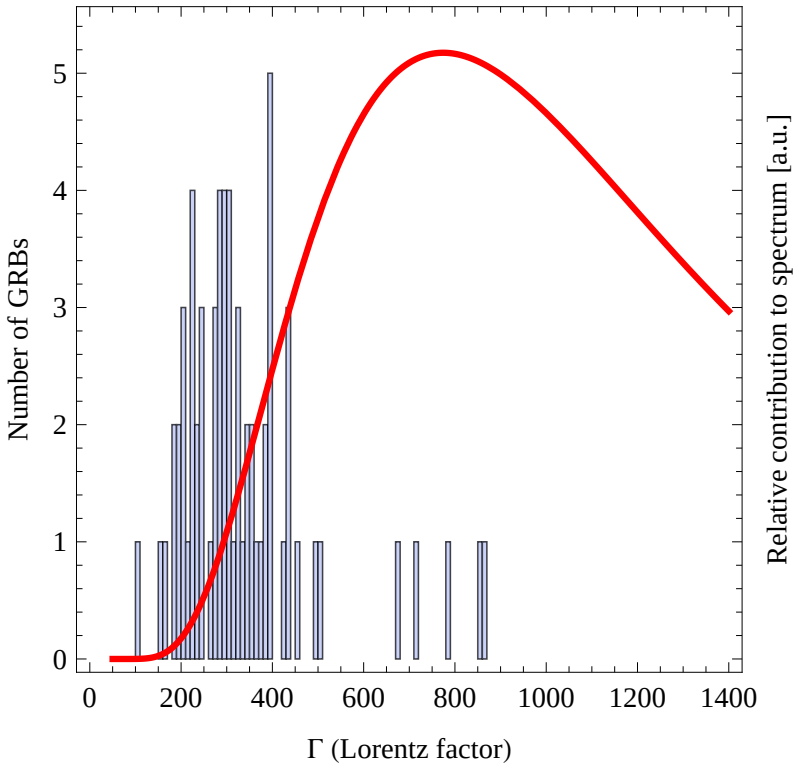

Figure 8.3: Distribution a sample 66 bursts following the distribution described by Eq. (7.1) with $\bar{x} = 2.6$, $\sigma = 0.25$, and *offset* $= 50$. Depicted here is sample 1, see the Appendix E for information on seed. Furthermore, the thick red curve shows the relative contribution of bursts with corresponding Γ, as described in section 7.1. By comparing the number of bursts to the relative contribution one can see that there are only five burst in the range of highest contribution (between $\Gamma = 600$ and $\Gamma = 1000$). This gives rise to additional uncertainties when one uses this low number of bursts to extrapolate a diffuse flux.

of the samples. The data sets are numbered from 1 to 5, and the chosen seeds for each set can be found in the Appendix E. Hence, we plot the generated values of sample 1 in form of a histogram using a bin size of 10 in the range from 0 to 1400. Additionally, we include the relative contribution of a certain Lorentz factor Γ, to visualize the limitations of low statistics samples, see Fig. 8.3. The sample 1 is the chosen example to represent the five data sets. The actual distribution of the 66 bursts is different, however, the qualitative distribution is the same. Therefore, it is sufficient to discuss the effects for one example. As one can clearly see from Fig. 8.3, the number of bursts at Γ that contribute most is low. Only five bursts are in the range of $600 \leq \Gamma \leq 1000$. Thus, one has to expect fluctuations in flux shape and normalization of the burst sample.

We then calculate the expected spectrum of ν_μ after flavor mixing. In the plot of the expected muon neutrino flux after mixing we have included the analytic WB shape (thin, dashed line) and the high statistics flux (bold, dashed line) as references, see Fig. 8.4 (left plot). Furthermore, there are the flux shapes for the five 66 burst samples, depicted as solid lines. The thick, solid line is the result for sample 1, which is also displayed in Fig. 8.3. The four thin, solid lines are the result for four further samples. These depicted curves are the extrapolation from the 66 burst sample up to a 10000 burst limit. Therefore, we added the 66 bursts and scaled them up to 10000 by a multiplication by $\frac{10000}{66}$. This method maintains the relative contributions and variations among the five samples. We have not included a legend for the different 66 burst samples because only the relative variation among the samples is relevant. As one can see from the left plot of Fig. 8.4 there is some variation among the samples. Therefore, it has to be carefully considered before drawing a conclusion from such a small sample. As expected from considering the low number of bursts with high contribution, as in Fig. 8.3, the analysis of such a small sample would be statistics limited. However, the changes of the flux shape are more subtle than for the magnetic field. For each spectrum the double peak structure is still visible as well as the kaon peak at high energies. Yet, the high statistics sample has slightly smoother features compared to the 66 burst samples. Moreover, the result for the expected flux as well as the energies of the features are shifted from sample to sample. Since we fix quantities at the source, the flux and the observed energy scale with the Lorentz factor. The samples scatter around the high statistics spectrum. Three extrapolation results are slightly higher than the high statistics result, two are significantly lower. This is due to the mentioned low number of bursts with Lorentz factor between 600 and 1000. The same holds for the flavor ratio R depicted in the right plot of Fig. 8.4. Here, we again only plotted the flavor ratio R for the sample 1 as an example for the five 66 burst spectra. The bold, dashed line is the flavor ratio of a single burst, while the thin, solid line is the flavor ratio for the high statistics sample. The transition from a mixed source between "neutron beam" and "pion beam" to "pion beam" to "muon damped" source is practically the same. Only a small kink at roughly $E \approx 10^{2.5}\,\mathrm{GeV}$ is not the same as in the upper right plot of Fig. 7.2. As stated before this is an effect of low statistics in this energy region. Hence, the flavor ratio is nearly unaffected by the low statistics. Therefore, it is possible to estimate that the result of a stacking analysis with such a low number of bursts will have an uncertainty of roughly one order of magnitude on the flux level (for GRBs). However, a sample of 66 bursts would already be sufficient to obtain representative information on the flux shape and the flavor ratio. Thus, one can

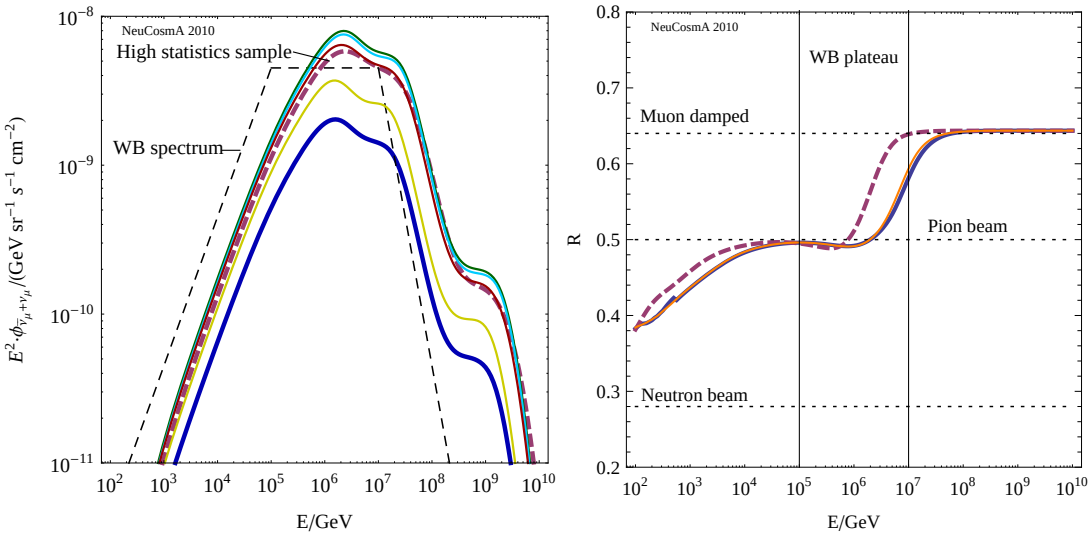

Figure 8.4: The flux of 66 simulated bursts with the Lorentz factor distributed as shown in Fig. 8.3. The left plot shows the flux spectrum of the ν_μ. The bold, solid curve is the sample 1 depicted in Fig. 8.3. The thin solid curves are the result for the samples 2, 3, 4, and 5. The 66 burst spectra have been rescaled to 10000 burst obtain a quasi-diffuse flux limit. Therefore, we have included the high statistics result as the bold, dashed curve. Due to the low number of bursts there is high variation among the low statistics samples, especially on the derived flux limit. However, the flux shape is unaffected by the low statistics. The right plot shows the flavor ratio R for sample 1 (thick, solid curve), which is chosen as representative for the low statistics samples. The thick, dashed curve is the flavor ratio for a single burst, while the thin, solid line is the result for the high statistics. As one can see from comparing the thin, solid and the thick, solid curves, there is nearly no difference in the flavor ratio between the high and the low statistics result.

gain insight on the distribution of Γ. The information from stacking analysis is very useful in this context, even though no precise diffuse flux estimation can be obtained from it.

The third sample is the redshift z. For the low statistics sample we again use the star formation rate by Hopkins and Beacom as stated in Eq. (4.4) including the correctional factor $\mathcal{E}(z)$ for evolution with redshift. As for the Lorentz factor we generate five 66 burst samples. The seeds for the sets can be found in the Appendix E. The representative sample 1 is displayed in the histogram on linear scale with a bin size of 0.1 together with the relative contribution from a redshift, see Fig. 8.5. Note that the number of bursts with high contribution is low, with the highest contributions (lowest redshifts) missing in the sample. There are only two bursts in this 66 burst sample with $z \leq 1$, and only eight with $z \leq 1.4$.

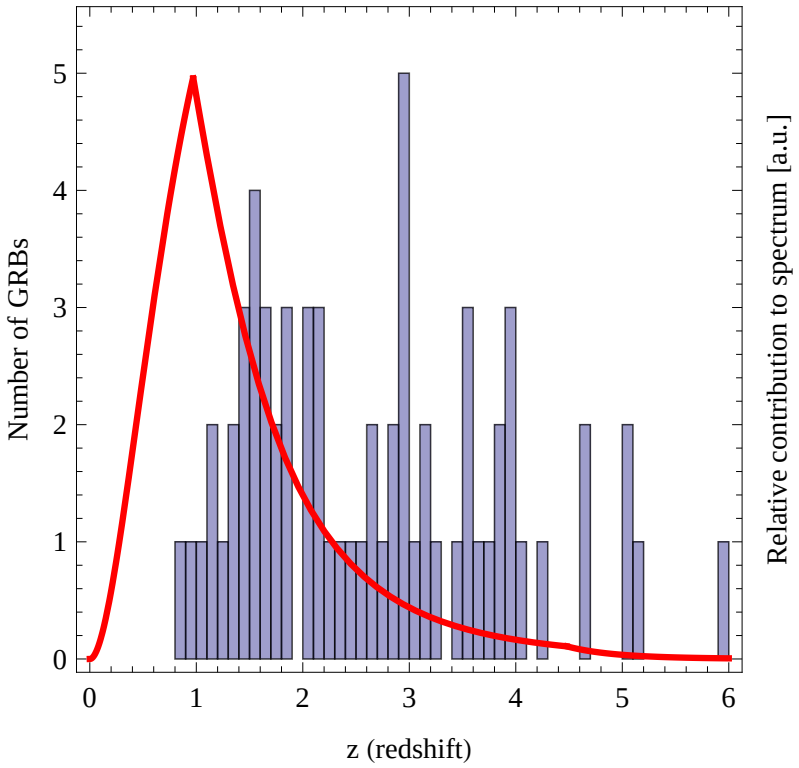

Figure 8.5: Distribution of the 66 bursts of sample 1 following the distribution described by Eq. (4.4). Sample 1 is one example of the five simulated distributions. Since there are no qualitative differences among the sample, we only include this one example. Furthermore, the thick red curve shows the contribution of all bursts up the corresponding z. By comparison of both contributions one can see that there are only two bursts at $z \leq 1$, which is considered to be the dominant region as discussed in section 7.2.

We use the five samples of 66 bursts with different redshifts z to calculate the spectral flux of the ν_μ after flavor mixing individually. We then add the 66 burst spectra and use linear extrapolation to gain a 10000 burst limit. As a consequence of the low number of low redshift GRBs, the extrapolated "10000 burst" result of sample 1 (solid, bold curve) is significantly lower compared to the high statistics sample (dashed, bold curve) from section 7.2, see left plot of Fig. 8.6. This observation is also correct for the four other 66 burst samples (solid, thin curves). Only one curve is nearly at the same level as the high statistics sample. However, if such a near burst (with all the assumptions and implications discussed in section 7.2) would by chance be observed in such a small sample, the result could also be higher compared to the high statistics sample. Nevertheless, this shows that the uncertainty on the diffuse flux from stacking analysis is high. And, maybe more importantly, that the low burst limit looks significantly different from the high burst limit, which could

also be obtained by Monte Carlo integration. Therefore, for low statistics, as can be expected for GRB neutrinos, it is mandatory to use Monte Carlo sampling, as Monte Carlo integration cannot produce any low statistics results. However, as for the Lorentz factor, the effect of the low statistics on the flux shape is small. All features of the single burst are visible. Moreover, as one can see from the right plot of Fig. 8.6, the flavor ratio is also just slightly affected. Depicted in Fig. 8.6 are the flavor ratio for sample 1 (bold, solid curve), as representative for the five 66 burst samples, the high statistics sample (thin, solid curve), and the single source flavor ratio (bold, dashed curve). Due to the lack of low z bursts, the transition from "pion beam" to "muon damped" is slightly shifted to lower energies, when one compares the low to the high statistics result. Still, the flavor ratio is very robust. Therefore, we can, as for the Lorentz factor before, gain insight on the flux shape and the flavor ratio from stacking analysis. However, the result of the flux limit from these analysis has significant uncertainties.

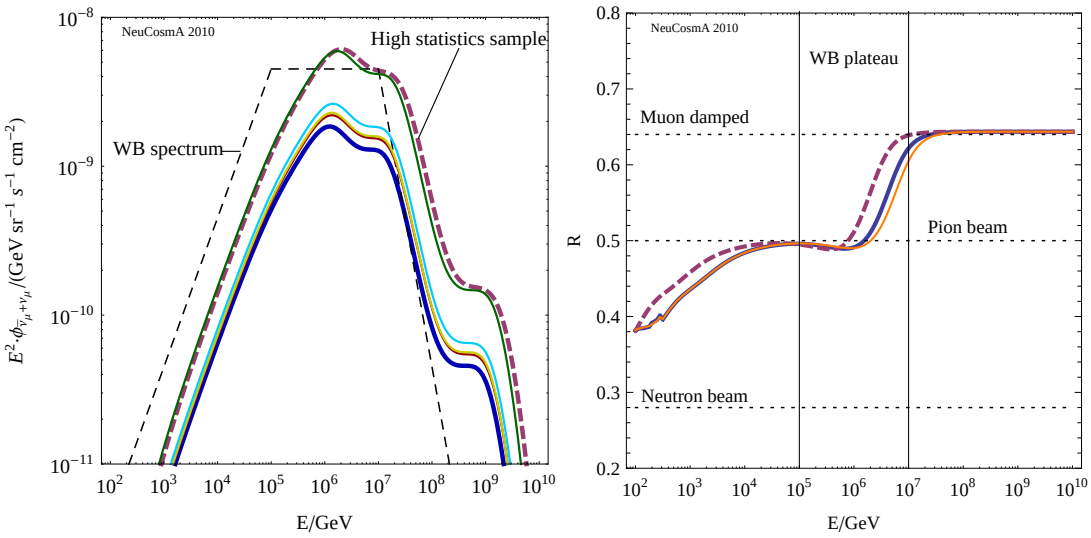

Figure 8.6: The muon neutrino flux obtained from the 66 burst samples (left plot). The bold, solid curve represents sample 1, which is depicted in Fig. 8.5. The four thin, solid curves are the four additional 66 burst samples. These flux results are obtained by extrapolating from 66 bursts up to 10000. They are in general lower than the high statistics result (bold, dashed curve), due to the lack of low redshift bursts. However, the flux shape is unchanged by low statistics. In case of the flavor ratio R similar reasoning applies. The bold, solid curve in the right plot depicts the flavor ratio for sample 1. The thin, solid line is the ratio for the high statistics sample. And, the bold, dashed curve is the flavor ratio for the single burst. The transition from a mixed source between "neutron beam" and "pion beam" to "pion beam" to "muon damped" source does not change in shape but is shifted to slightly lower energies compared to the high statistics result, as shown in the right plot. The kink at $E \approx 10^{2.5}$ GeV is due to low statistics in that energy range.

9. Discussion and Summary

This diploma project was centered around the simulation of diffuse neutrino fluxes from cosmic accelerators. The simulation of these was done for the special case of gamma-ray bursts. In the progress of this diploma thesis we first extended the new NeuCosmA code with features such as relativistic beaming, energy loss through cosmological redshift and flavor mixing of neutrinos. With the help of this extended code we were able to reproduce the often cited WB flux shape (proportional to energy till first break at $\approx 10^5\,\mathrm{GeV}$, then flat plateau till $10^7\,\mathrm{GeV}$, spectrum decays $\propto E^{-2}$ in $E^2\phi(E)$) by calculating the result of photohadronic interactions. For this reproduction the photohadronic interactions were modeled using the Δ-resonance approximation as used by Waxman and Bahcall. All calculations were done by assuming fixed photon and proton spectra, which were derived from observational data. The main goal was to successfully reproduce the WB flux shape. Therefore, we needed to use the same assumptions, including the same spectra, as Waxman and Bahcall did. We showed that the spectral features can be reproduced in a multi-step process including input from particle physics and astrophysics. The breaks in the spectra can be traced back to the break in the photon spectrum (lower break) and to synchrotron losses of the intermediate pions (upper break). From this starting point we derived parameter sets consisting of the Lorentz factor Γ, the redshift z, the magnetic field B, and the break energy of the photon spectrum $\varepsilon'_{\gamma,\mathrm{break}}$. Our calculations showed that the specific WB shape can be reproduced with a multitude of parameter sets. The two parameter sets shown in Table 6.1 are just two examples of reasonable solutions. The parameters have internal connections when one assumes the flux shape to be fixed. We then switched on other production channels from photo hadronic interactions. We showed how this affects the spectrum and how the shape is perturbed. In the next step we took flavor mixing into account leading to a new flux shape. After each step the spectra had to be renormalized to conserve energy. The resulting flux shape has a characteristic double peak from pions and muons and a further contribution at high energies from kaon decays. However, the parameters obtained from observations do not always match our parameter sets. The magnetic fields in GRBs currently cannot be probed by measurements. The

Lorentz factor can only be estimated, and some observations indicate that higher Lorentz factors than $\Gamma \sim 300$ should be assumed for most bursts. And, the observed spectral breaks are lower than the ones we obtain from the calculation of the lower break. Moreover, spectral data from the current *Fermi*/GBM observations indicate that for long gamma-ray bursts the lower photon spectral index is $\alpha_\gamma = 0.90 \pm 0.36$, taken from Ref. [57]. And, that the light curves should not be fitted with a Band function.

We discussed the effect of distribution of parameters at the example of the Lorentz factor Γ, the redshift z and the magnetic field B. For the first two parameters we could model observational data. We incorporated several known distributions as well as proposing an analytic distribution ourselves in case of Γ. As already theoretical considerations show the flux of a burst strongly depends on these two parameters. From the simulation of 10000 bursts each with parameters distributed according to the measured distributions we could obtain a (quasi-)diffuse flux. The parameter values were picked with Monte Carlo sampling. By this we could show that the diffuse flux is dominated by bursts with parameters which differ significantly from the "standard" values. For our distribution of Γ bursts with $\Gamma = 774$ contributed the most to the total diffuse flux. For the redshift bursts with $z = 0.97$ dominated in case of the star formation history by Hopkins and Beacom (with correction function). The magnetic field B affected only on the shape of the diffuse flux spectra and not the contribution of a single burst. The problem with the magnetic field was mainly the uncertainties. There was (and still is) no accepted distribution of the magnetic field among the bursts and there are only ranges for possibly viable values. Hence, we used some academic example distributions to quantify the effect. The result was that the features were smeared out. The degree of the smearing depended on the chosen distribution. In particular, in case of fewer bursts we showed that this can be problematic. In a low statistics sample we only considered 300 bursts for the magnetic field. For the samples of B the smearing effect got even stronger, obscuring all features of the single burst. Therefore, the information on the magnetic field from stacking analysis may be limited. Moreover, we also plotted 66 burst samples for the Lorentz factor Γ and the redshift z. This number of bursts is of the order of recent analysis, see Ref. [70]. We showed that the flux shape and the flavor ratio can already be obtained from such a small sample. However, the extrapolation of a diffuse flux limit from such a low number of bursts is highly limited by statistical uncertainties.

The flux levels estimated in this thesis were taken from ideal assumptions by Waxman and Bahcall. Even with those assumptions it will need roughly 10 years of data taking from IceCube to, in the best case, detect this diffuse flux. Unfortunately, it is more realistic that the diffuse flux from GRB is lower than the WB GRB limit by more than one order of magnitude. Some single bright bursts may be detected nonetheless. Also, the kaon component opens a new window of opportunity to maybe detect GRB neutrinos with extensive air shower imaging, *e.g.* with measurements from Auger. The next years will set new bounds on the diffuse flux of neutrinos. Even a non-detection will help refine the current bounds.

10. Outlook and open issues

Even though we have already taken a look at some parameters not all have been studied yet. We will be examining next the effect of different input spectra with different spectral indices. In particular, the effect of the included photon spectra still needs to be discussed in more detail. First of all, our choice of spectral indices of the Band function in Eq. (4.8) is only the averaged values. Real spectra mostly have different indices compared to our standard values, see Ref. [57] for current *Fermi*/GBM results. This will again alter the shape of the neutrino spectra, however, it is easily included into our code. Furthermore, we still need to take a closer look at the internal connections of the parameters in the internal shock model. As stated in chapter 7 varying one parameter nearly always also changes other parameters. This has to be examined carefully. So far, observational correlations, *e.g.* the Amati relation , see Ref. [94], or the Yonetoku relation, Ref. [91], are not included in our model. However, it might be possible to derive these relations with help of the internal connections of the source engine. Moreover, we still want to calculate the probability to observe a very favorable burst, *i.e.* low z, high Γ. On the other hand the Band function does not necessarily describe the observed photon spectra of a GRB. Since it is possible to calculate interpolating functions from datasets in our software we could take the measured GRB photon spectra and use these for calculations. This would omit the step of fitting the Band function to the measured photon spectra and would reduce the uncertainty on the result. This kind of direct calculation could be interesting for the search of GRB signals with a neutrino telescope. Moreover, with the first comprehensive analyses for *Fermi* data being published, we might also gain new information on the parameters of the burst in the near future. These developments considered and, maybe, give even new distributions for our diffuse flux simulations.

Another possible extension of this study could be achieved by adding the *pp* interactions into the NeuCosmA code. Since our current version totally neglects these kinds of interactions they will alter the shape. It would be interesting to see if these changes would be negligible or if they change the spectral shape significantly. As far

as GRB go an inclusion of these interactions could soften the requirement of neutron transparency. Since the code also calculates the production of photons the inclusion of these *pp* interactions could lead to (or at least be a next step) a self consistent model for GRB.

Bibliography

[1] W. Pauli, Phys. Today **31N9**, 27 (1978).

[2] E. Fermi, Zeitschrift für Physik A Hadrons and Nuclei **88**, 161 (1934), 10.1007/BF01351864.

[3] C. L. Cowan, F. Reines, F. B. Harrison, H. W. Kruse, and A. D. McGuire, Science **124**, 103 (1956), http://www.sciencemag.org/content/124/3212/103.full.pdf.

[4] K. Kodama *et al.*, Physics Letters B **504**, 218 (2001).

[5] K. Nakamura and P. D. Group, Journal of Physics G: Nuclear and Particle Physics **37**, 075021 (2010).

[6] K. Hirata *et al.*, Phys. Rev. Lett. **58**, 1490 (1987).

[7] R. Davis, Phys. Rev. Lett. **12**, 303 (1964).

[8] R. Davis, D. S. Harmer, and K. C. Hoffman, Phys. Rev. Lett. **20**, 1205 (1968).

[9] KM3NeT, C. Distefano, Nucl. Phys. Proc. Suppl. **190**, 115 (2009).

[10] V. Popa, Nuclear Instruments and Methods in Physics Research Section A: Accelerators, Spectrometers, Detectors and Associated Equipment **In Press, Corrected Proof**, "KM3NeT: Present status and potentiality for the search for exotic particles" (2010).

[11] IceCube, J. Ahrens *et al.*, Nucl. Phys. Proc. Suppl. **118**, 388 (2003), astro-ph/0209556.

[12] A. Einstein, Ann. Phys. **322**, 891 (1905).

[13] A. Einstein, Ann. Phys. **354**, 769 (1916).

[14] M. J. Rees, Nature **211**, 468 (1966).

[15] G. B. Rybicki and A. P. Lightman, *Radiative Processes in Astrophysics* (Wiley-VCH, 1985).

[16] E. Hubble, Proceedings of the National Academy of Science **15**, 168 (1929).

[17] A. Weigert, H. J. Wendker, and L. Wisotzki, *Astronomie und Astrophysik: Ein Grundkurs* (Wiley-VCH, 2009).

[18] E. Komatsu *et al.*, (2010), arXiv:1001.4538.

[19] T. K. Gaisser, *Cosmic Rays and Particle Physics* (Cambridge University Press, 1991).

[20] S. Hümmer, M. Maltoni, W. Winter, and C. Yaguna, Astropart. Phys. **34**, 205 (2010), arXiv:1007.0006.

[21] A. M. Hopkins and J. F. Beacom, Astrophys. J. **651**, 142 (2006), arXiv:astro-ph/0601463.

[22] A. Einstein, Ann. Phys. **322**, 132 (1905).

[23] J. G. Learned and K. Mannheim, Ann. Rev. Nucl. Part. Sci. **50**, 679 (2000).

[24] J. K. Becker, Phys. Rept. **458**, 173 (2008), arXiv:0710.1557.

[25] E. Waxman and J. N. Bahcall, Phys. Rev. Lett. **78**, 2292 (1997), arXiv:astro-ph/9701231.

[26] K. Mannheim, R. J. Protheroe, and J. P. Rachen, Phys. Rev. **D63**, 023003 (2001), arXiv:astro-ph/9812398.

[27] HiRes, R. U. Abbasi *et al.*, Phys. Rev. Lett. **100**, 101101 (2008), arXiv:astro-ph/0703099.

[28] Pierre Auger, J. Abraham *et al.*, Phys. Rev. Lett. **101**, 061101 (2008), arXiv:0806.4302.

[29] S. Hümmer, M. Rüger, F. Spanier, and W. Winter, Astrophys. J. **721**, 630 (2010), arXiv:1002.1310.

[30] D. Guetta, D. Hooper, J. Alvarez-Muniz, F. Halzen, and E. Reuveni, Astropart. Phys. **20**, 429 (2004), arXiv:astro-ph/0302524.

[31] P. Lipari, M. Lusignoli, and D. Meloni, Phys. Rev. **D75**, 123005 (2007), arXiv:0704.0718.

[32] C. Giunti and C. W. Kim, Found. Phys. Lett. **14**, 213 (2001), arXiv:hep-ph/0011074.

[33] Particle Data Group, C. Amsler *et al.*, Phys. Lett. **B667**, 1 (2008).

[34] T. Schwetz, M. A. Tortola, and J. W. F. Valle, New J. Phys. **10**, 113011 (2008), arXiv:0808.2016.

[35] M. Maltoni and W. Winter, JHEP **07**, 064 (2008), arXiv:0803.2050.

[36] IceCube, J. Dumm and H. Landsman, J. Phys. Conf. Ser. **60**, 334 (2007).

[37] ANTARES, J. Aguilar *et al.*, (2010), arXiv:1011.3772.

[38] J. F. Beacom, N. F. Bell, D. Hooper, S. Pakvasa, and T. J. Weiler, Phys. Rev. **D68**, 093005 (2003), arXiv:hep-ph/0307025.

[39] W. Winter, Nucl. Phys. Proc. Suppl. **203-204**, 45 (2010), arXiv:1004.4160.

[40] P. D. Serpico and M. Kachelriess, Phys. Rev. Lett. **94**, 211102 (2005), arXiv:hep-ph/0502088.

[41] S. Pakvasa, Mod. Phys. Lett. **A23**, 1313 (2008), arXiv:0803.1701.

[42] T. Karg and f. t. I. Collaboration, (2010), arXiv:1011.5027.

[43] R. W. Klebesadel, I. B. Strong, and R. A. Olson, ApJL **182**, L85+ (1973).

[44] M. Ruderman, Theories of gamma-ray bursts, in *Seventh Texas Symposium on Relativistic Astrophysics*, edited by P. G. Bergman, E. J. Fenyves, & L. Motz, , Annals of the New York Academy of Sciences Vol. 262, pp. 164–180, 1975.

[45] G. J. Fishman and C. A. Meegan, Annual Review of Astronomy and Astrophysics **33**, 415 (1995).

[46] E. E. Fenimore *et al.*, Nature **366**, 40 (1993).

[47] T. Piran, Rev. Mod. Phys. **76**, 1143 (2004), arXiv:astro-ph/0405503.

[48] P. Meszaros, Rept. Prog. Phys. **69**, 2259 (2006), arXiv:astro-ph/0605208.

[49] E. Costa *et al.*, Nature **387**, 783 (1997), arXiv:astro-ph/9706065.

[50] J. van Paradijs *et al.*, Nature **386**, 686 (1997).

[51] M. R. Metzger *et al.*, Nature **387**, 878 (1997).

[52] S. R. Kulkarni *et al.*, Nature **393**, 35 (1998).

[53] J. Hjorth *et al.*, Nature **423**, 847 (2003), arXiv:astro-ph/0306347.

[54] K. Z. Stanek *et al.*, ApJL **591**, L17 (2003), arXiv:astro-ph/0304173.

[55] S. D. Barthelmy *et al.*, Space Science Reviews **120**, 143 (2005).

[56] http://fermi.gsfc.nasa.gov/.

[57] L. Nava, G. Ghirlanda, G. Ghisellini, and A. Celotti, (2010), arXiv:1012.2863.

[58] A. I. MacFadyen and S. E. Woosley, Astrophys. J. **524**, 262 (1999), arXiv:astro-ph/9810274.

[59] S. E. Woosley, Astrophys. J. **405**, 273 (1993).

[60] D. Eichler, M. Livio, T. Piran, and D. N. Schramm, Nature **340**, 126 (1989).

[61] R. Narayan, B. Paczynski, and T. Piran, ApJL **395**, L83 (1992), arXiv:astro-ph/9204001.

[62] R. Sari and T. Piran, Astrophys. J. **485**, 270 (1997), arXiv:astro-ph/9701002.

[63] S. Kobayashi, T. Piran, and R. Sari, Astrophys. J. **490**, 92 (1997), arXiv:astro-ph/9705013.

[64] M. J. Rees and P. Meszaros, Astrophys. J. **430**, L93 (1994), arXiv:astro-ph/9404038.

[65] F. Halzen, (1998), arXiv:astro-ph/9810368.

[66] J. K. Becker, M. Stamatikos, F. Halzen, and W. Rhode, Astropart. Phys. **25**, 118 (2006), arXiv:astro-ph/0511785.

[67] Y. Lithwick and R. Sari, Astrophys. J. **555**, 540 (2001), arXiv:astro-ph/0011508.

[68] S. Razzaque, P. Meszaros, and B. Zhang, Astrophys. J. **613**, 1072 (2004), arXiv:astro-ph/0404076.

[69] I. K. Baldry and K. Glazebrook, Astrophys. J. **593**, 258 (2003), arXiv:astro-ph/0304423.

[70] M. D. Kistler, H. Yüksel, J. F. Beacom, A. M. Hopkins, and J. S. B. Wyithe, Astrophys. J. **705**, L104 (2009), arXiv:0906.0590.

[71] K. Murase and S. Nagataki, Phys. Rev. **D73**, 063002 (2006), arXiv:astro-ph/0512275.

[72] E. Waxman, Nucl. Phys. Proc. Suppl. **118**, 353 (2003), arXiv:astro-ph/0211358.

[73] D. Band *et al.*, Astrophys. J. **413**, 281 (1993).

[74] IceCube, R. Abbasi *et al.*, Astrophys. J. **710**, 346 (2010), arXiv:0907.2227.

[75] A. Mücke, R. Engel, J. P. Rachen, R. J. Protheroe, and T. Stanev, Comput. Phys. Commun. **124**, 290 (2000), arXiv:astro-ph/9903478.

[76] A. M. Hillas, Ann. Rev. Astron. Astrophys. **22**, 425 (1984).

[77] S. R. Kelner and F. A. Aharonian, Phys. Rev. **D78**, 034013 (2008), arXiv:0803.0688.

[78] A. M. Atoyan and C. D. Dermer, Astrophys. J. **586**, 79 (2003), arXiv:astro-ph/0209231.

[79] M. Matsumoto and T. Nishimura, ACM Trans. Model. Comput. Simul. **8**, 3 (1998).

[80] D. Wanderman and T. Piran, Mon. Not. Roy. Astron. Soc. **406**, 1944 (2010), arXiv:0912.0709.

[81] S. Razzaque, C. D. Dermer, and J. D. Finke, Open Astron. J. **3**, 150 (2010), arXiv:0908.0513.

[82] T. F. LAT and F. G. Collaborations, Science **323**, 1688 (2009), http://www.sciencemag.org/content/323/5922/1688.full.pdf.

[83] E. Waxman and J. N. Bahcall, Phys. Rev. **D59**, 023002 (1999), arXiv:hep-ph/9807282.

[84] P. Huber, M. Lindner, T. Schwetz, and W. Winter, JHEP **11**, 044 (2009), arXiv:0907.1896.

[85] P. Huber and W. Winter, Phys. Rev. **D68**, 037301 (2003), arXiv:hep-ph/0301257.

[86] J. Tang and W. Winter, Phys. Rev. **D80**, 053001 (2009), arXiv:0903.3039.

[87] K. Murase and K. Ioka, Astrophys. J. **676**, 1123 (2008), arXiv:0708.1370.

[88] E. Molinari *et al.*, Astronomy and Astrophysics **469**, L13 (2007), arXiv:astro-ph/0612607.

[89] N. Gupta and B. Zhang, Astropart. Phys. **27**, 386 (2007), arXiv:astro-ph/0606744.

[90] J. Alvarez-Muniz, F. Halzen, and D. W. Hooper, Phys. Rev. **D62**, 093015 (2000), arXiv:astro-ph/0006027.

[91] D. Yonetoku *et al.*, Astrophys. J. **609**, 935 (2003), arXiv:astro-ph/0309217.

[92] K. S. Cheng, Y.-W. Yu, and T. Harko, Phys. Rev. Lett. **104**, 241102 (2010), arXiv:1005.3427.

[93] C. Porciani and P. Madau, Astrophys. J. **548**, 522 (2001), arXiv:astro-ph/0008294.

[94] L. Amati *et al.*, Astron. Astrophys. **390**, 81 (2002), arXiv:astro-ph/0205230.

A. The effect of the input and further control parameters

In this chapter we discuss the effect of what we call input and further control parameters. So far, these parameters have been set to a certain value without explaining their function. We will now give a short overview of how these parameters effect the spectra and why these small changes do not affect the spectrum significantly. We will discuss the acceleration efficiency η, the minimal proton energy $\varepsilon_{p,\mathrm{min}}$, the minimal photon energy $\varepsilon_{\gamma,\mathrm{min}}$ and the maximal photon energy $\varepsilon_{\gamma,\mathrm{max}}$.

A.1. Acceleration efficiency

Another parameter of our model which so far has not been discussed is the acceleration efficiency η. So far we have adapted a value of $\eta = 0.1$ for our calculations. This selection was done relatively arbitrarily. To justify this decision as well as showing the effect of η we calculated the spectra of ν_e and ν_μ after oscillation. As can be seen in Fig. A.1 the changed cut-off energy $\varepsilon^{'}_{p,\mathrm{max}}$ affects the high energy part of the spectra. Features such as the peak from kaons are more pronounced for a higher acceleration efficiency. The spectral shape stay unperturbed from this change. Also this constrain on the maximum proton energy does not allow for a dominance of the $\bar{\nu}_e$ from n-decays at high energies, see Fig. 6.3.

We also looked into the effect the maximal proton energy $\varepsilon^{'}_{p,\mathrm{max}}$ (in the source rest frame) has on the muon neutrino flux spectra from π^+-decay, especially on the high energy processes (labeled "Multi π" in Fig. 6.2). We inserted $\varepsilon^{'}_{p,\mathrm{max}}$ manually simulating spectra with 10^6, 10^7, 10^8, 10^9 and 10^{10} GeV. The solid curves are obtained from the full photohadronic interaction cross section while the solid curves are without the high energy ("Multi π") events, see Fig. A.2. As can be seen in Fig. A.2 a lower $\varepsilon^{'}_{p,\mathrm{max}}$ leads to earlier breaks in the neutrino spectra which is clearly visible for 10^6 and 10^7 GeV due to the change of shape, visible for 10^8 GeV (steeper drop-off), while the curves for 10^9 and 10^{10} GeV are hardly distinguishable. None

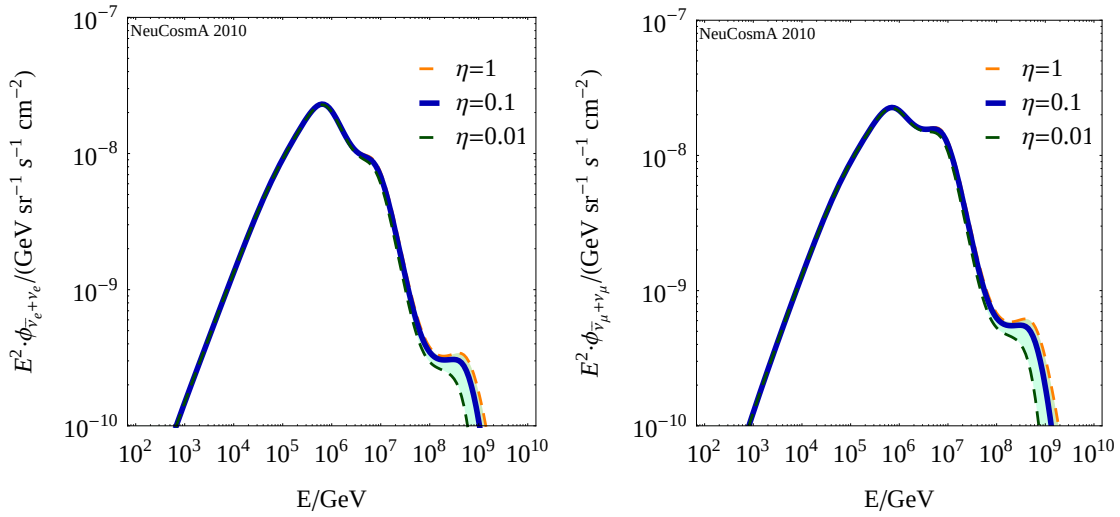

Figure A.1: These plots show the effect of the acceleration efficiency η (which effects the cut-off energy $\varepsilon'_{p,\max}$). At high energies the spectra are higher for higher η while at low energies the effect is negligible.

the less even for the last two the premise of a cut at lower energy (or a stronger break) still holds. The normalization is the same as in Fig. 6.2.

A.2. Minimal proton energy

The minimal proton energy $E_{p,\min}$ was set to 1 GeV due to estimations of the threshold energy. This value of $E_{p,\min}$ is considered our "standard value" of $E_{p,\min}$. The main goal was to choose a value that was far enough away from the threshold to suppress effects of this parameter. In Fig. A.3 we plot the spectra of the electron and muon neutrinos after oscillation at the detector for our standard value (thick curve) and for a value 4 orders of magnitude larger (thin curve). As can be expected a higher $E_{p,\min}$ leads to lower neutrino fluxes at low energies. To emphasize the effect the area between the two spectra was shaded. Calculations for a value of $E_{p,\min}$ which was four orders of magnitude smaller did not show any deviation from the standard spectrum and are therefore not depicted additionally.

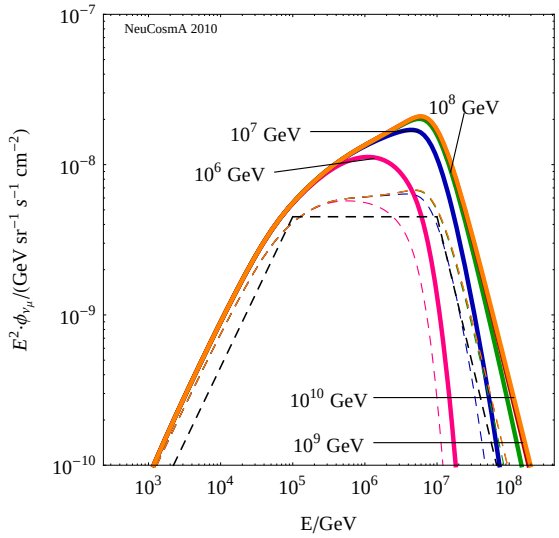

Figure A.2: These curves show the effect of the maximal proton energy $\varepsilon'_{p,\max}$ on the muon neutrino spectra from π^+-decay. The solid curves are for the full photohadronic cross section, while the dashed lines represent the neutrino production without high energy ("Multi π" in Fig. 6.2) processes. The plot shows spectra for $\varepsilon'_{p,\max} = 10^6$, 10^7, 10^8, 10^9 and 10^{10} GeV. The curves for 10^9 and 10^{10} GeV are hardly distinguishable.

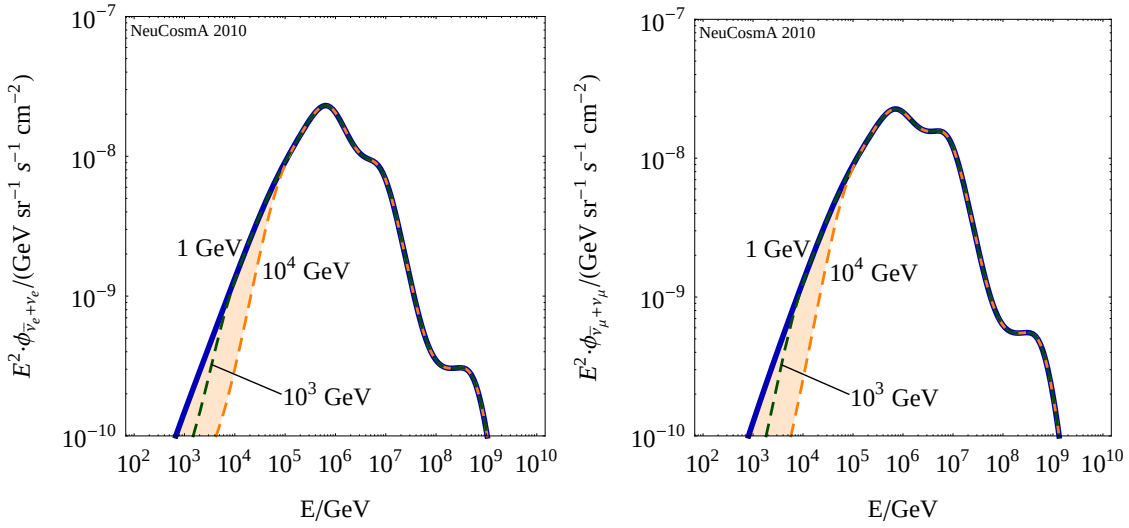

Figure A.3: In these figures the effect of $E_{p,\min}$ is depicted. The labels show the value of $E_{p,\min}$ for the appropriate curve. Due to the proportionality $E_\nu \propto E_p$ the effect of $E_{p,\min}$ is to the lower energy part of the spectrum. As expected a higher maximal proton energy leads to lower levels of neutrinos in these energy regions.

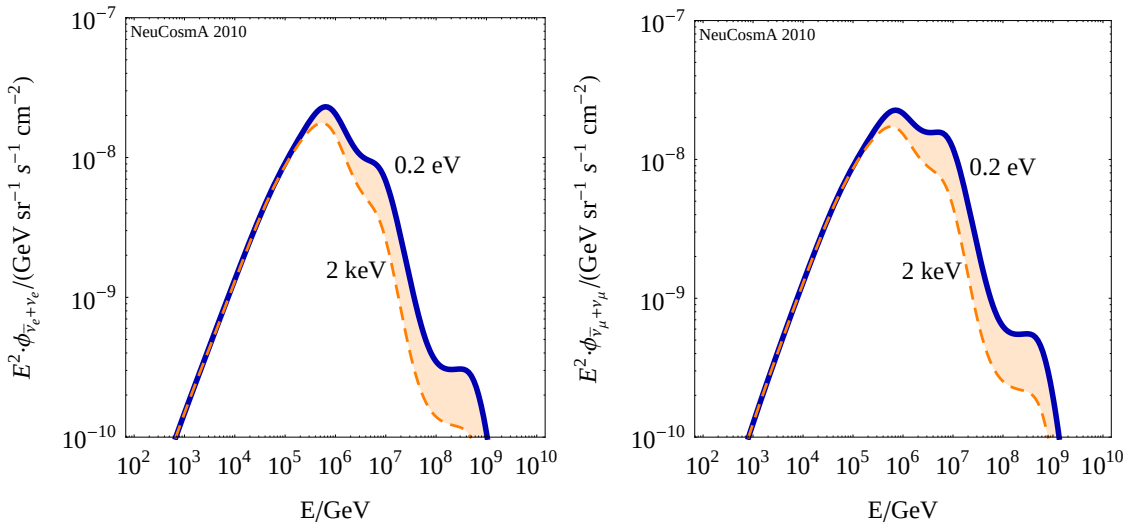

Figure A.4: In these figures the effect of $E_{\gamma,\min}$ is depicted. The labels show the value of $E_{\gamma,\min}$ for the appropriate curve. As can be seen above a higher value of $E_{\gamma,\min}$ leads to a suppression of the neutrino flux at energies above 10^5 GeV.

A.3. Minimal photon energy

As another parameter the minimal photon energy $E_{\gamma,\min}$ was set to 0.2 eV without further explanation. Again the threshold energy of the photohadronic interactions was the energy reference taken into account for this decision. But opposite to the effect of $E_{p,\min}$ which directly affects the low energy regime $E_{\gamma,\min}$ has an effect on the highest energy neutrinos as can be derived from Eq. (4.12). As can be seen in Fig. A.4 a $E_{\gamma,\min}$ that is four orders of magnitude larger than our standard value leads to a suppression of the produced neutrinos above $\approx 10^5$ GeV. To emphasize this deviation the area between the standard spectrum and the one with large $E_{\gamma,\min}$ has been shaded. The curves have been labeled in Fig. A.4 by the values of $E_{\gamma,\min}$.

A.4. Maximum photon energy

The maximum photon energy $E_{\gamma,\max}$ was chosen to be a multiple of $\varepsilon_{\gamma,\text{break}}$. For our standard spectrum in Fig. 6.1 we chose a value of 300. As explained earlier the choice of $E_{\gamma,\max}$ affects the "zeroth" break of the neutrino spectrum. This break is obtained by inserting $E_{\gamma,\max}$ into Eq. (4.12). By simple evaluation of the formula one obtains a value for the zeroth break at $\sim 10^{2.5}$ GeV (for $E_{\gamma,\max} = 300 \cdot \varepsilon_{\gamma,\text{break}}$.

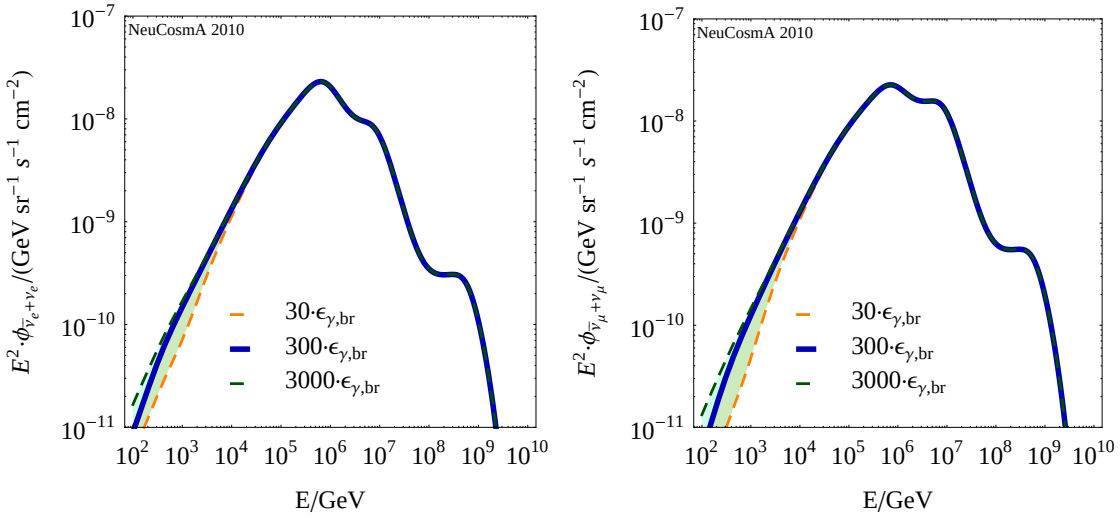

Figure A.5: The effect of $E_{\gamma,\mathrm{max}}$ for the values 30, 300 (standard) and 3000 in multiples of $\varepsilon_{\gamma,\mathrm{break}}$. A higher $E_{\gamma,\mathrm{max}}$ leads to a lower "zeroth" break.

B. The full transition probabilities

On the next page we have given the full analytic formulas for the transition probabilities as defined in Eq. (3.10). The transition probability $P_{\tau\tau}$ is not included since none of the considered decay processes results in the production of a τ or a ν_τ, see Eqs. (3.3) to (3.6).

$$
\begin{aligned}
P_{ee} &= \cos^4\theta_{12}\,\cos^4\theta_{13} + \sin^4\theta_{12}\,\cos^4\theta_{13} + \sin^4\theta_{13} && \text{(B.1)}\\
P_{e\mu} &= \cos^2\theta_{12}\,\cos^2\theta_{13}\cdot\left(\sin^2\theta_{12}\,\cos^2\theta_{23} + \sin\theta_{12}\,\cos\theta_{23}\,\cos\theta_{12}\,\sin\theta_{23}\,\sin\theta_{13}\cdot 2\,\cos\delta + \cos^2\theta_{12}\,\sin^2\theta_{23}\,\sin^2\theta_{13}\right)\\
&\quad + \sin^2\theta_{12}\,\cos^2_{13}\cdot\left(\cos^2\theta_{12}\,\cos^2\theta_{23} - \cos\theta_{12}\,\cos\theta_{23}\sin\theta_{12}\,\sin\theta_{23}\,\sin\theta_{13}\cdot 2\,\cos\delta + \sin^2\theta_{12}\,\sin^2\theta_{23}\,\sin^2\theta_{13}\right)\\
&\quad + \sin^2\theta_{13}\,\sin^2\theta_{23}\,\cos^2\theta_{13} && \text{(B.2)}\\
P_{e\tau} &= \cos^2\theta_{12}\,\cos^2\theta_{13}\cdot\left(\sin^2\theta_{12}\,\sin^2\theta_{23} - \sin\theta_{12}\,\sin\theta_{23}\,\cos\theta_{12}\,\cos\theta_{23}\,\sin\theta_{13}\cdot 2\,\cos\delta + \cos^2\theta_{12}\,\cos^2\theta_{23}\,\sin^2\theta_{13}\right)\\
&\quad + \sin^2\theta_{12}\,\cos^2_{13}\cdot\left(\cos^2\theta_{12}\,\sin^2\theta_{23} + \cos\theta_{12}\,\sin\theta_{23}\sin\theta_{12}\,\cos\theta_{23}\,\sin\theta_{13}\cdot 2\,\cos\delta + \sin^2\theta_{12}\,\cos^2\theta_{23}\,\sin^2\theta_{13}\right)\\
&\quad + \sin^2\theta_{13}\,\cos^2\theta_{23}\,\cos^2\theta_{13} && \text{(B.3)}\\
P_{\mu\mu} &= \left(\sin^2\theta_{12}\,\cos^2\theta_{23} + \sin\theta_{12}\,\cos\theta_{23}\,\cos\theta_{12}\,\sin\theta_{23}\,\sin\theta_{13}\cdot 2\,\cos\delta + \cos^2\theta_{12}\,\sin^2\theta_{23}\sin^2\theta_{13}\right)^2\\
&\quad + \left(\cos^2\theta_{12}\,\cos^2\theta_{23} - \cos\theta_{12}\,\cos\theta_{23}\,\sin\theta_{12}\,\sin\theta_{23}\,\sin\theta_{13}\cdot 2\,\cos\delta + \sin^2\theta_{12}\,\sin^2\theta_{23}\,\sin^2_{13}\right)^2\\
&\quad + \sin^4\theta_{23}\,\cos^4\theta_{13} && \text{(B.4)}\\
P_{\mu\tau} &= \left(\sin^2\theta_{12}\,\cos^2\theta_{23} + \sin\theta_{12}\,\cos\theta_{23}\,\cos\theta_{12}\,\sin\theta_{23}\,\sin\theta_{13}\cdot 2\,\cos\delta + \cos^2\theta_{12}\,\sin^2\theta_{23}\sin^2\theta_{13}\right)\\
&\quad\cdot\left(\sin^2\theta_{12}\,\sin^2\theta_{23} - \sin\theta_{12}\,\sin\theta_{23}\,\cos\theta_{12}\,\cos\theta_{23}\,\sin\theta_{13}\cdot 2\,\cos\delta + \cos^2\theta_{12}\cos^2\theta_{23}\,\sin^2\theta_{13}\right)\\
&\quad + \left(\cos^2\theta_{12}\,\cos^2\theta_{23} - \cos\theta_{12}\,\cos\theta_{23}\,\sin\theta_{12}\,\sin\theta_{23}\,\sin\theta_{13}\cdot 2\,\cos\delta + \sin^2\theta_{12}\,\sin^2\theta_{23}\,\sin^2_{13}\right)\\
&\quad\cdot\left(\cos^2\theta_{12}\,\sin^2\theta_{23} + \cos\theta_{12}\,\sin\theta_{23}\,\sin\theta_{12}\,\cos\theta_{23}\,\sin\theta_{13}\cdot 2\,\cos\delta + \sin^2\theta_{12}\,\cos^2\theta_{23}\,\sin^2\theta_{13}\right)\\
&\quad + \sin^2\theta_{23}\,\cos^4\theta_{13}\,\cos^2\theta_{23} && \text{(B.5)}
\end{aligned}
$$

C. Classes of neutrino sources

The classification of neutrino sources, taken from Ref. [20]:

Pion beams

Neutrinos are produced by charged pion decays in the ratio $\nu_e : \nu_\mu : \nu_\tau$ of $1 : 2 : 0$ (neutrinos and antineutrinos added). This means that the electron to muon neutrino ratio $R_e = (Q_{\nu_e} + Q_{\bar{\nu}_e}) \,/\, \left(Q_{\nu_\mu} + Q_{\bar{\nu}_\mu}\right) \simeq 1/2$ (corresponds to $R = 0.5$ for our flavor ratio R after flavor mixing, taken from Eq. (3.12)). In fact, corrections from the helicity dependence of the muon decays lead to small deviations from this ratio, which, however, can be understood in terms of particle physics, as well as there can be pile-up effects. The deviations depend on the input particle spectra and are below the level of 10% in Re. They are fully taken into account in our computations.

Muon damped sources

If the synchrotron loss time scale of the muons is shorter than the decay time scale, the muons loose energy before they decay. In this case, only neutrinos from pion decays are present, leading to $\nu_e : \nu_\mu : \nu_\tau$ of $0 : 1 : 0$ (neutrinos and antineutrinos added), or $R_e = (Q_{\nu_e} + Q_{\bar{\nu}_e}) \,/\, \left(Q_{\nu_\mu} + Q_{\bar{\nu}_\mu}\right) \simeq 0$ (corresponds to $R \simeq 0.64$).

Neutron beam sources

Given the assumption of sources optically thin to neutrons, the neutrons leave the source and decay into protons, electrons, and electron antineutrinos. These neutrinos are typically found at low energies, unless the synchrotron losses of the pions and muons are so large (i.e., the magnetic fields are very large) that the neutrinos from neutron decays contribute significantly. In this case, we have $\nu_e : \nu_\mu : \nu_\tau$ of $1 :$

$0:0$ (neutrinos and antineutrinos added), or $R_e = (Q_{\nu_e} + Q_{\bar{\nu}_e}) \,/\, \left(Q_{\nu_\mu} + Q_{\bar{\nu}_\mu}\right) \to \infty$ (corresponds to $R \simeq 0.28$). Note that there are other potential sources of neutrons, such as neutrons produced by the photo-dissociation of heavy nuclei.

Muon beams

If the synchrotron loss time scale of the muons is shorter than the decay time scale, the muons loose energy before they decay. These muons may pile up at lower energies, where, similar to a neutrino factory, only neutrinos from muon decays are present. This leads to $\nu_e : \nu_\mu : \nu_\tau$ of $1:1:0$ (neutrinos and antineutrinos added), or $R_e = (Q_{\nu_e} + Q_{\bar{\nu}_e}) \,/\, \left(Q_{\nu_\mu} + Q_{\bar{\nu}_\mu}\right) \simeq 1$ (corresponds to $R \simeq 0.44$). Typically, a muon beam comes together with a muon damped sources at higher energies: The muons missing at high energies are recovered at lower energies. Note that there may be other sources of muon beams, such as heavy flavor decay (D, DS, B, etc.) dominated sources, where the pions and kaons interact before they can decay, whereas the heavy mesons have shorter lifetimes.

D. Redshift distributions on logarithmic scales

Some additional figures to explain some plots in references.

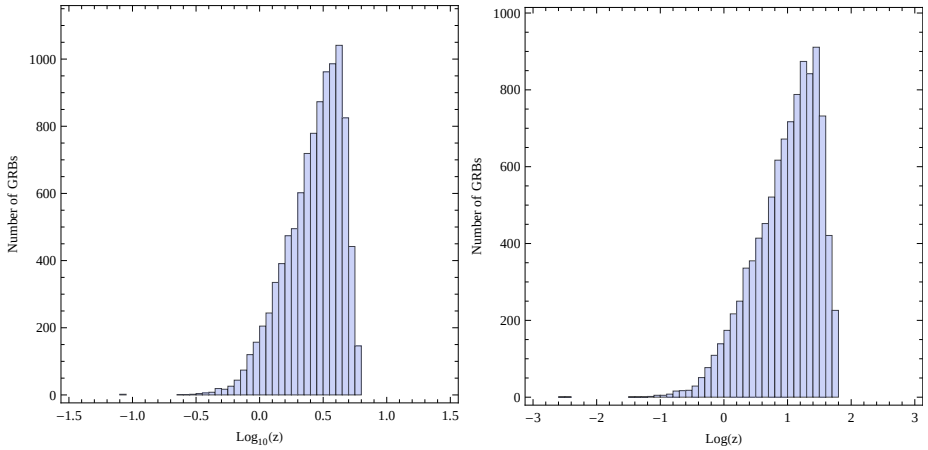

Figure D.1: Distribution of bursts in redshift on a logarithmic scale. The data is the data set tracing the star formation history by Hopkins and Beacom (Eq. (4.4)). The left plot is for a logarithm with a base of 10, the right plot for the natural logarithm.

E. Used seed for 66 burst data sets

# of set	Seed
1	0
2	5
3	12
4	249253
5	3641

Table E.1: These are the seeds used for the generation of the ten 66 burst data sets. Five sets were generated for the Lorentz factor Γ and five sets for the redshift z.

Acknowledgments

In this last paragraph I want to thank the people who helped during the progress of this thesis. First of all, I would like to thank PD Dr. Walter Winter for giving me the opportunity to work on this project and giving me an introduction in the vast field of neutrino physics. All the discussions and conversations helped to shape this work. Furthermore, Svenja Hümmer for all the help, information and feedback. Without her work none of the simulations would have been possible. Also, my officemate Jian Tang for help in countless questions, as well as Dr. Davide Meloni and Martin Krauß for their thoughts and expertise on various aspects of neutrino physics. Moreover, I have to thank Michael Rüger, Dr. Felix Spanier and Prof. Dr. Karl Mannheim for their input on the astrophysics topics in this work. All of your feedback and remarks were, and still are, greatly appreciated. And, last but not least, all the PhD and diploma students at the Lehrstuhl für Theoretische Physik II at the Universität Würzburg for making this thesis such a great time.
On a more personal note I would like to thank my parents for giving me all the love and support a son could wish for. And Silvana Olivares Flórez for being there at all times. Te amo, mi amor.

Erklärung

Gemäß der Studien- und Prüfungsordung für den Diplomstudiengang Physik an der Julius-Maximilians-Universität Würzburg erkläre ich hiermit, dass ich diese Arbeit selbstständig verfasst, keine anderen als die angegebenen Quellen und Hilfsmittel benutzt habe und die Arbeit bisher keiner anderen Prüfungsbehörde unter Erlangung eines akademischen Grades vorgelegt habe.

Würzburg, den 22. Dezember 2010

Philipp Baerwald